Title
Topological Properties of Magnetic Nanostructures in Amorphous Fe/Gd Multilayers

Author
Montoya, Sergio Antonio

Publication Date
2016

UNIVERSITY OF CALIFORNIA, SAN DIEGO

Topological Properties of Magnetic Nanostructures in Amorphous Fe/Gd Multilayers

A dissertation submitted in partial satisfaction of the

requirements for the degree

Doctor of Philosophy

in

Electrical Engineering

(Nanoscale Devices and Systems)

by

Sergio A. Montoya

Committee in charge:

Professor Eric E. Fullerton, Chair
Professor Olivia Graeve
Professor Vitaliy Lomakin
Professor Daniel Sievenpiper
Professor Sunil K. Sinha

2016

The dissertation of Sergio A. Montoya is approved, and it is acceptable in quality and form for publication on microfilm and electronically:

Chair

University of California, San Diego

2016

EPIGRAPH

“Work hard and measure something interesting”

Eric E. Fullerton

“Just keep swimming”

Doris, Finding Nemo

TABLE OF CONTENTS

TABLE OF FIGURES

ACKNOWLEDGEMENTS

First, I would like to thank my advisor Eric E. Fullerton for his mentorship during my doctoral studies. I have learned a great deal from you and admire your humility. Thank you for always making the time to discuss magnetism and everything in between, even when under pressure to submit another proposal a few hours before the deadline. Also, thank you for allowing me to explore a whole range of topics in magnetism and continually supporting my studies. I appreciate your feedback, advise and spell checks.

To all the members of the Fullerton Nanomagnetism group: Richard Choi, Nasim Eibagi, Matthias Gottwald, Tyler Hennan, Jimmy Kan, Dokyun Kim, Roopali Kukreja, Sohini Manna, Rajasekhar Medapalli, Sheena Patel, Haowen Ren, Conrad Rizal, Jonathan Sapan, Erik Shipton, Robert Tolley and Vojtěch Uhlĩr. I appreciate your patience and flexibility for allowing me to be part of the group. Apart from sharing experimental tools, I believe we shared meaningful experiences both at the personal and professional level. I especially would like to thank Erik Shipton and Matthias Gottwald for helping me get started in the group depositing and characterizing magnetic thin films. To those who joined me to synchrotron beam-time experiments, thank you for pressing forward even when the graveyard shift loomed ahead.

To the staff and researchers, present and past, of the Center for Memory Recording Research: Iris Villanueva, Fred Spada, Ami Berkowitz, Raymond Descoteaux, Marina Robenko, Jonathan Chae, Agapi Tshamjyan, Julie Matsuda and Kevin Wong. I thank you for your continuous support helping me navigate through the administrative side of my studies. I would have been lost placing orders in Marketplace. To Iris, thank you for being caring and warm as well as a great support these past years. To Fred Spada, thank you for the countless thought provoking discussions and allowing me to use some of your tools. I appreciate your guidance and insightful mentorship. To Ami, I enjoyed the plentiful discussions on magnetism and science. It was pleasure meeting. To Ray, thanks for always taking the time to machine countless devices and allowing me to use your tools. We had fun!

To the machines with whom I spent more time than I wish to divulge. We had rough patches, but we were able to compromise and learn to work with each other. I admit superstitions and rituals became part of our daily routines. Thank you for working tirelessly and yielding reproducible results.

To all the members of the Lomakin Micromagnetic group: Simon Couture, Majd Kuteifan, Sidi Fu, Marco Menarini, Iana Volvach, Marko Lubarda and Marco Escobar. Thank you for making me part of your group. I enjoyed the countless chats and discussions. To Simon and Majd, thanks for taking the time to help me carry out countless simulations.

I want to also thank all my collaborators. At the Lawrence Berkeley National Lab: Sujoy Roy, James Lee, Peter Fischer, Mi-Young Im and Steven Kevan. Thank you for introducing to incredible world of synchrotron soft x-ray techniques to study condensed matter physics. I have really enjoyed the opportunities to pursue different experiments at the coherent soft x-ray scattering beamline and the full-field transmission x-ray microscopy beamline and appreciate the insightful feedback on research projects. At the University of Oregon: Jordan Chess and Benjamin McMorran. Thank you for being a bright set of eyes investigating topology of magnetism and showing me the Lorentz transmission electron microscopy. To all, I've enjoyed our collaborations and look forward to continue doing science together!

I also acknowledge support from the U.S. Department of Defense (DOD,) Science, Mathematics & Research Transformation (SMART) Scholarship, the U.S. Department of Energy (DOE), Office of Basic Energy Sciences (Award No. DE-SC0003678), and the Space and Naval Warfare Systems Command (SPAWAR) Pacific. To the SMART scholarship, I am thankful for the financial support provided during my doctoral studies. To the Office of Basic Energy Sciences, I am thankful for funding multiple studies carried out at the Lawrence Berkeley National Lab, the Oakridge National Lab and the Stanford Linear Accelerator Center. To members of the Advanced Concepts and Applied Research Branch at SPAWAR Pacific: Benjamin Taylor, Susan Berggren, Marcio De Andrade, Osama Nayfeh, Teresa Emery and Anna Leese de Escobar. Thank you for the mentorship and learning opportunity provided during the Summer internships

Finally, I want to thank all my family. To my dad, mom and brothers. Thank you for your support in my doctoral studies. I know it hasn't been easy, but I appreciate your constant understanding and showing interest in my work. Most importantly, I am thankful for my wife's constant and unconditional support and encouragement. We have survived our version of Dante's journey while we both pursued our graduate studies. You are my anchor and the reason for which I continually strive to grow. I look forward to continue enjoying journeys together. Also, I want thank Sunshine, my dog, for always keeping me awake with your farts and snores. I appreciate your contributions to science, even if limited to your circadian rhythms.

Chapter 4 is a reprint of a manuscript submitted for publication: S. A. Montoya, S. Couture, J. J. Chess, J. C. T. Lee, N. Kent, D. Henze, S. K. Sinha, M.-Y. Im, S. D. Kevan, P. Fischer, B. J. McMorran, V. Lomakin, S. Roy and E. E. Fullerton. *Tailoring magnetic*

energies to stabilize dipole skyrmions and skyrmion lattices. arXiv:1608.01368 (2016). The dissertation author was the primary author of the manuscript.

Chapter 5 is a reprint of a manuscript being prepared for submission to a journal: S. A. Montoya, S. Couture, J. J. Chess, J. C. T. Lee, N. Kent, M.-Y. Im, S. D. Kevan, P. Fischer, B. J. McMorran, S. Roy, V. Lomakin, and E. E. Fullerton. *Resonant properties of dipole stabilized skyrmions in amorphous Fe/Gd multilayers*. (Preprint) The dissertation author was the primary author of the manuscript.

Chapter 6 is based on a manuscript being prepared for submission to a journal: S. A. Montoya, M. V. Lubarda, S. Couture, V. Lomakin and E. E. Fullerton. *Anisotropic magnetoresistance properties of dipole skyrmions in amorphous Fe\Gd multilayers*. (Preprint) The dissertation author was the primary author of the manuscript.

VITA

2016	Ph.D. in Electrical Engineering (Nanoscale Devices and Systems), UC San Diego
2014	M.S. in Electrical and Computer Engineering, UC San Diego
2010	B.A. in Physics and B.A. in Mathematics, UC Berkeley

PUBLICATIONS

S. A. Montoya, M. V. Lubarda, S. Couture, V. Lomakin and E. E. Fullerton. *Anisotropic magnetoresistance properties of dipole skyrmions in amorphous Fe\Gd multilayers*. Preprint. (2016).

H.-H. Lin, M.-H. Yang, R. Sharma, M. Puckett, S. A. Montoya, C. Wurm, F. Vallini, E. E. Fullerton and Y. Fainman. *Synthesis of Second-order Nonlinearities in Dielectric-Semiconductor-Dielectric Metamaterials.* APL Submitted. (2016).

S. A. Montoya, S. Couture, J. J. Chess, J. C. T. Lee, N. Kent, M.-Y. Im, S. D. Kevan, P. Fischer, B. J. McMorran, S. Roy, V. Lomakin, and E. E. Fullerton. *Resonant properties of dipole stabilized skyrmions in amorphous Fe/Gd multilayers*. Preprint (2016).

J. Smalley, F. Vallini, S. A. Montoya, L. Ferrari, S. Shahin, C. Riley, B. Kante, E. E. Fullerton, Z. Liu and Y. Fainman, *Luminescent Hyperbolic Metasurfaces*, Nature Comm. [accepted] (2016).

S. A. Montoya, S. Couture, J. J. Chess, J. C. T. Lee, N. Kent, D. Henze, S. K. Sinha, M.-Y. Im, S. D. Kevan, P. Fischer, B. J. McMorran, V. Lomakin, S. Roy and E. E. Fullerton. *Tailoring magnetic energies to stabilize dipole skyrmions and skyrmion lattices*. PRB Submitted. arXiv:1608.01368 (2016).

J. J. Chess, S. A. Montoya, T. R. Harvey, C. Ophus, S. Couture, V. Lomakin, E. E. Fullerton, B. J. McMorran. *A streamlined approach to mapping magnetic induction of skyrmion materials*. Submitted to Ultramicroscopy. arXiv:1608.06000 (2016).

R. Medapalli, D. Afanasiev, D. Kim, Y. Quessab, S. A. Montoya, A. Kirilyuk, T. Rasing, A. V. Kimel and E. E. Fullerton. *Mechanism of all-optical control of ferromagnetic multilayers with circularly polarized light*. PRL Submitted. arXiv:1607.02505 (2016).

J. C. T Lee, J. J. Chess, S. A. Montoya, X. Shi, N. Tamura, S. K. Mishra, P. Fischer, B. J. McMorran, S. K. Sinha, E. E. Fullerton, S. D. Kevan and S. Roy. *Synthesizing skyrmion bound pairs in Fe-Gd films*. Appl. Phys. Lett. **109**, 022402 (2016).

CONFERENCE PAPERS

J. J. Chess, S. A. Montoya, E. E. Fullerton and B. J. McMorran. *Determination of domain wall chirality using in situ Lorentz transmission electron microscopy*. AIP Advances (Submitted) (2016).

J. S. Smalley, F. Vallini, S. A. Montoya, L. Ferrari, C. Riley, S. Shahin, B. Kante, E. E. Fullerton, Z. Liu and Y. Fainman. *Light-Emitting Hyperbolic Metasurfaces at Telecom Frequencies.* Advanced Photonics 2016 (IPR, NOMA, Sensors, Networks, SPPCom, SOF), OSA Technical Digest (online) (Optical Society of America, 2016).

J. J. Chess, S. A. Montoya, J. C. T. Lee, S. Roy, S. Kevan, E. E. Fullerton and B. J. McMorran, *Observation of Skyrmions at Room-temperature in Amorphous Fe/Gd Films*, Microsc. Microanal **21** (Suppl 3), (2015).

CONFERENCE PRESENTATIONS

S. A. Montoya, M. V. Lubarda, J. J. Chess, S. Couture, B. J. McMorran, V. Lomakin and E. E. Fullerton. *Anisotropic Magnetoresistance Properties of Skyrmions in Amorphous Fe\Gd Multilayers*. 61th Conference on Magnetism and Magnetic Materials, New Orleans, LA, USA, October 31 – November 4, 2016.

S. A. Montoya, S. Couture, J. J. Chess, J. C. T. Lee, N. Kent, M.-Y. Im, S. D. Kevan, P. Fischer, B. J. McMorran, S. Roy, V. Lomakin, and E. E. Fullerton. *Resonant Properties of a Skyrmionic RE-TM Ferrimagnet with Weak Perpendicular Magnetic Anisotropy*. 13th Joint MMM-Intermag Conference, San Diego, CA, USA, January 11 – January 15, 2015.

S. A. Montoya, S. Couture, J. J. Chess, J. C. T. Lee, N. Kent, M.-Y. Im, S. D. Kevan, P. Fischer, B. J. McMorran, S. Roy, V. Lomakin, and E. E. Fullerton. *Resonant Properties of a Skyrmionic RE-TM Ferrimagnet with Weak Perpendicular Magnetic Anisotropy*. Lawrence Berkeley National Lab, Advanced Light Source User Meeting – Correlations Methods in X-ray Scattering (invited), Berkeley, CA, USA, October 5 – October 7, 2015.

S.A. Montoya, A. Vashenko, E. E. Fullerton. *Ferromagnetic alloys with tailored properties for rf applications*. 59th Conference on Magnetism and Magnetic Materials (poster), Honolulu, HI, USA, November 3 – November 7, 2014.

ABASTRACT OF THE DISSERTATION

Topological Properties of Magnetic Nanostructures in Amorphous Fe/Gd Multilayers

by

Sergio A. Montoya

Doctor of Philosophy in Electrical Engineering (Nanoscale Devices and Systems)

University of California, San Diego, 2016

Professor Eric E Fullerton, Chair

The dissertation explores in detail the formation of dipole stabilized skyrmions and skyrmion lattices that we discovered in amorphous Fe/Gd multilayers. The dipole skyrmion phase exists in amorphous Fe/Gd films which is commonly associated as a classical magnetic bubble material. However, as we discuss throughout the thesis, there are clear distinctions between both magnetic textures in topology, magnetic energies required to favor their formation and their response under external perturbations. Bubble domains typically form in films where the uniaxial anisotropy K_U exceeds the demagnetization anisotropy $K_D = 2\pi M_S^2$ or have a $Q = K_U/2\pi M_S^2 > 1$ whereas the dipole skyrmions and skyrmion lattices we report exist in thin films with $Q < 1$.

Over the course of the thesis, we present comprehensive studies as individual chapters describing the magnetic, ferromagnetic resonance and transport properties associated with the dipole skyrmions. For each of these studies, we first identified the dipole skyrmion phase using real and reciprocal space imaging techniques and then quantified the respective properties of these films. We then established a one-to-one correlation between magnetic, ferromagnetic resonance and transport measurements and the domain morphologies observed thus allowing us to assign unique attributes to the dipole skyrmion phase. With aid of numerical simulations, we are able to further validate our experimental observations and investigate additional magnetic information that is not easily accessible in experiments.

Overall, dipole skyrmions possess interesting physics that are comparable and complements the physics observed in skyrmions stabilized by the Dzyaloshinskii–Moriya interaction. The sub-100nm features exists over a broad range of temperatures and magnetic fields which can further tuned by modifying the film composition or thickness. The dipole skyrmion phase exists in a material parameter space that had previously not been investigated by neither bubble domain nor skyrmion scientific communities. Last, our results show that a lot of the interesting physics resulting from these textures appears to be a result of topology and not the physical mechanism that forms these chiral cylindrical-like textures.

Chapter 1

Introduction

1.1 Motivation

The rise of the internet of things and mobile technologies has prompted the development of a new wave of research to produce non-volatile memory devices that offers very high memory density, very fast data read and write abilities, exceedingly low power consumption and is inexpensive. A promising technology, proposed in 2008, suggested encoding information in magnetic domain walls along small magnetic wires. To access the encoded information that lies in the magnetic wires, low-density electrical currents are used to move the magnetic domain walls along the length of the magnetic wires. Given the nature of how information is accessed, the memory was termed 'racetrack memory' [1]. This new technology was proposed as a solid-state potentially 3-D storage platform aimed to replace most data storage devices, including RAM, FLASH and even hard drives, reduce the manufacturing cost per gigabyte and be very energy efficient [2,3] .

A great deal of efforts have been invested to understand the mechanisms for fast displacement of domain walls using electrical currents and in exploring these effects in different materials [4-6]. This resulted in the observation of a skew exchange interaction, commonly known as Dzyaloshinskii–Moriya interaction (DMI), and as strong spin-orbit coupling effects in thin films structures consisting of a heavy metal, ferromagnet and oxide layers. One of the challenges observed when displacing domain walls with currents resulted when these encountered defects in magnetic wires which pinned the domain wall [1,7,8]. In order to unpin the domain wall, relatively high current densities were required which deteriorated the energy efficiency and controllability of the racetrack memory.

At the same time racetrack memory was being investigated, particle-like magnetic domains textures termed 'skyrmions' were for the first time observed experimentally using small-angle neutron scattering in MnSi at ~30K [9]. It was shown that these skyrmion textures arranged in a close packed hexagonal lattice and formed in a narrow temperature window under the application a perpendicular magnetic field. Since these magnetic textures possess a domain wall that continuously wraps around the cylindrical-like domain, they are termed topologically protected because the domain wall protects the skyrmion feature from continuous deformation by external forces to the uniform state [10-12]. It was then shown that these skyrmion features could be displaced with ultra-low current densities and unlike domain walls these chiral textures did not pin easily to defects [12-14].

The prospects of developing a universal memory based on skyrmions, prompted strong research efforts to investigate properties of these magnetic textures to facilitate their exploitation in technologies as well as the exploration of new materials that stabilizes these textures. Today, these textures exist in an array of materials from bulk magnets [9,15-17] to thin films [18-25] and have been shown to be stable under several physical mechanisms [25-29]. Most materials exhibit a skyrmion phase at cryogen temperatures, but there are a few materials that form these textures at and above room temperature. Since the initial observation of skyrmion, research efforts have solely been focused on investigating DMI skyrmions because it was anticipated, early on, that these textures would exhibit sub-100nm features, whereas dipole skyrmions were expected to possess magnetic features are a few orders of magnitude larger.

1.2 Scope of the Thesis

This thesis is focused specifically on the study of dipole skyrmions and skyrmion lattices that we discovered in amorphous Fe/Gd multilayers. The work presented demonstrates that dipole skyrmions with sub-100nm features are spontaneously formed in thin films. We show that dipole skyrmions and magnetic bubbles are distinct magnetic features that form under the same physical mechanism: competition of dipole energy and domain wall energy. Throughout this thesis, we detail comprehensive studies detailing the magnetic, ferromagnetic resonance and transport properties of dipole skyrmions and skyrmion lattices. Many of our observations are generalized to be inherent properties of these chiral domains are valid in other ferromagnets and ferrimagnets. Overall, it is the first in-depth study of a class of skyrmions that has not received considerable attention since their initial discovery. The results, herein, demonstrate this class of skyrmions possess far richer textures and novel properties than expected.

In Chapter 2, the basic magnetic concepts on the formation of magnetic domains in thin films with perpendicular magnetic anisotropy are described, including information about magnetic stripe domains and bubble domains. Emphasis is given to the subject of skyrmions to provide sufficient background to grasp the significance of the results provided in this thesis. Some properties of skyrmions are described more closely in the individual Chapters were it is more relevant.

In Chapter 3, we briefly review many of the experimental techniques utilized to carry out the growth, characterization and optimization of amorphous Fe/Gd multilayers. In addition, we describe many real- and reciprocal-space imaging techniques used to profile the magnetic domains that form in Fe/Gd multilayers under varying magnetic fields and temperatures. Since some material property characterization requires the continuous films be patterned to nanowires, we also detail the fabrication processed utilized.

In Chapter 4, the magnetic properties that result in the formation of dipole skyrmions and skyrmion lattices in amorphous Fe/Gd multilayers are explored through thickness, temperature and alloy composition studies. Real- and reciprocal-space imaging techniques are used to image the field and temperature dependence of magnetic domains in Fe/Gd multilayers. Then material properties that result in a skyrmion phase are quantified and compared to numerical simulations. Excellent correlation in domain morphology is found between the experimentally observed magnetic textures and their numerical counterparts. Micromagnetic results allow us to predict that these class of skyrmions possess a far richer textures than originally foreseen. Finally, we explore the sensitivity to magnetic properties that result in formation of a closed packing lattice of dipole skyrmions. The results presented in this chapter provide guidelines to engineer materials which exhibit dipole skyrmions in ferromagnets and ferrimagnets.

In Chapter 5, the resonant properties of dipole skyrmions in amorphous Fe/Gd multilayers are explored using ferromagnetic resonance. Temperature, thickness and field history dependent studies are performed on numerous Fe/Gd specimens which are detailed in resonant mode and magnetic field dispersions. Using magnetic phase maps, we further correlate the resonant modes to specific magnetic domain textures. We then use numerical simulations to interpret the resonant modes which allow us to predict the existence of new localized spin-wave modes in dipole skyrmions. We also show that dipole skyrmions and bubble domains exhibit different dynamics under microwave fields. Altogether, we predict dipole skyrmions exhibit complex dynamics under microwave fields that are dependent on the resonant frequency and the helicity of magnetic texture.

In Chapter 6, the anisotropic magnetoresistance properties of dipole skyrmions and skyrmion lattices are explored by means of magnetic field and temperature dependent studies on amorphous Fe/Gd multilayers patterned into wires with different width and fixed length. The Fe/Gd film studied possess disordered stripe domains above 180K and a dipole skyrmion phase below 180K. The anisotropic magnetoresistance is collected along three field-current probing directions as a function of temperature. We find the field varying polar resistivity response shows an artifact at temperatures where a skyrmion phase has been experimentally observed. Numerical simulations were performed to compute the field dependent domain states and then compute the anisotropic magnetoresistance. Very accurate correlations are observed between experiments and simulations, which suggest the observed artifact in the polar resistivity results from a Bloch-line rearrangement.

In Chapter 7, I summarize the experimental and numerical findings for the studies detailed in this thesis and provide a future outlook of potential studies on dipole skyrmions.

1.3 References

[1] S. P. Parkin, M. Hayashi and L. Thomas, *Magnetic domain-wall racetrack memory*, Science **320**, 190-194 (2008).

[2] S. P. Parkin and S.-H. Yang, *Memory on the racetrack,* Nature Nano. **10**, 195-198 (2015).

[3] D. A. Allwood, G. Xiong, C. C. Faulkner D. Atkinson, D. Petit and R. P. Cowburn, *Magnetic domain-wall logic*, Science **309**, 5741 (2005).

[4] I. M. Miron, T. Moore, H. Szambolics, L. L. Buda-Prejbeanu, S. Auffret, B. Rodmacq, S. Pizzini, J. Vogel, M. Bonfim, A, Schuhl and G. Gaudin, *Fast current-induced domain-wall motion controlled by the Rashba effect*, Nature Mat. **10**, 419-423 (2011).

[5] K.-S. Ryu, L. Thomas, S.-H. Yang and S. P. Parkin, *Chiral spin torque at magnetic domain walls*, Nature Nano. **8**, 527-533 (2013).

[6] K.-S. Ryu, S.-H. Yang, L. Thomas and S. P. Parkin, *Chiral spin torque arising from proximity-induced magnetization*, Nature Comm. **5**, 3910 (2014).

[7] T. Koyama, D. Chiba, K. Ueda, K. Kondou, H. Tanigawa, S. Fukami, T. Suzuki, N. Ohshima, N. Ishiwata, Y. Nakatani, K. Kobayashi and T. Ono, *Observation of the intrinsic pinning of a magnetic domain wall in a ferromagnetic nanowire*, Nature Mat. **10**, 194-197 (2011).

[8] H. Y. Yuan and X. R. Wang, *Domain wall pinning in notched nanowires*, Phys. Rev. B. **89**, 054423 (2014).

[9] Mühlbauer, B. Binz, F. Jonietz, C. Pfleiderer, A. Rosch, A. Neubauer, R. Georgii and P. Böni. *Skyrmion lattice in a chiral magnet*. Science **323**, 915-919 (2009).

[10] F. Hellman, A. Hoffmann, Y. Tserkovnyak, G. Beach, E. E. Fullerton, C. Leighton, A. MacDonald, D. Ralph, D. Arena, H. Durr, P. Fischer, J. Grollier, J. Heremans, T. Jungwirth, A. Kimmel, B. Koopmans, I. Krivorotov, S. May, A. Petford-Long, J. Rondinelli, N. Samarth, I. Schuller, A. Slavin, M. Stiles, O. Tchernyshyov, A.

Thiaville, B. Zink, *Interface induced phenomena in magnetism,* arXiv:1607.00439v2 (2016).

[11] H.-B. Braun, *Topological effects in nanomagnetism: from superparamagnetism to chiral quantum solitons.* Adv. Phys. **61:1**, 1-116 (2012).

[12] N. Nagaosa and Y. Tokura, *Topological properties and dynamics of magnetic skyrmions*. Nature Nano. **8**, 899-911 (2013).

[13] A. Fert, V. Cros and J. Sampaio, *Skyrmions on the track*. Nature Nanotech. **8**, 152–156 (2013).

[14] J. Sampaio, V. Cros, S. Rohart, A. Thiaville and A. Fert, Nucleatio, stability and current-induced motion of isolated magnetic skyrmions in nanostructures, Nature Nano. 8, 839-844 (2013).

[15] W. Münzer, A. Neubauer, T. Adams, S. Mühlbauer, C. Fran, F. Jonietz, R. Georgii, P. Böni, B. Pedersen, M. Schmidt, A. Rosch and C. Pfleiderer. *Skyrmion lattice in the doped semiconductor FeCoSi*, Phys. Rev. *B*. **81**, 041203(R) (2010).

[16] X. Z. Yu, Y. Onose, N. Kamazawa, J. H. Park, J. H. Han, Y. Matsui, N. Nagaosa and Y. Tokura. *Real-space observation of a two-dimensional skyrmion crystal*. Nature **465**, 901–904 (2010).

[17] S. Seki, X. Z. Yu, S. Ishiwata and Y. Tokura, *Observation of skyrmions in a multiferroic material.* Science **336**, 198-201 (2012).

[18] X. Z. Yu, N. Kanazawa, Y. Onose, K. Kimoto, W. Z. Zhang, S. Ishiwata, Y. Matsui and Y. Tokura. *Near room-temperature formation of a skyrmion crystal in thin-films of the helimagnet FeGe.* Nat. Mater. **10**, 106-109 (2011).

[19] W. Jiang, P. Upadhyaya, W. Zhang, G. Yu, M. B. Jungfleisch, F. Y. Fradin, J. E. Pearson, Y. Tserkovnyak, K. L. Wang, O. Heinonen, S. G. E. te Velthuis, A. Hoffmann. *Blowing Magnetic Skyrmion Bubbles.* Science **349**, 283 (2015).

[20] C. Moreau-Luchaire, C. Moutafis, N. Reyren, J. Sampaio, C. A. F. Vaz, N. Van Horne, K. Bouzehouane, K. Garcia, C. Deranlot, P. Warnicke, P. Wohlhüter, J.-M. George, M. Weigand, J. Raabe, V. Cros and A. Fert. *Additive interfacial chiral interaction in multilayers for stabilization of small individual skyrmions at room temperature,* Nat. Nanotech. **11**, 444-448 (2016).

[21] S. Woo, K. Litzius, B. Krüger, M.-Y. Im, L. Caretta, K. Richter, M. Mann, A. Krone, R. M. Reeve, M. Weigand, P. Agrawal, I. Lemesh, M.-A. Mawass, P. Fischer, M. Kläui and G. S. D. Beach. *Observation of room-temperature magnetic skyrmions and*

their current-driven dynamics in ultrathin metallic ferromagnets. Nat. Mat. **15**, 501-506 (2016).

[22] W. Wang, Y. Zhang, G. Xu, L. Peng, B. Ding, Y. Wang, Z. Hou, X. Zhang, X. Li, E. Liu, S. Wang, J. Cai, F. Wang, J. Li, F. Hu, G. Wu, B. Shen and X.-X. Zhang. *A centrosymmetric hexagonal magnet with superstable biskyrmion magnetic nanodomains in a wide temperature range of 100K-340K*. Adv. Mater. 1521-4095 (2016).

[23] J. C. T Lee, J. J. Chess, S. A. Montoya, X. Shi, N. Tamura, S. K. Mishra, P. Fischer, B. J. McMorran, S. K. Sinha, E. E. Fullerton, S. D. Kevan and S. Roy. *Synthesizing skyrmion bound pairs in Fe-Gd films*. Appl. Phys. Lett. **109**, 022402 (2016).

[24] X. Z. Yu, K. Shibata, W. Koshibae, Y. Tokunaga, Y. Kaneko, T. Nagai, K. Kimoto, Y. Taguchi, N. Nagaosa and Y. Tokura. *Thermally activated helicity reversal of skyrmions*. Phys. Rev. *B* **93**, 134417 (2016).

[25] X. Z. Yu, M. Mostovoy, Y. Tokunaga, W. Zhang, K. Kimoto, Y. Matsui, Y. Kaneko, N. Nagaosa and Y. Tokura. *Magnetic stripes and skyrmions with helicity reversals*. Proc. Natl Acad. Sci. USA **109**, 8856–8860 (2012).

[26] I. Dzyaloshinskii*, A thermodynamic theory of "weak" ferromagnetism of antiferromagnetics*. J. Phys. Chem. Solids **4**, 241–255 (1958).

[27] T. Moriya, *Anisotropic superexchange interaction and weak ferromagnetism*. Phys. Rev. Lett. **120**, 91–98 (1960).

[28] S. Heinze, K. von Bergmann, M. Menzel, J. Brede, A. Kubetzka, R. Wiesendanger, G. Bihlmayer and S. Blüger. *Spontaneous atomic-scale magnetic skyrmion lattice in two dimensions.* Nature Phys. **7**, 713-718 (2011).

[29] T. Okubo, S. Chung and H. Kawamura, *Multiple-q states and the skyrmion lattice of the triangular-lattice heisenberg antiferromagnet under magnetic fields*. Phys. Rev. Lett. **108**, 017206 (2012).

Chapter 2

Magnetic Domains

2.1 Introduction

In thin films with perpendicular magnetic anisotropy (PMA) the balance between ferromagnetic exchange, anisotropy, and dipolar energies often results in stripe and bubble domain patterns. Understanding the formation and properties of these periodic domain structures has been an active research topic dating back to the 1950's [1-4]. The characteristic width of the periodic or quasi-periodic domains depends on the materials properties such as magnetization, exchange and anisotropy and varies with film thickness. Furthermore, the domain morphology and period depends sensitively on the application of magnetic fields, the field history and the presence of disorder. Domains can arrange in a variety of metastable configurations and hysteresis effects are connected with domain generation, annihilation and transformation. Because of this variability, magnetic films with PMA have been an ongoing test-bed for the physics of stripe and bubble phases [4-8].

The presence and control of magnetic bubbles has also gained interest for their potential application to novel memory technologies. This was thoroughly investigated in the 1970's [1-4, 9-15], and has attracted renewed interest because of their potential to bring about highly scalable and low power consumption non-volatile memory for mobile technologies [16-18]. Today, a magnetic bubble with non-trivial topology is termed a skyrmion [19-21]. Apart from their technological applications, these textures exhibit interesting new physics when these textures interact with conduction electrons and result in novel dynamics when perturbed with external forces.

Over the course of this chapter, I introduce concepts of magnetic domains, magnetic domain walls and the formation of magnetic stripe domains and magnetic bubble domain in thin films with perpendicular magnetic anisotropy. I will then focus on describing magnetic skyrmion domains, including the physical mechanisms that result in their formation and distinctive properties. Additional information about skyrmions is detailed in the individual chapters discussing the various studies presented in this thesis.

2.2 Magnetic Domains

Magnetic domains are microscopic configurations of interacting magnetic moments. In ferromagnetic materials, the arrangement of magnetic domains can vary from single domain states in ultra-thin films where all the magnetic moments are aligned in the same direction to complex multi-domain configurations that form as the thickness of the magnetic film is increased. The formation and arrangement of magnetic domains results from the interactions of magnetic moments over short and long distances. Each of these interactions result in a total magnetic energy,

$$E_T = E_{exchange} + E_{anisotropy} + E_{magnetostatic} + E_{Zeeman} \tag{2.1}$$

that accounts nearest neighbor interactions between magnetic moments ($E_{exchange}$), a preferable orientation of the magnetic moments due to the crystal lattice arrangement ($E_{anisotropy}$), the effect of internal fields ($E_{magnetostatic}$) resulting from magnetic moments across the whole magnetic specimen, and the rearrangement of magnetic moments under an applied magnetic field (E_{Zeeman}). Additional energetic contributions can arise due to magnetostriction and magneto elastic effects which distort the latter magnetic interactions and can be incorporated as an anisotropy contribution.

A magnetic specimen, thin film or bulk, exists in a state of equilibrium (either stable or metastable) which results from minimizing the total magnetic energy E_T which is achieved by the creating of magnetic domains of varying shape and size. As a result, the identification of magnetic domains presents a direct link to the physics of ferromagnetism.

2.2.1 Magnetic Energies of Ferromagnets

To further understand the formation of magnetic domains, let us consider describing in more detail the magnetic energies of a homogenous single-crystal ferromagnet with cubic symmetry. First, the origin of a magnetic moment arises both from the spin of the electrons (spin moment) and the electrons orbiting around an atom (orbital moment). Given the charge and angular momentum of these particles, the moving electrons act as current which induce an intrinsic magnetic dipole moment. It is through this magnetic field from both the spin and orbits that are generated by a ferromagnet.

Exchange energy.

In ferromagnets, the exchange interaction is responsible for maintaining the spontaneous macroscopic magnetic order under zero applied field. Its origin is electrostatic but in order to explain it we require quantum mechanics. We know that electrons can be described in terms of wavefunctions and that interacting waves of identical particles result in a quantum mechanical interaction, known as the exchange interaction, which basically describes the relative proximity of the electrons. The exchange interaction can be very strong and keeps neighboring spins aligned parallel or antiparallel to each other.

The exchange energy is described in terms of the Heisenberg Hamiltonian,

$$H_{ex} = -\frac{1}{2}\sum_{\substack{i,j \\ i \neq j}} J_{ij}\, \boldsymbol{S_i} \cdot \boldsymbol{S_j} \tag{2.2}$$

where $\boldsymbol{S_i}$ and $\boldsymbol{S_j}$ are the magnetic spins of neighboring magnetic moments and J_{ij} is the exchange coupling integral. From equation 2.3, we see the exchange interaction depends on the orientation of the magnetic spins. When the nearest neighbor magnetic spins are oriented parallel (ferromagnet) the exchange coupling is positive $J_{ij} > 0$, whereas antiparallel magnetic spins (antiferromagnet) result in a negative exchange $J_{ij} < 0$.

To account variations of magnetic moments in films with multi-domains, one can describe the exchange energy in terms of a continuum approximation [22-23] which Taylor expands Eq. 2.2 into

$$E_{exchange} = -\frac{nJS^2}{a}\left(|\widehat{m_x}|^2 + \left|\widehat{m_y}\right|^2 + |\widehat{m_z}|^2\right) = A_{ex}(\nabla\,\widehat{\boldsymbol{m}})^2, \quad \widehat{\boldsymbol{m}} = \boldsymbol{M}(\boldsymbol{r})/M_S \quad (2.3)$$

$$\boldsymbol{M}(\boldsymbol{r}) = \sum_i \boldsymbol{m}_i(\boldsymbol{r}) \quad (2.4)$$

where A_{ex} is the exchange stiffness constant, J is the exchange coupling from Eq. 2.2, n is the number of atoms per unit cell, a is the lattice constant, $\widehat{\boldsymbol{m}}$ is the unit magnetic vector, M_S is the saturation magnetization and $\boldsymbol{M}(\boldsymbol{r})$ is the magnetization vector.

Anisotropy energy.

In magnetic materials, the magnetization typically lies along a preferential direction or directions called the easy axis. This favorable orientation can be perpendicular or along the plane of the magnetic film. In either case, the arrangement of the magnetic moments results from the coupling between the spin moment to the orbital moment which is dictated by the crystal lattice. Since each atom is discretely positioned in a lattice configuration the ions produce a potential that causes the cloud of electrons to orbit along a particular direction. Given the origin of this interaction it is called the magneto-crystalline anisotropy. This magneto-crystalline anisotropy tends to orients of the magnetization along specific easy axis and generally a small magnetic field is required to align all the magnetic moments along this preferable direction. Conversely, ferromagnets possess a less favorable orientation orthogonal to the easy axis termed the hard axis, which requires higher magnetic fields to orient the magnetization along this direction. The mathematical description for magneto-crystalline anisotropy energy reflects the symmetry of the crystal structure. Often in thin films and for the samples described in this thesis the energy associated with the magnetic-crystalline anisotropy is uniaxial (as only has one preferred axis in the material) and can be written as:

$$E_{anisotropy} = \sum_{n}^{\infty} K_{u,n} \sin^{2n}(\theta) = K_{u,1} \sin^2 \theta + K_{u,2} \sin^4 \theta + \cdots \approx K_{u,1} \sin^2 \theta \quad (2.5)$$

where K_u are anisotropy constant and θ is the angle between the easy axis and the magnetization [13, 24, 25]. From Eq. 2.5, we see the anisotropy energy is minimal when the magnetic moment lies in the same direction as the easy axis. In the case of a ferromagnet with cubic crystal structure the anisotropy can be expressed as:

$$E_{anisotropy} = K_{u,1}(\alpha_1^2\alpha_2^2 + \alpha_2^2\alpha_3^2 + \alpha_3^2\alpha_1^2) + K_{u,2}(\alpha_1^2\alpha_2^2\alpha_3^2) + \cdots \quad (2.6)$$

where $\alpha_i = \cos(\theta_i)$ and θ_i is the angle between the magnetization and the easy axes [13, 25].

Magnetostatic energy.

Given each magnetic dipole moment $\boldsymbol{m_i}$ induces its own magnetic field which allows it to interacts locally and globally, it follows that the whole magnetic body generates its own magnetic field which influences the arrangement of the magnetization $\boldsymbol{M}(\boldsymbol{r})$. For a magnetic specimen with volume V, the magnetostatic energy is given by:

$$E_{magnetostatic} = -\frac{1}{2} \int_V \boldsymbol{M}(\boldsymbol{r}) \cdot \boldsymbol{H_d}(\boldsymbol{r})\, dV \quad (2.7)$$

where $\boldsymbol{H_d}(\boldsymbol{r})$ is the demagnetization field which can be described in terms of scalar potential $\Phi_d(\boldsymbol{r})$ such that:

$$\mathbf{H_d} = -\nabla \cdot \Phi_d(\boldsymbol{r}) \quad (2.8)$$

$$\Phi_d(\boldsymbol{r}) = -\int_V \frac{\nabla \cdot \boldsymbol{M}(\boldsymbol{r}')}{|\boldsymbol{r} - \boldsymbol{r}'|} dV' + \int_S \frac{\widehat{\boldsymbol{n}} \cdot \boldsymbol{M}(\boldsymbol{r}')}{|\boldsymbol{r} - \boldsymbol{r}'|} dS' \tag{2.9}$$

where r' is the variable to be integrated over the volume V and surface S, and $\hat{n}$ is the outward unit vector normal to the surface S [13,]. From Eqs. 2.7, 2.8 and 2.9, it is clear that the magnetostatic energy can be fairly complex to calculate for magnetic specimens with complex geometries or non-uniform magnetization. However, in the case of simple geometries where the magnetization is uniform throughout the magnetic body one can more easily determine the demagnetization field rather easily because $\nabla \cdot \boldsymbol{M} = 0$ which makes the magnetostatic energy term solely dependent on the shape of the specimen.

In the case of a magnet with an ellipsoid shape, the demagnetization field $\boldsymbol{H_d}$ has the same direction as the magnetization and is uniform in the sample [13, 25],

$$\boldsymbol{H_d} = -4\pi D\, \boldsymbol{M} \tag{2.10}$$

where D is a tensor that is called the demagnetization tensor. The tensor D describes how the magnetization lies along the axes and must satisfy the identity,

$$\sum_i D_{ii} = 1 \tag{2.11}$$

As a result, the demagnetization field for simple geometries can be described. In the case of a sphere, the demagnetization lies along all three axes, thus $D_x = D_y = D_z = 1/3$. For an infinitely long cylinder along the z-axis $D_z = 0$ and $D_x = D_y = 1/2$. Whereas an infinite slab that lies along the *xy*-plane only exhibits a demagnetization for the magnetization that lies perpendicular to the plane, such that $D_x = D_y = 0$ and $D_z = 1$. We can thus express the demagnetization field $\boldsymbol{H_d}$ for an infinite slab as,

$$\boldsymbol{H_d} = -4\pi M_z \tag{2.12}$$

It follows, that the magnetostatic energy for a thin film can be written as,

$$E_{magnetostatic} = 2\pi M_z^2 \tag{2.13}$$

Zeeman Energy.

The interaction of magnetic moments $\boldsymbol{m}$ under an applied magnetic field $\boldsymbol{H}$ is referred as the called a Zeeman interaction and is described by [13],

$$E_{Zeeman} = -\boldsymbol{m}\,(\boldsymbol{r}) \cdot \boldsymbol{H}(\boldsymbol{r}) \tag{2.14}$$

Alternatively, one can describe the Zeeman energy in terms of the magnetization vector $\boldsymbol{M}(\boldsymbol{r})$ which then takes the form,

$$E_{Zeeman} = -\int_V \boldsymbol{M}(\boldsymbol{r}) \cdot \boldsymbol{H}(\boldsymbol{r})\, d^3\boldsymbol{r} \tag{2.15}$$

that accounts for the Zeeman energy over the whole magnetic specimen.

2.2.2 Thickness Evolution of Magnetic Domains

For a magnetic film with no crystalline anisotropy the magnetization will lie in-plane (M_z=0) so the magnetostatic (Eq. 2.13) will be zero. However, if there strong perpendicular magnetic anisotropy such that the magnetization lies along the z-direction the internal field will be $-4\pi M_s$ and magnetostatic energy for the sample with be $2\pi M_s^2V$ where V is the volume of the sample. When the thickness of a magnetic film is increased, the volume increases and there is a build-up of magnetostatic energy (Fig 2.1a). To reduce the magnetostatic energy, the uniform magnetization can be broken into domains of opposite magnetization (Fig. 2.1b, c). As more domains are introduced into the magnetic specimen, the magnetostatic energy is continuously reduced and can be nearly eliminated

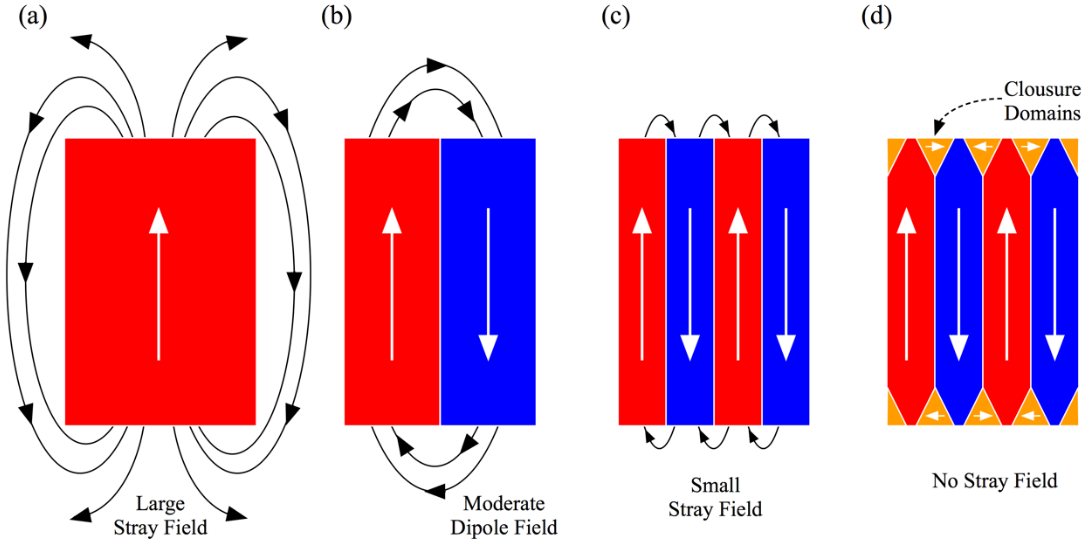

Figure 2.1 – Stray field from perpendicular magnetic domain. (a) A single magnetized domain will exhibit the highest stray field. (b, c) Introducing a multi-domain configuration reduces the stray field outside the domain. (d) Néel caps, also called closure domains, can eliminate the formation of magnetic flux outside the domains.

by introducing of closure domains at the top and bottom of the film (Fig. 2d) known as Néel caps. However, the introduction of a magnetic domain results in an energetic penalty because magnetic moments aligned antiparallel result in an increase of the exchange energy. As a result, a final domain state is reached when the subdivision of domains does not incur in a greater exchange energy than decreasing the magnetostatic energy.

Figure 2.2 details the domain morphology of [Co (0.4nm)/Pt(0.6nm)]xN multilayer films with different number of bilayers N = 5, 10, 20, 40, 80 and 160 at zero-field. The domain states are imaged using magnetic force microscopy where variations of intensity reveal perpendicular domains with magnetization that is oriented “up” (yellow) and “down” (brown). For N=5 repetitions, the film exhibits very large domains with irregular shape across the field of view (Fig. 2.2a). As the bilayer repetitions are increased, N=10,

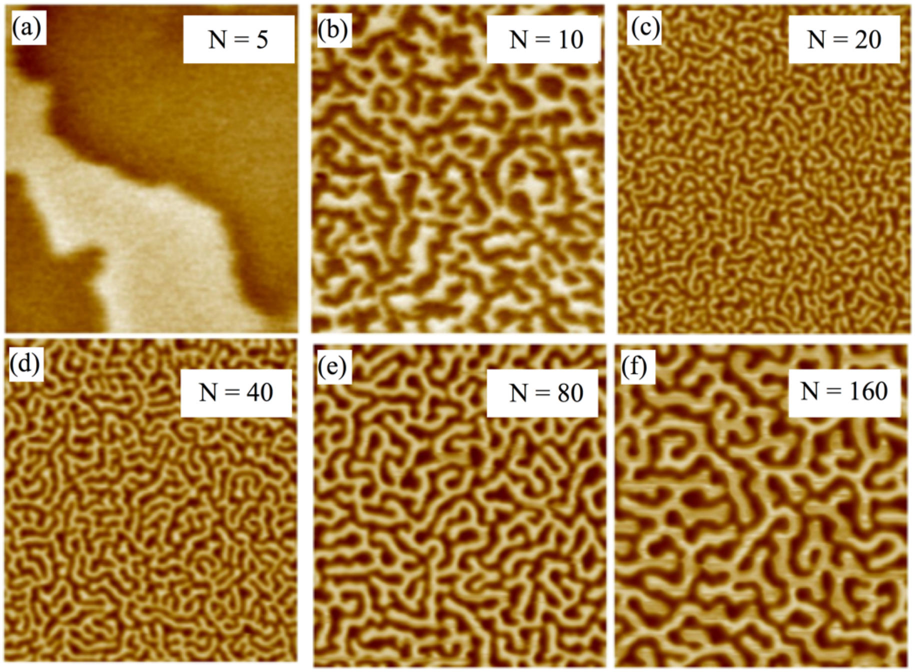

Figure 2.2 – Thickness dependence of domain states. (a-f) Shows the domain morphology of [Co (0.4nm)/ Pt (0.7nm)]xN for different N bilayer repetitions: **(a)** 5, **(b)** 10, **(c)** 20, **(d)** 40, **(e)** 80 and **(f)** 160 under zero-field at room temperature. Figure reproduced with permission from: **a-f**, ref. ##.

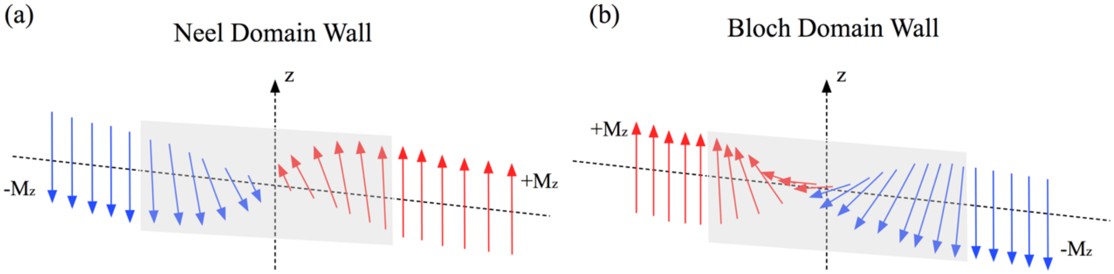

Figure 2.3 – Bloch and Néel walls. Schematics detail the smoothly varying magnetization of a **(a)** Néel and **(b)** Bloch domain wall separating two opposite magnetization perpendicular domains.

the opposite magnetization domains become more comparable in size and shape (Fig. 2.2b). Further increasing the bilayers, N=20, we observe the domains continue decreasing in size and exhibit worm-like domain features (Fig. 2.2c). Above a critical thickness, the domains begin to increase in size and always exhibit opposite domains of equal width at remanence (Fig. 2.2d-f)

2.2.3 Magnetic Domain Walls

Magnetic domains that are magnetized in opposite direction are separated by a finite boundary which describes how the magnetization smoothly changes orientation from one magnetization state to the other. This boundary is known as a magnetic domain wall. In films with perpendicular magnetic anisotropy (PMA), 180° domain walls are some of the simplest domain walls that can form. Here, there are two paths the magnetization can take to reorient its direction by 180° from one domain state to another: if the magnetization rotates in the plane of the magnetic domain, the wall is called a Néel domain wall (Fig. 2.3a); similarly, if the magnetization rotates out of the plane of the magnetic domain, the wall is called Bloch domain wall (Fig. 2.3b).

Typically, Bloch walls are almost always favored in thin films with PMA. The domain wall width is mainly given by competing magnetic anisotropy energy and exchange energy. In the case of a one dimensional Bloch wall, the domain wall energy can be written as,

$$\sigma_w = \int_{-\infty}^{\infty} A\left(\frac{\partial\theta}{\partial x}\right)^2 + K sin^2(\theta) dx = 4\pi\sqrt{AK} \tag{2.16}$$

where the first term corresponds to the exchange energy and the second is the anisotropy energy.

2.3 Stripe Domains

Stripe domains are particularly interesting because they represent the lowest energetic magnetic domain state achievable in a film with perpendicular magnetic anisotropy. Typically thin films exhibit this domain morphology if they possess a uniaxial magnetic anisotropy K_U that exceeds the magnetostatic energy $2\pi M_S^2$ and require the film to exhibit a minimum critical film thickness [3,4,13].

Figure 2.4 details the magnetic hysteresis and domain morphology of an [Fe(0.36nm) /Gd(0.4nm)]x80 film that exhibits labyrinth domains (i.e. stripe domains where the domain wall do not have a preferred in-plane direction) measured at room temperature. The magnetic domains states are captured using full-field transmission x-ray microscopy along the Fe L_3 edge (708 eV) where variations of intensity depict magnetic domains pointing “up” (white) and “down” (dark). When a perpendicular magnetic field is applied, the stripe with magnetization opposite to the field will shrink and the other will grow (Fig. 2.4c-d). This process continues to occur until the extremities of the stripe domain shrinking collapse into cylindrical magnetic domains, termed magnetic bubbles (Fig. 2.4f-g). At this point, magnetic bubbles are randomly space throughout the specimen and the bubbles tend not to interact given the repelling dipole field interactions (Fig. 2.4h). When the magnetic field is increased further, the bubble domain’s diameter decreases until

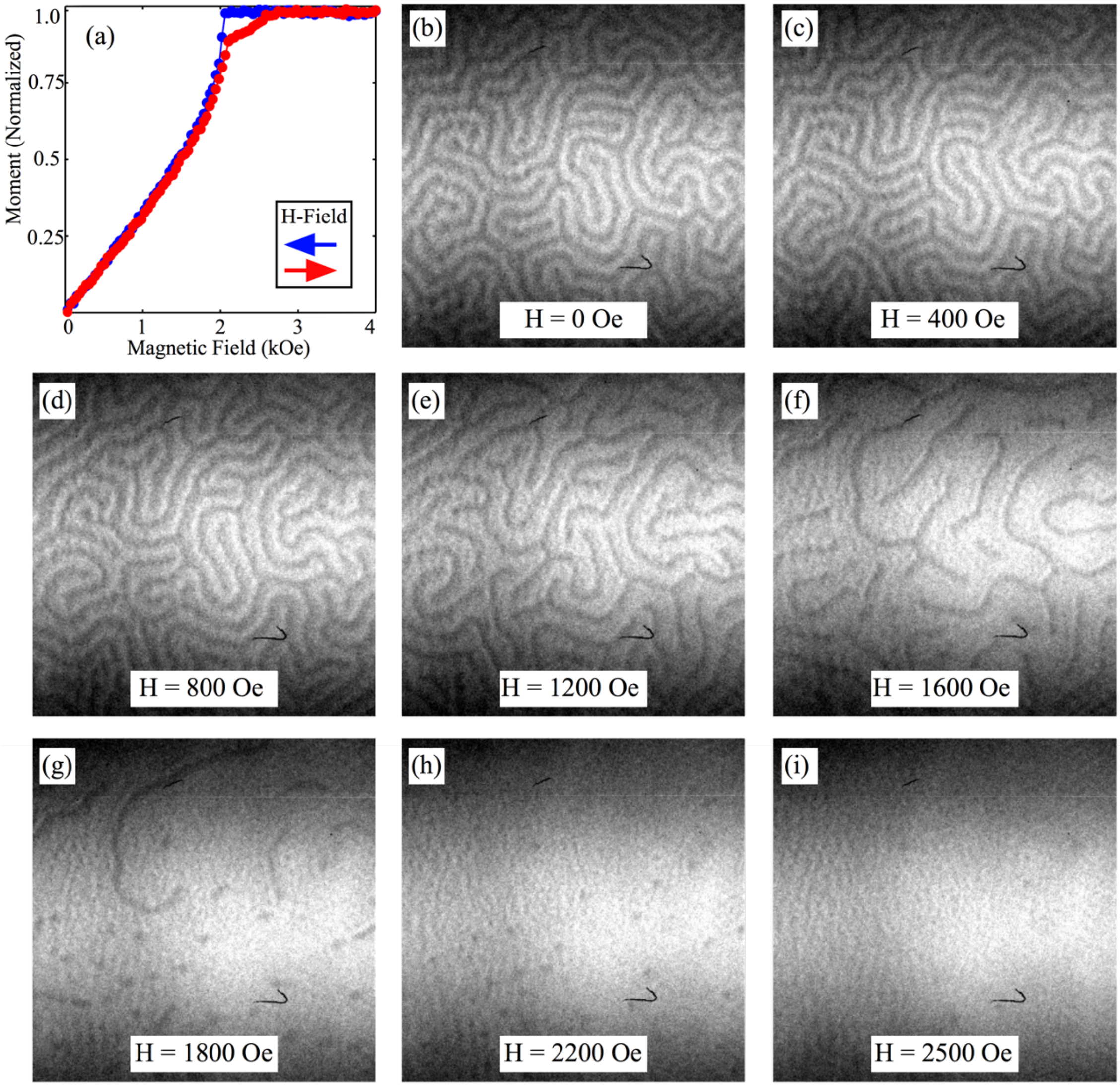

Figure 2.4 – Field dependence of perpendicular stripe domains. (a) A representative magnetic hysteresis of a film exhibiting disordered stripe domains. The field direction is colored differently for the magnetic field reduced from positive to negative magnetic saturation, and vice-versa. **(b-i)** Shows the domain morphology as a magnetic field is applied from zero-field to positive saturation where different magnetic phases are observable: **(b-e)** stripe domains, **(f-g)** stripe domains collapsing to cylindrical domains, **(h)** disordered cylindrical domains and **(i)** uniform magnetization.

they collapse at a critical field, known as the collapse field, which occurs close to magnetic saturation (Fig.2.4).

In the case the magnetic field is reduced from magnetic saturation, magnetic bubbles will form at pinning (defect) sites and will continue to grow in diameter as the field is reduced until reaching a nucleation field, another critical field, which is typically depicted by a sharp kink in the magnetization (Fig. 2.4a). At this field the bubbles are submitted to an elliptical instability [10] which results in the bubble domains branching out to elongated stripe-like domains. By further decreasing the field, the thin film is filled with maze-like domains by means domain wall motion [3,10,15]. At zero field, the domain morphology consists of alternating perpendicular magnetic domains with magnetization pointing along\opposite the direction of the magnetic field. Overall, most ferromagnet and ferrimagnet films that exhibit perpendicular stripe domains exhibit the latter field history dependence.

2.4 Magnetic Bubbles

A magnetic bubble is a cylindrical-like magnetic domain that generally forms in films with perpendicular magnetic anisotropy under the application of a magnetic field [9-15]. On a film, the cylindrical domain has magnetization down and the region outside the domain boundary has magnetization up. Most commonly magnetic bubbles form as a result of a collapsing stripe domain and these textures are uncorrelated [10,12], as described before. However, films with specific ratio of magnetic properties and film thickness can result in hexagonal lattice of close packed magnetic bubbles under a magnetic field [13,15].

These ordered magnetic bubbles where primarily observed and investigated in crystalline magnets, such as: garnets, hexaferrites and orthoferrites [11,12-14,]. Although, they were also observed in amorphous materials [13].

Favorable conditions to form bubble domains include a uniaxial magnetic anisotropy energy K_U that exceeds the demagnetization energy $2\pi M_S^2$ and a film thickness d which is not less than $d = \sqrt{A/K_U}\ (K_U/2\pi M_S^2\ )$ where A is the exchange length, or greater than 30 to 50 times the latter thickness [15]. By convention, the ratio of $K_U/2\pi M_S^2$ is defined as the material Q-factor. Fundamentally, bubble domains are anticipated to form in thin films with high perpendicular magnetic anisotropy and low magnetization, i.e. Q > 1. Given the magnetic energy and thickness requirements, a bubble domain is characterized by a Bloch domain wall with negligible width [15].

2.5 Skyrmions

Until now, magnetic domains have solely been described in terms of competing ferromagnetic exchange, anisotropy and magnetostatic energy. One can further categorize magnetic domains in terms of their topology. The topology can be characterized by a winding number S which is given by

$$S = \frac{1}{4\pi} \iint \hat{\boldsymbol{m}} \cdot \left(\frac{\partial\, \hat{\boldsymbol{m}}}{\partial x} \times \frac{\partial \hat{\boldsymbol{m}}}{\partial y} \right) dx\, dy \qquad (2.17)$$

where $\hat{\boldsymbol{m}}$ is the unit vector in the direction of the magnetization [19-21]. A skyrmion is defined as a cylindrical-like domain that has a domain wall with magnetization continuously wrapping around the texture which results in a winding number S = 1. The

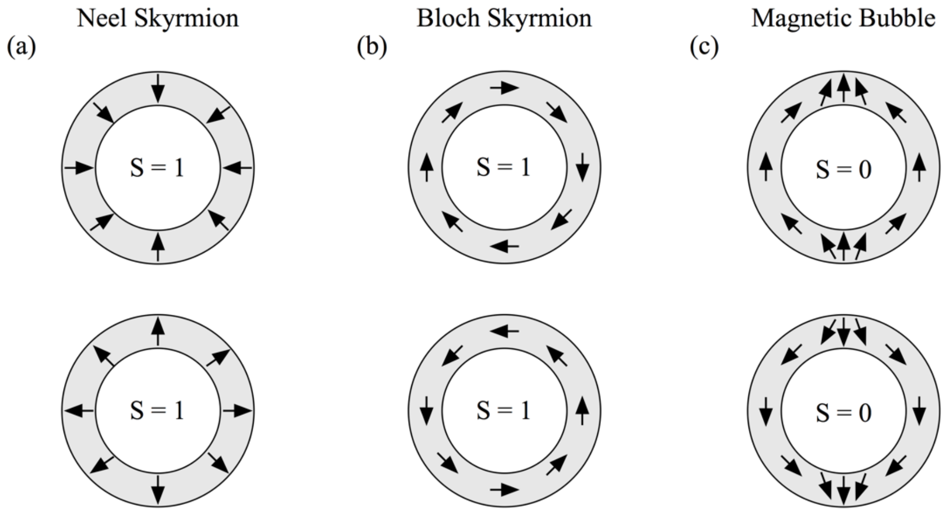

Figure 2.5 – Magnetic domains with different winding number. (a, b) Simple schematics show skyrmions with either **(a)** Néel or **(b)** Bloch type with two possible helicities. **(c)** Bubble domain has Bloch wall with two possible helicities.

vorticity or helicity of the wrapping can be clockwise or counterclockwise (Fig. 2.5a, b). Lastly, skyrmions domains can form with either Néel or Bloch domain walls (Fig. 2.5a, b).

Although magnetic bubbles and skyrmions are both cylindrical-like textures, there is a distinction in the terms of the winding number. A magnetic bubble is typically defined as a trivial texture since it has a winding number S = 0. Figure 2.5c shows that the domain wall of a trivial magnetic bubble has two discontinuities where the magnetization changes its vorticity at each discontinuity along the boundary of the cylindrical domain. These discontinuities are called Bloch-points.

2.5.1 Physical Mechanisms to Stabilize Skyrmions

The formation of skyrmion lattices and isolated skyrmion domains results from the interplay of different magnetic energies. Most materials known to host skyrmions are stabilized by competing ferromagnetic exchange and Dzyaloshinskii–Moriya interaction (DMI) or exchange [26-28]. The first describes the symmetric interaction of magnetic spins, as detailed earlier, whereas the DMI interaction describes the antisymmetric exchange of magnetic spins which are described by the DMI Hamiltonian,

$$H_{DM} = -\boldsymbol{D_{ij}} \cdot \left(\boldsymbol{S_i} \times \boldsymbol{S_j}\right) \qquad \boldsymbol{D_{ij}} = \lambda \boldsymbol{a} \times \widehat{\boldsymbol{r_{ij}}} \tag{2.18}$$

where $\boldsymbol{S_i}$ and $\boldsymbol{S_j}$ are neighboring spins, $\boldsymbol{D_{ij}}$ is an orientation vector perpendicular to the canted spins, $\widehat{\boldsymbol{r_{ij}}}$ is the unit distance vector connecting spins $\boldsymbol{S_i}$ and $\boldsymbol{S_j}$, $\mathbf{a}$ is distance mediating the super-exchange and λ is the spin-orbit constant [26]. This exchange favors the canting of magnetic spins and thus supports chiral arrangements of the magnetization.

In magnetic materials with non-centrosymmetric crystal structures (MnSi [29], FeCoSi [30-31], FeGe [32], MnFeGe [33], CuO_2SeO_3 [34]) the lack of inversion symmetry in the crystal structure results in a DMI that causes the magnetic spins to skew thus arranging in a helical structure. Under a magnetic field, the helical spins undergo a phase change from a helical phase to conical phase before the spins are completely aligned in the direction of the saturation field. Near the critical temperature T_C, a skyrmion phase become stable due to thermal fluctuations in between the helical and conical phases [20]. Typically, the skyrmion phase is restricted to a narrow window of temperatures close to T_C in these kind of magnets [20]. It has been shown that reducing the thickness from a bulk crystal to a thin platelet with thickness below the helical period can result in a skyrmion phase that

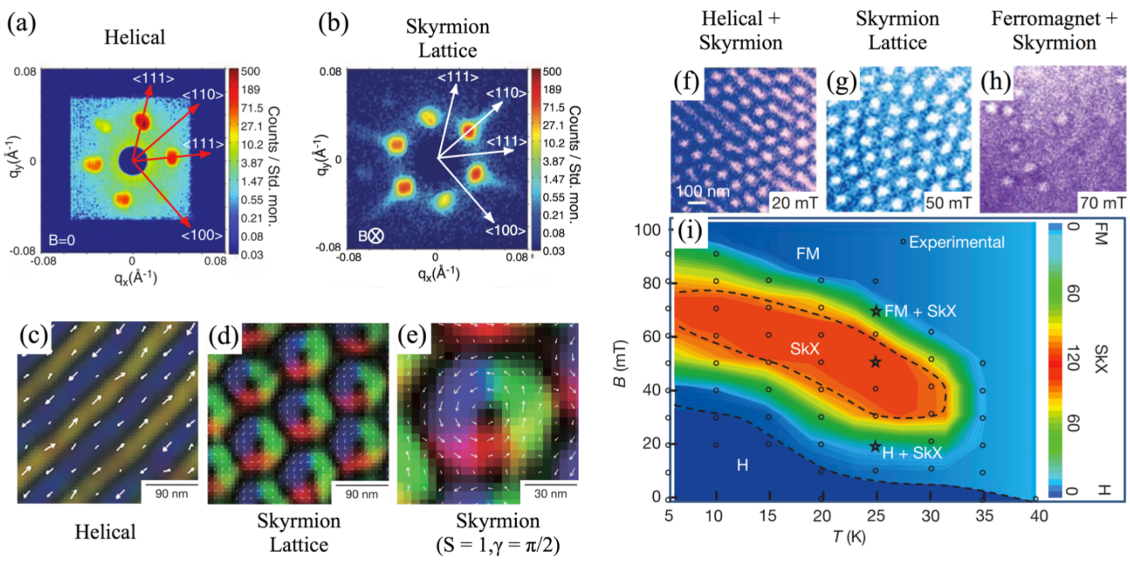

Figure 2.6 –Real and reciprocal space imaging of skyrmion lattice. (a, b) Small angle neutron scattering images detail the **(a)** helical phase at $H_z = 0$ Oe and **(b)** skyrmion lattice phase at $H_z = 1640$ Oe that forms in MnSi at 27K. **(c, d)** Magnetic induction color maps obtained from analyzing under-focused, focused and over-focused Lorentz TEM images with the transport of intensity equation show **(c)** helical stripes and **(d)** a hexagonal skyrmion lattice. The white arrows in **(c, d)** detail the in-plane magnetization. **(e)** The center skyrmion in **(d)** is enlarged to show chiral texture in greater detail. **(f-i)** Characteristic domain states of a centrosymmetric magnet showing DMI skyrmions are detailed and used to construct a magnetic phase map consisting of temperature and magnetic fields at which different magnetic states are favorable in MnSi. Figure reproduced with permission from: **a-b**, ref. 29 © AAAS; **c-i**, ref. 31 © NPG.

exists over a broader range of magnetic fields and temperatures [32,35]. This was first shown for FeGe platelets [32] and now has become a common practice to extend the skyrmion phase in non-centrosymmetric magnets.

Thin films with broken mirror symmetry at the interface can result in antisymmetric exchange interactions when the ferromagnetic layer is interfaced and is enhanced for large spin-orbit coupling heavy metal. Given the asymmetric exchange results from the interface it is called interfacial DMI interaction. Most of the reported skyrmions stabilized at room

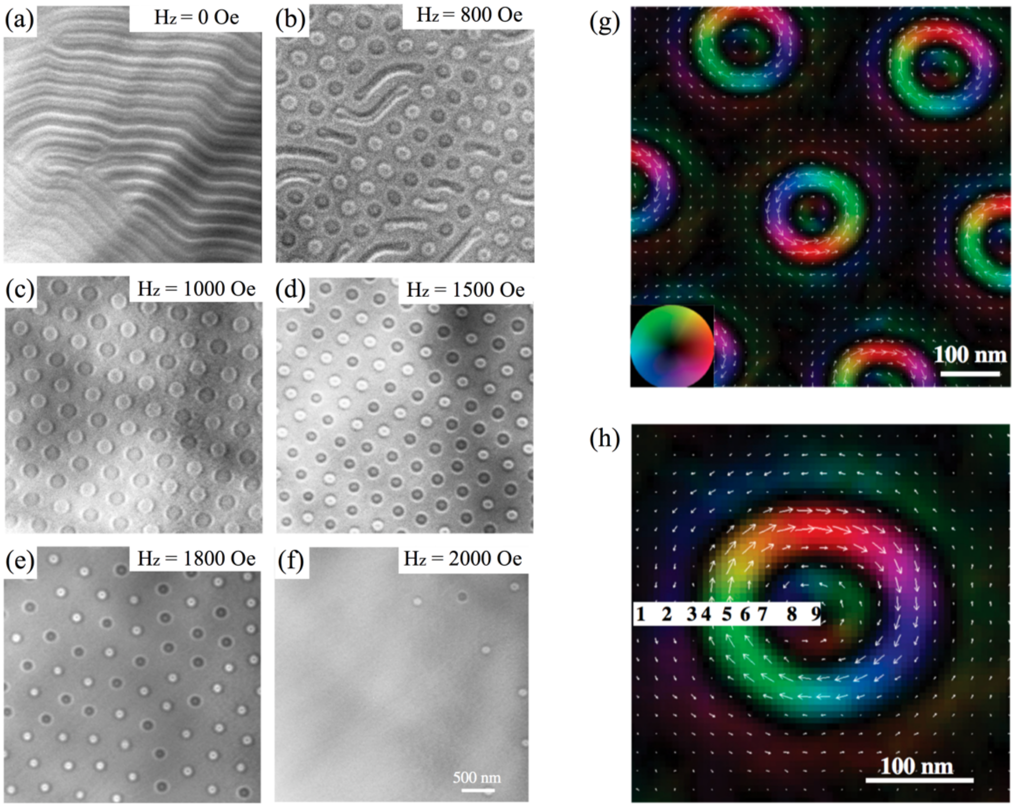

Figure 2.7 – Dipole stabilized skyrmions. The field dependent domain morphology of a thin BaFeScMgO, an Sc-doped barium ferrite, is shown as a perpendicular magnetic field is applied at room temperature. Different magnetic phases are observed as a magnetic field is applied from zero-field to magnetic saturation: **(a)** stripes, **(b)** mixture of stripes and dipole skyrmions, **(c, e)** dipole skyrmion lattice of two helicity chiral textures and **(f)** disordered dipole skyrmions. **(g, h)** Shows the magnetic induction map from the dipole skyrmion lattice with chiral textures of random helicities at H_z = 1500 Oe. **(h)** Shows a magnified image of a dipole skyrmion with clockwise helicity. Figure reproduced with permission from: **a-h**, ref. 39, © 2011 National Academy of Science.

temperature are a result of this class of DMI [36-38]. An interesting characteristic about DMI skyrmions, is that their helicity is set by the sign of the DMI. As a result, all the chiral textures have the same vorticity.

Skyrmions can also form under the competition of dipolar energy and domain wall energy [39-41], which is the mechanism by which magnetic stripes and bubbles form in thin films with perpendicular magnetic anisotropy. The latter type of skyrmions are commonly refereed as ‘dipole skyrmions’ to differentiate them to those stabilized by DMI. Dipole skyrmions had solely been identified experimentally in Sc-doped M-type barium ferrite [39, 40] and amorphous Fe/Gd multilayers [41]. Similar to DMI skyrmions, these chiral textures form under the application of a perpendicular field. However, a dipole skyrmion phase is characterized by a mixture of two possible helicities ($S = 1$, $\gamma = \pm\pi/2$) [20]. That is, there is a coexistence of equal populations of left and right helicity dipole skyrmions.

Lastly, the formation of a two-dimensional hexagonal lattice of skyrmions can result from frustrated exchange interactions [42] and four spin interactions [43] in a two-dimensional magnet. Experimentally, a two-dimensional Fe monolayer on Ir(111) exhibits a skyrmion ground state by means of competing ferromagnetic exchange, four spin exchange and DMI. Skyrmions stabilized by frustrated exchange have not been experimentally verified, but they are theoretically anticipated. Both these mechanisms result in skyrmion textures on the crystal lattice length scales (~1nm).

2.5.2 Skyrmion Properties

Usually, magnetic materials that host a skyrmion phase are accompanied by a magnetic phase map which details the temperatures and magnetic fields where the chiral textures are stable as well as other magnetic phases (Fig. 2.6i). Typically, they are constructed using reciprocal-space scattering (Fig. 2.6a, b) and/or real (Fig. 2.6c-e) space imaging techniques. Since most skyrmions in crystal magnets arrange in a close packed hexagonal lattice, this can easily be identified in reciprocal space by a six-fold scattering pattern (Fig. 2.6b). The first skyrmion materials where identified using scattering techniques, like small angle neutron scattering [29,30] and it was later demonstrated that the same scatter pattern is also observable by means of coherent soft x-ray scattering [44]. One must note that reciprocal space images do not contain any information about the chirality nor vorticity of the skyrmions. These solely provide information the existence of cylindrical-like textures arranged in a hexagonal lattice.

Real space images of skyrmions are typically captured using electron microscopy [31-33-35, 40-41] or scanning probe microcopy techniques [43]. One of the most common and powerful real-space imaging techniques is Lorentz transmission electron microscopy (LTEM) because one can access information about the chirality of the magnetic domains with high spatial resolution (~1nm) which facilitates the imaging of nanomagnetic domains. This technique and others are further explored in Chapter 3 where the experimental techniques are detailed. Real-space images allow us to directly capture the field evolution from magnetic stripe domains to skyrmion domains (Fig. 2.6c-g), and also capture the formation of isolated skyrmions (Fig. 2.6i), a state that is not detectable in reciprocal space.

The primary reason a magnetic phase map accompanies most materials is because the skyrmion phase is normally stabilized at cryogen temperatures and for technological applications it is desirable to know the temperature and magnetic fields at which these textures form. Often, the first order magnetic transitions – helical, conical, skyrmion and

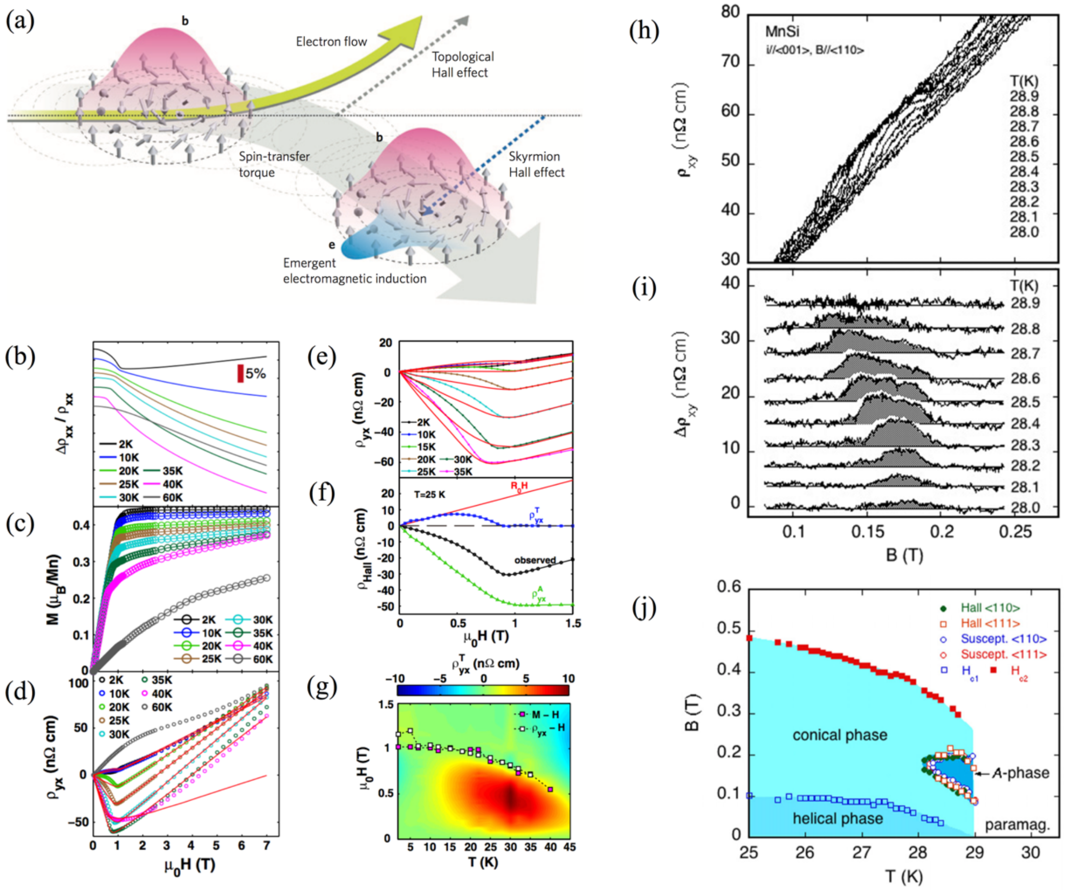

Figure 2.8 – Topological hall response. (a) Schematic shows the interaction of a flowing electron with a skyrmion texture. Electron current displaces the skyrmion by means of spin transfer torque and the electron path is modified. **(b-e)** Show the longitudinal resistivity, magnetization and transverse resistivity as a function of perpendicular magnetic field for a 50-nm thick MnSi patterned film at different temperatures ranging from 60K to 2K. **(f)** Shows the topological hall resistivity calculated from results in **(b-e)** at 25K. **(g)** A topological hall resistivity phase map is constructed from results like those in **(f)**. Regions of the phase map with high topological hall resistivity are correlated with the skyrmion hexagonal lattice. **(h-j)** Details the topological hall response resulting from a bulk MnSi patterned film. The transverse resistivity **(h)** shows clear evidence of an additional Hall contribution at temperatures where the skyrmion phase is observed. The latter is further resolved in **(i)**. The topological Hall resistivity is overlaid on a magnetic phase map **(j)** constructed from small angle neutron scattering data. Figure reproduced with permission from: **a**, ref. 20, © 2013 NPS; **b-g** ref. 49, © 2013 PRL; **h-j,** ref. 47, © 2009 PRL.

ferromagnet state – are usually identified in a magnetic phase map for DMI skyrmion materials, or similarly the domain morphology – stripes, stripe-to-skyrmion, skyrmion lattice, isolated skyrmions and uniform magnetization – are identified as a function of applied magnetic field.

There is a notion in the literature that the size of skyrmion textures, based on initial observations of these chiral domains, which suggests that each physical mechanism yields skyrmions of a given dimension [20,39,45-46]. Skyrmions induced by DMI are predicted to form textures with diameters ranging from 5nm to 100nm; whereas, dipole interactions are anticipated to yield the largest skyrmion textures, 100nm to 1μm or larger. However, this is not an accurate assertion for either class of skyrmions given several recent observations [35-38]. In the case of DMI skyrmions, textures with features larger than a few micrometers have been recently reported as well as sub-100nm dipole skyrmions, the subject of this thesis.

When conduction electrons interact with a non-trivial magnetic texture, the spin of the electrons couple to the magnetization wrapping around the skyrmion accumulating a quantum mechanical phase known as a Berry phase (Fig. 2.8a) [20]. This gives rise to an effective field which leads to a topological Hall contribution [47-53] and the physical displacement of the skyrmion by means of spin transfer torque [54-55]. This topological Hall contribution is beyond the ordinary and anomalous Hall effects (Fig. 2.8d-e, h-i). It has been experimentally reported for several DMI skyrmion materials such as: MnSi [47-50], MnGe [51] and FeGe [52]. Often it is used to construct magnetic phase maps to detail the magnetic fields and temperatures where the skyrmion phase forms (Fig. 2.8g, j) [49-

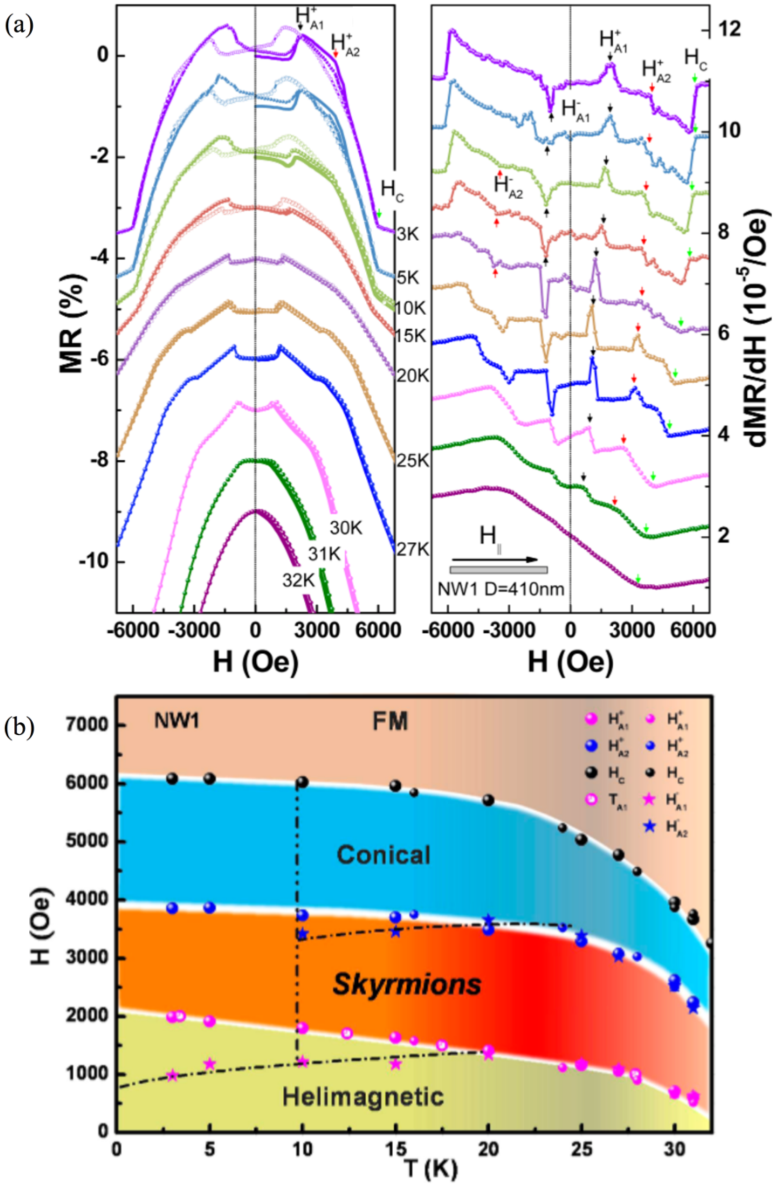

Figure 2.9 – Magnetoresistance from non-centrosymmetric magnet hosting DMI skyrmions. (a) The field dependence of the magnetoresistance (MR) and its derivative is detailed for a MnSi nanowire of 410-nm width as a function of temperature. The magnetoresistance (MR) is defined as MR = [R(H) – R(0)]/R(0) and the magnetic field is applied along the length of the wire. At temperatures above 30K, the MR can be described in terms of a parabolic response. Below 30K, the MR response begins to show artifacts as distinct fields. The critical magnetic fields are labeled: H_{A1}^{+}, H_{A2}^{+} and H_c. The derivative of the MR as a function field clearly shows the existence of critical fields. **(b)** Magnetic phase map constructed from results in **(a)** show the skyrmion phase is extended to lower temperatures. Figure reproduced with permission from: **a-b**, ref. 55, © 2014 Nano. Lett.

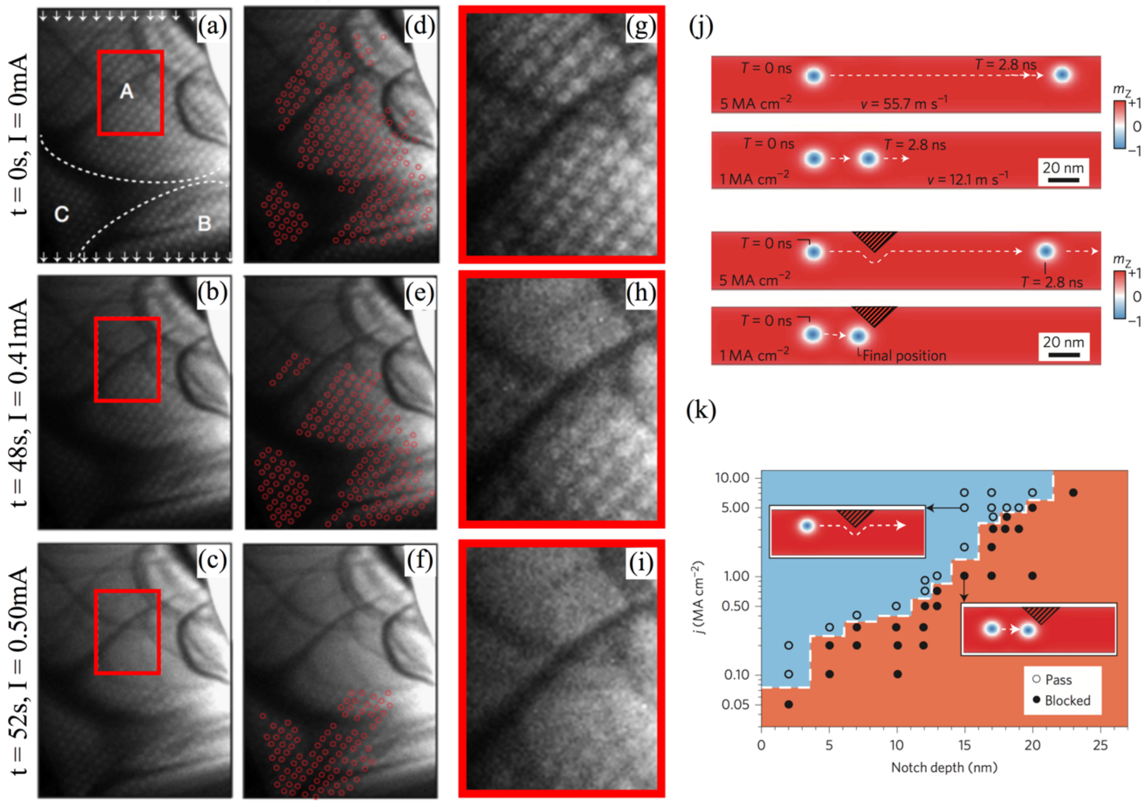

Figure 2.10 – Current induced motion of DMI skyrmions. (a-i) Shows the dc current induced displacement of a skyrmion lattice that is identified with Lorentz TEM in a 100-nm platelet of FeGe under H_z = 1500 Oe at 250K. **(a-c)** Show the skyrmion lattice as the applied current is increased from **(a)** I=0mA to **(b)** I = 0.41mA and **(c)** I = 0.5mA. Then panels **(d-e)** overlay masks, in red color, over the skyrmion features shown in **(a-c)** as a guide to the eye. Also, regions enclosed in the red box of **(a-c)** are enlarged in panels **(g-i)**. **(j, k)** Details the displacement of skyrmions on a track under different current densities and also illustrates that higher current densities are required to push a skyrmion feature pass an artifact lying on the track. **(k)** Illustrates the required currents densities to move skyrmions passed a notch of varied depth. Figure reproduced with permission from: **a-i**, ref. 57, © 2012 NPS, **j** ref. 18, © 2013 NPS, and **k**, ref. 59, © 2013 NPS.

53]. Bear in mind, the observation of a topological Hall effect is not a direct measure that a skyrmion phase exists in a material [54].

In non-centrosymmetric magnets, it has also been observed that the anisotropic magnetoresistance, i.e. the change in electrical resistance due to the orientation of the magnetization with respect to the electrical current direction in the material, exhibits artifacts at comparable magnetic fields where the specimen undergoes magnetic phase changes from helical, skyrmion, conical and ferromagnetic states [55-56] (Fig. 2.9a). This was first observed in patterned MnSi nanowires [56] and has now been adopted as a simple technique to probe the formation of a skyrmion phase in non-centrosymmetric patterned films [55-56]. Given the ability to detect the magnetic phases, magnetoresistance measurements have been used to construct magnetic phase maps (Fig. 2.9b) like those typically resulting from inspecting the domain morphology by means of real or reciprocal space imaging techniques. In the case of MnSi nanowires [55-56], it was shown that the skyrmion phase was extended to lower temperatures and matches the previous results reported for similar non-centrosymmetric magnets.

2.5.3 Skyrmion Dynamics

The topology of skyrmions results in novel domain dynamics when these textures are perturbed with currents [36,38,57-59], thermal gradients [60-62] or microwave fields [63-65]. Until now, skyrmion dynamics have primarily been investigated in DMI skyrmions. For the remainder of this chapter, we detail some of the recent experimental observations and predicted behaviors for these chiral textures.

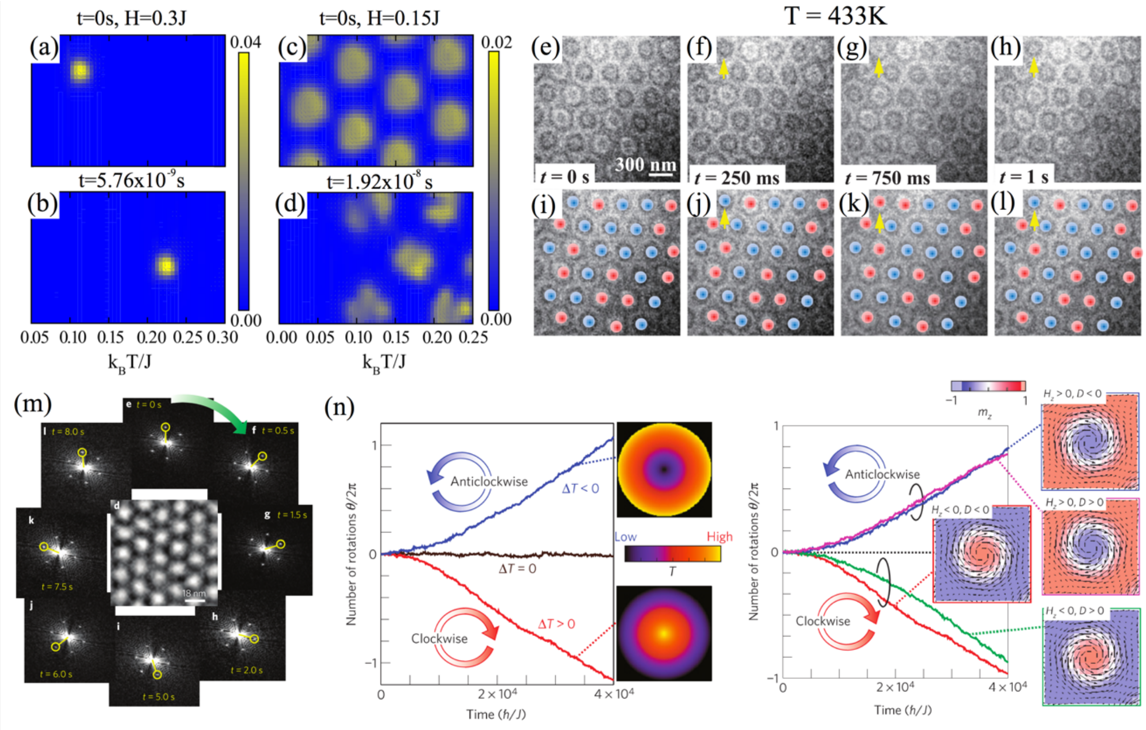

Figure 2.11 – Thermal dynamics of DMI skyrmions. (a, d) The displacement of a skyrmion under a thermal gradient is shown under two magnetic fields: **(a, b)** shows the displacement of a single skyrmion at H = 0.3J and **(c, d)** shows the displacement of the skyrmion lattice at H = 0.15J. **(e, l)** Shows the thermal activation of dipole stabilized skyrmions as a function of time: **(e, h)** shows a mixture of two helicity skyrmions under zero-field at T = 433K and **(i, l)** shows the same frames as **(e, h)** with markers identifying clockwise (blue) and counter-clockwise (red) helicity. A marker arrow shows the fluctuation of a single dipole skyrmion over t = 0-s, 250-ms, 750-ms and 1-s. **(m, o)** Show the rotation of skyrmions induced by a thermal gradient. **(m)** Details the rotation of the 6-fold scatter pattern resulting from the hexagonal lattice of skyrmions in MnSi under H_z = 1750 Oe at 8K. **(n, o)** Simulations of the magnon current density shows **(n)** gyration of skyrmions under different radial thermal gradients hot-to-cold and cold-to-hot. Similar simulations of the magnon current density reveal the independence of field direction and DMI sign in the clockwise and counter-clockwise rotation of DMI skyrmions. Figure reproduced with permission from: **a-d**, ref. 60, © 2013 PRL; **e-l** ref. 61, © 2016 PRB; **m-o,** ref. 62, © 2014 NPS.

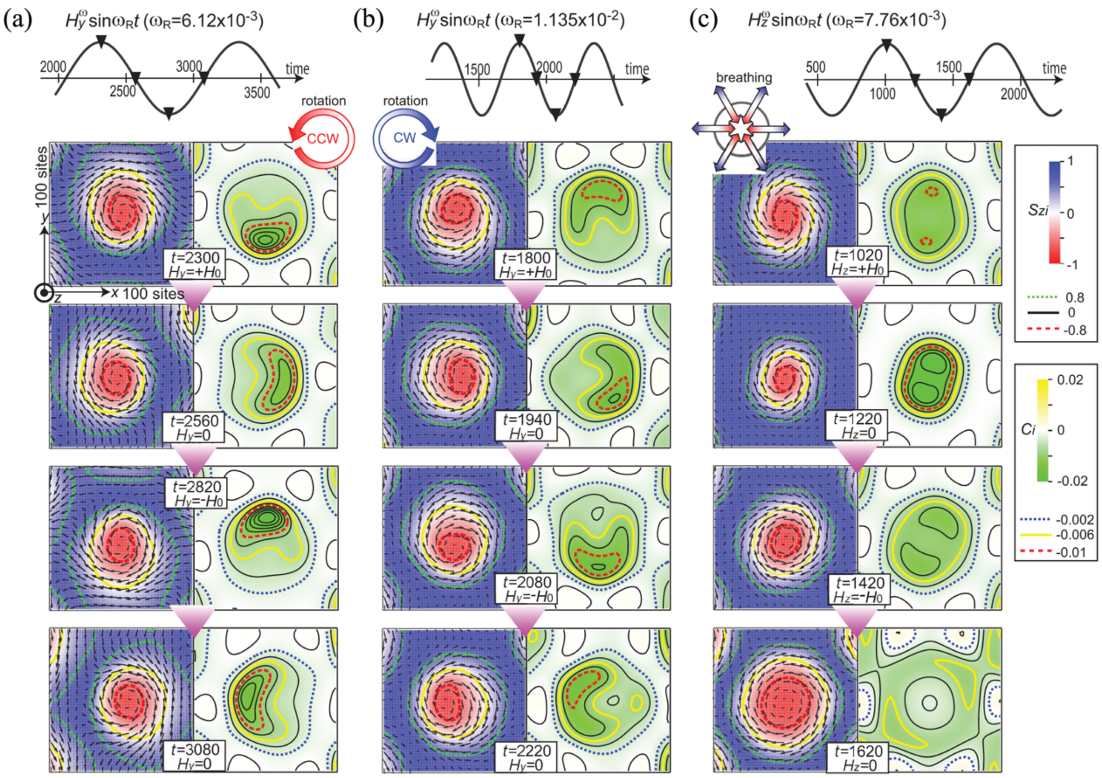

Figure 2.12 – Localized spin wave modes of DMI skyrmions. (a-c) The magnetic spin and spin chirality dynamics under sinusoidal microwave field pulse are detailed for a skyrmion. On the left panel, the magnetic spins are represented by arrows whereas on the right panel to local spins chirality are shown in a color map. The three skyrmion modes **(a)** counter-clockwise, **(b)** clockwise and **(c)** breathing are illustrated at four uniformly spaced time intervals within a single r.f. field pulse, which is shown in the top potion of **(a-c)**. Figure reproduced with permission from: **a-c**, ref. 63, © 2012 PRL.

Skyrmions domains can be displaced with current by means of spin transfer torque that arises from the transfer of angular momentum of the electron to the local magnetization using very low current densities compared to domain wall motion [20]. The typical current density to move a domain wall is in the order of ~$10^{11\text{-}12}$ A/ m^2 [16,20] whereas a skyrmion domain is the order of 10^6 A/m^2 [57-58]. However, to achieve skyrmion speeds comparable to domain walls similar current densities are required. Current induced displacement of skyrmions has been observed in continuous films where the closed packed lattice has been moved [57-58], as well as, isolated skyrmions in patterned wires [36,38]. The first observation of flowing skyrmions under a dc current where reported by X. Z. Yu, et al [57] in FeGe thin platelets at ultralow current densities (<100 A/cm^2) (Fig. 10a-i).

In potential racetrack memory devices, skyrmions have been suggested as the building block memory bit for this non-volatile memory because it possesses technological advantages compared to domain walls. For example, current induced motion of domain walls in patterned thin film wires can encounter pinning effects at physical or energetic artifacts that prevents the domain wall moving past the artifact; however, the topology from skyrmions prevents pinning at artifacts and the chiral texture can move past an artifact without deforming the magnetic domain (Fig. 3.10j, k) [59].

Skyrmions can also exhibit interesting dynamics due to thermal effects, which include skyrmion displacement under a thermal gradient, rotation of the skyrmion textures by means of thermal excitation and even thermal switching. First, DMI skyrmions are predicted to move towards the high-temperature region when placed under a thermal gradient which is opposite to typical diffusion of magnetic domains (Fig. 2.11a-d) [60]. Also the motion of skyrmions is expected to be transverse to the thermal gradient [60] similar to the current induced displacement of skyrmions [20].

In the case of dipole skyrmions, heating the specimen close to its Curie temperature can result in thermal activation of dipole skyrmion which causes the chiral texture to reverse their helicity while keeping the skyrmion feature intact (Fig. 2.11e-l) [61]. Experimentally, the electron beam irradiation from Lorentz TEM can be used to induce a local thermal gradient to drive DMI skyrmions to rotate unidirectionally [62]. This gyration of skyrmions is caused by thermal fluctuations and the rotation direction is dependent on the direction of the applied perpendicular field used to stabilize the DMI skyrmion but not the sign of the DMI [62].

Skyrmions are predicted to exhibit localized spin-wave modes under the application of microwave magnetic fields. These were numerically predicted by Mochizuki [63] to exhibit different skyrmion core dynamics: under in-plane fields the core can rotate either in a clockwise or counterclockwise fashion which depends on one of the two possible skyrmion resonance. Alternatively, if the skyrmions are perturbed with a perpendicular a.c. fields then these will exhibit a core expansion and contraction. These dynamics are detailed in Figure 2.12. Experimentally, the resonant modes branches have been verified in a variety of materials in which DMI skyrmions are stabilized [64, 65] and it has been concluded that resonant properties are independent on whether the DMI skyrmions form in a metallic, semiconducting or insulating material [64]. This is further discussed in the Chapter detailing the ferromagnetic resonance properties of dipole skyrmions.

2.6 References

[1] C. Kittel, *Physical theory of ferromagnetic domains*. Rev. Mod. Phys. **21**, 541 (1949).

[2] Z. Malek and V. Kambersky, *On the theory of the domain structure of thin films of magnetically uni-axial materials*. Czech. J. Phys. **8**, 416 (1958).

[3] C. Kooy and U. Enz, *Experimental and theoretical study of the domain configuration in thin layers of* $BaFe_{12}O_{19}$. Philips, Res. Rep. **15**, 7 (1960).

[4] Kittel, C. Theory of the structure of ferromagnetic domains in films and small particles. *Phys. Rev*. **70**, 965 (1946).

[5] O. Hellwig, A. Berger, J. B. Kortright and E. E. Fullerton, *Domain structure and magnetization reversal of antiferromagnetically coupled perpendicular films*. J. Magn. Magn. Mater. **319**, 13-55 (2007).

[6] M. Seul, L. O. Monar, L. O'Gorman and R. Wolfe, *Morphology and local structure in labyrinthine stripe domain phase.* Science **254**, 1616-1618 (1991).

[7] M. Seul and R. Wolfe, *Evolution of disorder in magnetic stripes domains I. Transverse instabilities and disclination unbinding in lamellar patterns*. Phys. Rev. A **46**, 7519-33 (1992).

[8] M. Seul and R. Wolfe, *Evolution of disorder in magnetic stripes domains I. Hairpins and labyrinth patterns versus branches and comb patterns formed by growing minority component.* Phys. Rev. *A* **46**, 7534 (1992).

[9] Bobeck, H. Properties and device applications of magnetic domains in orthoferrites. *Bell Systems Tech. J.* **46**, 1901 (1967).

[10] Thiele, A. Theory of the static stability of cylindrical domains in uniaxial platelets. *J. Appl. Phys.* **41**, 1139 (1970).

[11] Lin, Y. S., Grundy, J. & Giess, E. A. Bubble domains in magnetostatically coupled garnet films. *Appl. Phys. Lett*. **23**, 485–487 (1973).

[12] Malozemoff, A. P. an Slonczewski, J. C. Magnetic Domain Walls in Bubble Materials p306-314 (1979).

[13] Hubert, A. and Schäfer, R. Magnetic Domains (Springer, Berlin, 1998), p108-134, p.215-290, p306-314, p499-509

[14] Suzuki, T. A study of magnetization distribution of submicron bubbles in sputtered Ho-Co thin films. *J. Magn. Magn. Mater*. 31-34, 1009–1010 (1983).

[15] Cape, J.A. & Lehman, W. Magnetic domain structures in thin uniaxial plates with perpendicular easy axis. *J. Appl. Phys*. **42**, 13 (1971).

[16] S. P. Parkin, M. Hayashi and L. Thomas, *Magnetic domain-wall racetrack memory*, Science **320**, 190-194 (2008).

[17] N. S. Kiselev, A. N. Bogdanov, R. Schafer and U. K. Robler, *Chiral skyrmions in thin magnetic films: new objects for magnetic storage technologies*. J. Phys. D: Appl. Phys. **44**, 392001 (2011).

[18] A. Fert, V. Cros and J. Sampaio, *Skyrmions on the track*. Nature Nanotech. **8**, 152–156 (2013).

[19] T. H. R. Skyrme, *A unified field theory of mesons and baryons*. Nuclear Phys. 31, 556-569 (1962).

[20] N. Nagaosa and Y. Tokura, *Topological properties and dynamics of magnetic skyrmions*. Nature Nano. **8**, 899-911 (2013).

[21] F. Hellman, A. Hoffmann, Y. Tserkovnyak, G. Beach, E. E. Fullerton, C. Leighton, A. MacDonald, D. Ralph, D. Arena, H. Durr, P. Fischer, J. Grollier, J. Heremans, T. Jungwirth, A. Kimmel, B. Koopmans, I. Krivorotov, S. May, A. Petford-Long, J. Rondinelli, N. Samarth, I. Schuller, A. Slavin, M. Stiles, O. Tchernyshyov, A. Thiaville, B. Zink, *Interface induced phenomena in magnetism,* arXiv:1607.00439v2 (2016).

[22] K. H. J. Buschow, Handbook of magnetic materials, (Elsevier, Amsterdam, 2006), Vol. 16.

[23] H. Kronmüler and M. Fänhle, Micromagnetism and microstructure of ferromagnetic solids, (Cambridge University Press, 2003) p14-17.

[24] J. Stöhr and H. C. Siegmann, Magnetism from Fundamental to Nanoscale, Solid State Sciences, (Springer, 2006). P504-506.

[25] B. D. Cullity and C. D. Graham, Introduction to magnetic materials, (Wiley, IEEE Press, 2009) p198-205, p234-237, p.292-294.

[26] K. H. J. Buschow. Handbook of magnetic materials, (Elsevier, Amsterdam, 2015), p259.

[27] I. Dzyaloshinskii*, A thermodynamic theory of "weak" ferromagnetism of antiferromagnetics*. J. Phys. Chem. Solids **4**, 241–255 (1958).

[28] T. Moriya, *Anisotropic superexchange interaction and weak ferromagnetism*. Phys. Rev. Lett. **120**, 91–98 (1960).

[29] S. Mühlbauer, B. Binz, F. Jonietz, C. Pfleiderer, A. Rosch, A. Neubauer, R. Georgii and P. Böni. *Skyrmion lattice in a chiral magnet*. Science **323**, 915-919 (2009).

[30] W. Münzer, A. Neubauer, T. Adams, S. Mühlbauer, C. Fran, F. Jonietz, R. Georgii, P. Böni, B. Pedersen, M. Schmidt, A. Rosch and C. Pfleiderer. *Skyrmion lattice in the doped semiconductor FeCoSi*, Phys. Rev. *B*. **81**, 041203(R) (2010).

[31] X. Z. Yu, Y. Onose, N. Kamazawa, J. H. Park, J. H. Han, Y. Matsui, N. Nagaosa and Y. Tokura. *Real-space observation of a two-dimensional skyrmion crystal*. Nature **465**, 901–904 (2010).

[32] X. Z. Yu, N. Kanazawa, Y. Onose, K. Kimoto, W. Z. Zhang, S. Ishiwata, Y. Matsui and Y. Tokura. *Near room-temperature formation of a skyrmion crystal in thin-films of the helimagnet FeGe.* Nat. Mater. **10**, 106-109 (2011).

[33] K. Shibata, X. Z. Yu, T. Hara, D. Morikawa, N. Kanazawa, K. Kimoto, S. Ishiwata, Y. Matsui and Y. Tokura, *Towards control of the size and helicity of skyrmions in helimagnet alloys by spin-orbit coupling*, Nature Nano. **8**, 723-728 (2013).

[34] S. Seki, X. Z. Yu, S. Ishiwata and Y. Tokura, *Observation of skyrmions in a multiferroic material.* Science **336**, 198-201 (2012).

[35] Y. Tokunaga, X. Z. Yu, J. S. White, H. M. Rønnow, D. Morikawa, Y. Taguchi and T. Tokura, *"A new class of chiral materials hosting magnetic skyrmion beyond room temperature",* Nature Comm. **6**, 7638 (2015).

[36] W. Jiang, P. Upadhyaya, W. Zhang, G. Yu, M. B. Jungfleisch, F. Y. Fradin, J. E. Pearson, Y. Tserkovnyak, K. L. Wang, O. Heinonen, S. G. E. te Velthuis, A. Hoffmann. *Blowing Magnetic Skyrmion Bubbles.* Science **349**, 283 (2015).

[37] C. Moreau-Luchaire, C. Moutafis, N. Reyren, J. Sampaio, C. A. F. Vaz, N. Van Horne, K. Bouzehouane, K. Garcia, C. Deranlot, P. Warnicke, P. Wohlhüter, J.-M. George, M. Weigand, J. Raabe, V. Cros and A. Fert. *Additive interfacial chiral interaction in multilayers for stabilization of small individual skyrmions at room temperature,* Nature Nanotech. **11**, 444-448 (2016).

[38] S. Woo, K. Litzius, B. Krüger, M.-Y. Im, L. Caretta, K. Richter, M. Mann, A. Krone, R. M. Reeve, M. Weigand, P. Agrawal, I. Lemesh, M.-A. Mawass, P. Fischer, M. Kläui and G. S. D. Beach. *Observation of room-temperature magnetic skyrmions and their current-driven dynamics in ultrathin metallic ferromagnets*. Nature Mat. **15**, 501-506 (2016).

[39] X. Z. Yu, M. Mostovoy, Y. Tokunaga, W. Zhang, K. Kimoto, Y. Matsui, Y. Kaneko, N. Nagaosa and Y. Tokura. *Magnetic stripes and skyrmions with helicity reversals*. Proc. Natl Acad. Sci. USA **109**, 8856–8860 (2012).

[40] X. Z. Yu, K. Shibata, W. Koshibae, Y. Tokunaga, Y. Kaneko, T. Nagai, K. Kimoto, Y. Taguchi, N. Nagaosa and Y. Tokura. *Thermally activated helicity reversal of skyrmions*. Phys. Rev. *B* **93**, 134417 (2016).

[41] J. C. T Lee, J. J. Chess, S. A. Montoya, X. Shi, N. Tamura, S. K. Mishra, P. Fischer, B. J. McMorran, S. K. Sinha, E. E. Fullerton, S. D. Kevan and S. Roy. *Synthesizing skyrmion bound pairs in Fe-Gd films*. Appl. Phys. Lett. **109**, 022402 (2016).

[42] T. Okubo, S. Chung and H. Kawamura, *Multiple-q states and the skyrmion lattice of the triangular-lattice heisenberg antiferromagnet under magnetic fields*. Phys. Rev. Lett. **108**, 017206 (2012).

[43] S. Heinze, K. von Bergmann, M. Menzel, J. Brede, A. Kubetzka, R. Wiesendanger, G. Bihlmayer and S. Blüger. *Spontaneous atomic-scale magnetic skyrmion lattice in two dimensions.* Nature Phys. **7**, 713-718 (2011).

[44] M. C. Langner, S. Roy, S. K. Mishra, J. C. T. Lee, X. W. Shi, M. A. Hossain, Y.-D. Chuang, S. Seki, Y. Tokura, S. D. Kevan and R. W. Schoenlein, Coupled skyrmion sublattices in Cu_2OSeO_3, Phys. Rev. Lett. **112**, 167202 (2014).

[45] Ezawa, Phys. Rev. Lett. **105**, 197202 (2010).

[46] Seki and Mochizuki, Skyrmions in Magnetic Materials (Springer, 2016), p3.

[47] A. Neubauer, C. Pfleiderer, B. Binz, A. Rosch, R. Ritz, P.G. Niklowitz and P. Böni. *Topological hall effect in the A Phase of MnSi.* Phys. Rev. Lett. **102**, 186602 (2009).

[48] T. Schulz, R. Ritz, A. Bauer, M. Halder, M. Wagner, C. Franz, C. Pfleiderer, K. Everschor, M. Gasrt and A. Rosch. *Emergent electrodynamics of skyrmions in a chiral magnet.* Nat. Phys. **8**, 301-304 (2012).

[49] Y. Li, N. Kanazawa, X. Z. Yu, A. Tsukazaki, M. Kawasaki, M. Ichikawa, X. F. Jin, F. Kagawa and Y. Tokura. *Robust formation of skyrmions and topological hall effect anomaly in epitaxial MnSi*. Phys. Rev. Lett. **110**, 117202 (2013).

[50] D. Liang, J. P. DeGrave, M. J. Stolt, Y. Tokura and S. Jin. *Current-driven dynamics of skyrmions stabilized in MnSi nanowires revealed by topological Hall effect*. Nat. Comm. **6**, 8217 (2015).

[51] N. Kanazawa, Y. Onose, T. Arima, D. Okuyama, S. Wakimoto, K. Kakurai, S. Ishiwate and Y. Tokura. *Large topological hall effect in a short-period helimagnet MnGe*. Phys. Rev. Lett. **106**, 156603 (2011).

[52] S. X. Huang and C. L. Chien, *Extended skyrmion phase in epitaxial FeGe(111) thin films*. Phys. Rev. Lett. **108**, 267201 (2012).

[53] J. Matsuno, N. Ogawa, K. Yasuda, F. Kagawa, W. Koshibae, N. Nagaosa, Y. Tokura and M. Kawasaki. *Interface-driven topological hall effect in* $SrRuO_3$*-*$SrIrO_3$ *bilayer*. Sci. Adv. **2**, E1600304 (2016).

[54] S. A. Meynell, M. N. Wilson, J. C. Loudon, A. Spitzig, F. N. Rybakov, M. B. Johnson, and T. L. Monchesky, *Hall effect and transmission electron microscopy of epitaxial MnSi thin films*, Phys. Rev. B **90**, 224419 (2014).

[55] H. Du, J. P. DeGrave, F. Xue, D. Liang, W. Ning, J. Yang, M. Tian, Y. Zhang and S. Jin. *Highly stable skyrmion state in helimagnet MnSi nanowires*. Nano Lett. 14, 2026-2032 (2014).

[56] H. Du, D. Liang, C. Jin, L. Kong, M. J. Stolt, W. Ning, J. Yang, Y. Xing, J. Wang, R. Che, J. Zang, S. Jin, Y. Zhang and M. Tian. *Electric field probing of field-driven cascading quantized transitions of skyrmion cluster states in MnSi nanowires*. Nat. Comm. 6, 7637 (2015).

[57] X. Z. Yu, N. Kanazawa, W. Z. Zhang, T. Nagai, T. Hara, K. Kimoto, Y. Matsui, Y. Onose and Y. Tokura*. Skyrmion flow near room temperature in an ultralow current density.* Nature Comm. **3**, 988 (2012).

[58] X. Z. Yu, Y. Tokunaga, Y. Kaneko, W. Z. Zhang, K. Kimoto, Y. Matsui, Y. Taguchi and Y. Tokura. *Biskyrmion states and their current-driven motion in a layered manganite.* Nature Comm. **5**, 3198 (2014).

[59] J. Sampaio, V. Cros, S. Rohart, A. Thiaville and A. Fert, Nucleatio, stability and current-induced motion of isolated magnetic skyrmions in nanostructures, Nature Nano. 8, 839-844 (2013).

[60] L. Kong and J. Zang, *"Dynamics of an insulating skyrmion under a temperature gradient",* Phys. Rev. Lett. **111**, 067203 (2013).

[61] X. Z. Yu, K. Shibata, W. Koshibae, Y. Tokunaga, Y. Kaneko, T. Nagai. K. Kimoto, Y. Taguchi, N. Nagaosa and Y. Tokura, "*Thermally activated helicity reversals of skyrmions*", Phys. Rev. B. **93**, 134417 (2016).

[62] M. Mochizuki, X. Z. Yu, S. Seki, N. Kanazawa, W. Koshibae, J. Zang, M. Mostovoy, Y. Tokura and N. Nagaosa, "*Thermally driven ratchet motion of a skyrmion microcrystal and topological magnon Hall effect*", Nature Mat. **13**, 241-246 (2014).

[63] M. Mochizuki, "*Spin-wave modes and their intense excitation effects in skyrmion crystals*", Phys. Rev. Lett. **108**, 017601 (2012).

[64] T. Schwarze, J. Waizner, M. Garst, A. Bauer, I. Stasinopoulos, H. Berger, C. Pfleiderer and D. Grundler, "*Universal helimagnon and skyrmion excitation in metallic, semiconducting, and insulating chiral magnets*" Nature Mat. **14**, 478-483 (2015).

[65] Y. Onose, Y. Okamura, S. Seki, S. Ishiwata, and Y. Tokura, "*Observation of magnetic excitations of skyrmion crystal in helimagnetic insulator Cu2OSeO3*" Phys. Rev. Lett. **109**, 037603 (2012).

Chapter 3

Experimental Techniques

The various experimental techniques used to grow, optimize and characterize the magnetic, ferromagnetic and transport properties of the Fe/Gd specimens investigated are presented, including the various imaging techniques used to map the domain configurations under different temperature and applied magnetic fields. Since some characterization and experiments required films be patterned into thin film wires, photolithography fabrication was employed to make the transport devices.

3.1 Thin Film Depositions

The thin film Fe/Gd multilayers detailed in this thesis are grown by means of d.c. magnetron sputter deposition technique. This method consists of removing atoms from ultra-pure elemental materials, commonly referred to as 'targets' and transferring them onto a substrate of choice. To remove atoms from the solid target material, an inert gas is

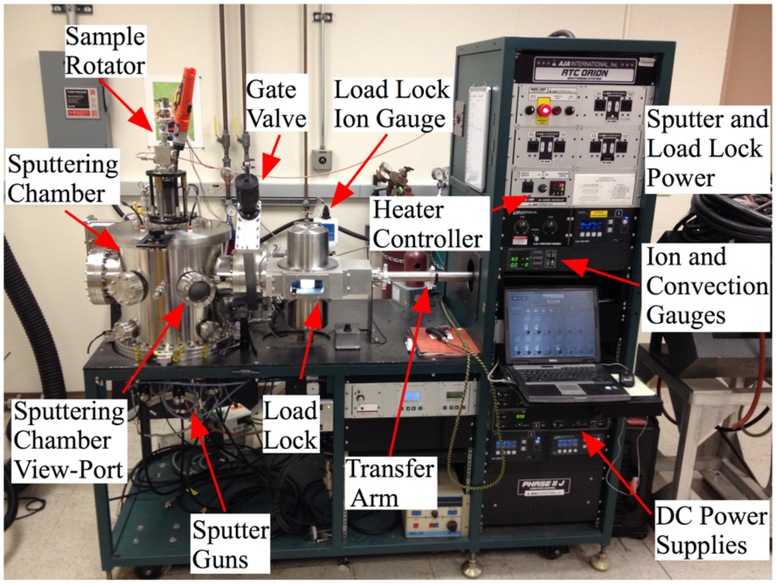
AJA ATC Orion - Magnetron Sputtering Tool

Figure 3.1 – Sputtering tool. Shows an image of the AJA ATC Orion magnetron sputter deposition tool used to grow the Fe/Gd specimens detailed in this thesis. Several components are identified in the image. The rack contains most power supplies and controllers which are computer controlled to facilitate the precise depositions in the sputter chamber.

introduced into the sputter chamber while the target is connected to a negatively charged electrode (cathode) and the substrate is connected to a positively charged electrode (anode). The most common inert gas used is Argon (Ar). A plasma is then created by ionizing the inert gas which occurs when a stray electron e^- near the cathode is accelerated towards the anode and collides with a neutral Ar atom converting it into a positively charged ion (Ar^+). As a whole, this process yields:

$$Ar + e^- \rightarrow Ar^+ + 2e^- \tag{3.1}$$

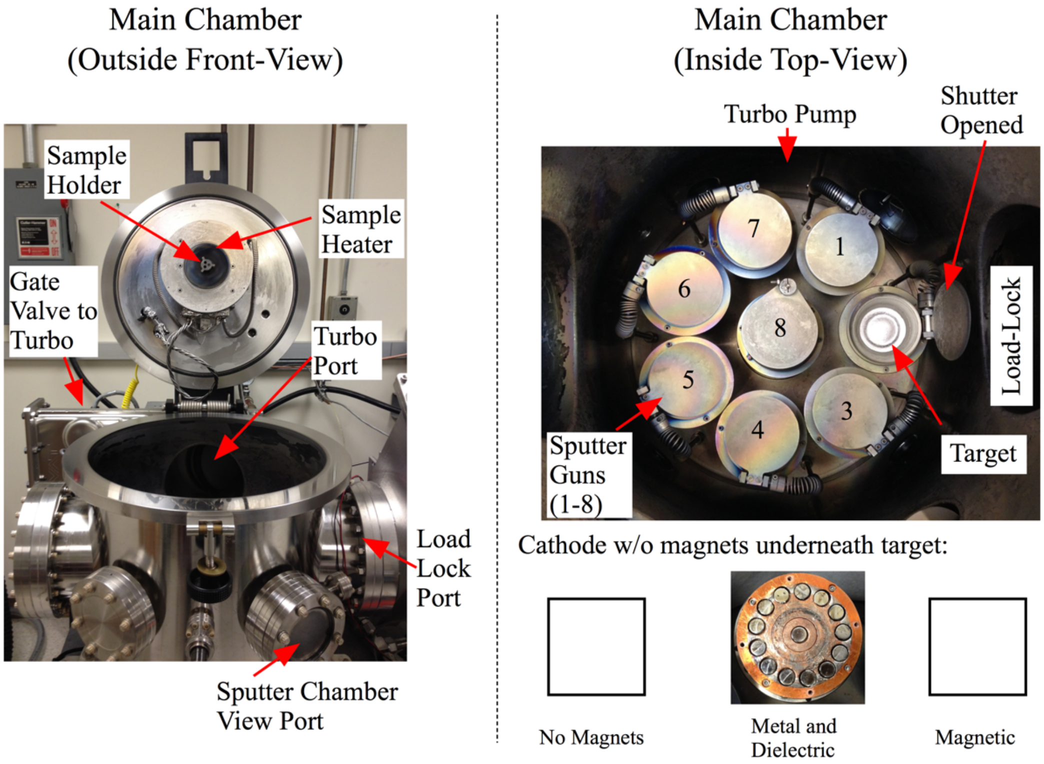

Figure 3.2 – Main Sputter Chamber. Components inside the sputter chamber are detailed with emphasis on the sputter guns and the location of the deposition puck where the sample is mounted. The sputter tool has eight sputter guns where metal and insulating solid targets can be placed. The cathode underneath the target is shown without magnets and with two possible magnet configurations for different types of targets. The magnets arranged on the outside all point in the same direction and the magnet in the center points opposite – this configuration is used for non-ferromagnets targets. A soft metal core in the center of the cathode when ferromagnets are used.

At this point the Ar^{+} ions will accelerate towards the cathode where the material target sits. Upon collision, neutral particles from the target will be ejected as well as additional electrons e^{-}. Since the targets sit inside confined housings, termed ‘guns’, the target atom are directed toward the substrate, but these can potentially coat any surface inside the sputter tool. The extra electrons continue supplying the plasma that is confined above the target by a magnetic field generated by magnets below the target (hence the term magnetron sputtering) and thus the continued formation of charged ions. As long there are enough collisions, the plasma becomes self-sustaining.

Figure 3.1 shows the AJA ATC Orion magnetron sputter tool utilized to grow the Fe/Gd films. The system is composed of (i) a main chamber which houses the targets and is where depositions are carried out, (ii) a load-lock chamber houses multiple sample holder, (iii) a transfer arm to move samples to-and-from the load-lock and main chamber and (iv) the relevant power distribution modules. Inside the main chamber (Fig. 3.2), the targets are housed inside one of the potential eight guns which have a shutter to control and limit material coatings on the substrate. Figure 3.2 shows the inside housing of one of the guns were the plasma is confined when the target is light. The substrate is held in a sample holder suspended over the guns at the center of the main chamber (Fig. 3.2). Since most guns are positioned around the wall of the chamber, the sample holder is continuously rotated during the deposition to obtain uniform thin film coatings. Furthermore, the sputter tool is pumped to UVH pressures (~1x10^{-9} Torr) before any films are deposited to obtain high quality films. The chamber background pressure is monitored using an ion gauge, whereas the deposition pressure is monitored using a convection gauge.

To deposit the Fe/Gd multilayers, we use Fe (99.95%) and Gd (99.9%) pure element targets and alternate the deposition of individual layers of each material of the desired thickness. For most films presented in this work, the individual layers are a few monolayers thick (< 0.5 nm). To appropriately grow each layer, a deposition calibration is carried out prior to determine the rate of material transfer from target-to-substrate under specific chamber conditions (Ar gas content, chamber pressure, gun power and gun position) to be replicated when the Fe/Gd films are grown. All the films presented in this thesis are grown at room temperature under 3mTorr Ar pressure. The deposition rate is determined via small angle x-ray reflectivity from a single material films where the thickness is divide by the time of deposition. Further details are explained in Chapter 2.2.5. To protect the films from corrosion a 5nm Ta (99.9%) seed and capping layer was used. Given the range of different studies performed, the samples were deposited on: native oxide Silicon (3.9mm x 4.1mm), Silicon with a 300nm thermal oxide (10mm x 8mm), SiN TEM grids (window: 20nm x 200μm x 200μm, frame: 0.5mm x 0.5mm) and SiN membranes (window:100nm x 1mm x 1mm, frame: 5mm x 5mm).

3.2 Thin Film Characterization

The thin films magnetic, resonant, transport and structural properties were characterized using a suite of different techniques that allows us to quantify magnetization, anisotropy, coercivity field, saturation field, ferromagnetic resonance frequencies resulting from non-homogeneous and uniform magnetization states, magnetic damping, anisotropic magneto-resistance, Hall resistance, structure of the multilayer and total film thickness.

3.2.1 Magnetometry

The magnetic loops of the thin film specimens were obtained using two different techniques: (i) vibrating sample magnetometer (VSM) and (ii) magneto optical Kerr effect (MOKE) magnetometer. The first is suited for profiling and quantifying the volume magnetization of a film, whereas the latter is best for characterizing the surface magnetization within the optical penetration depth.

Vibrating sample magnetometry is based on Faraday's law of electromagnetic induction, which states that any change in the magnetic field of a coil will result in an electromotive force to be induced in the coil. A vibrating sample magnetometer consists of a linear motor that moves a magnetic specimen, at a specific frequency ($f \sim 40$ Hz), through a collection coil were the induced voltage is detected. The time-dependent voltage is given by:

$$V_{coil} = \frac{d\Phi}{dt} = \frac{d\Phi}{dz}\frac{dz}{dt} \tag{3.2}$$

where Φ is the magnetic flux in the coil, z is the vertical position of the sample with respect to the coil and t is time [1]. For a sinusoidal oscillating sample position, the voltage is given by:

$$V_{coil} = 2\pi f CmA \sin(2\pi f t) \tag{3.3}$$

where C is the coupling constant, m is the d.c. moment of the sample, A is the amplitude of the oscillation and f is the oscillation frequency [1].

The sample is attached to the end of a carbon-fiber rod and its orientation in the direction of the applied magnetic field, allows us one to characterize either the in-plane or perpendicular magnetization field dependence. The sample is then positioned at the vertical center of the detection coil, where the specimen is driven sinusoidally. This induces a voltage that is amplified, locked-in and averaged. In overall, the technique yields magnetic sensitivity (< 10^{-6} emu) with 1 sec averaging [1].

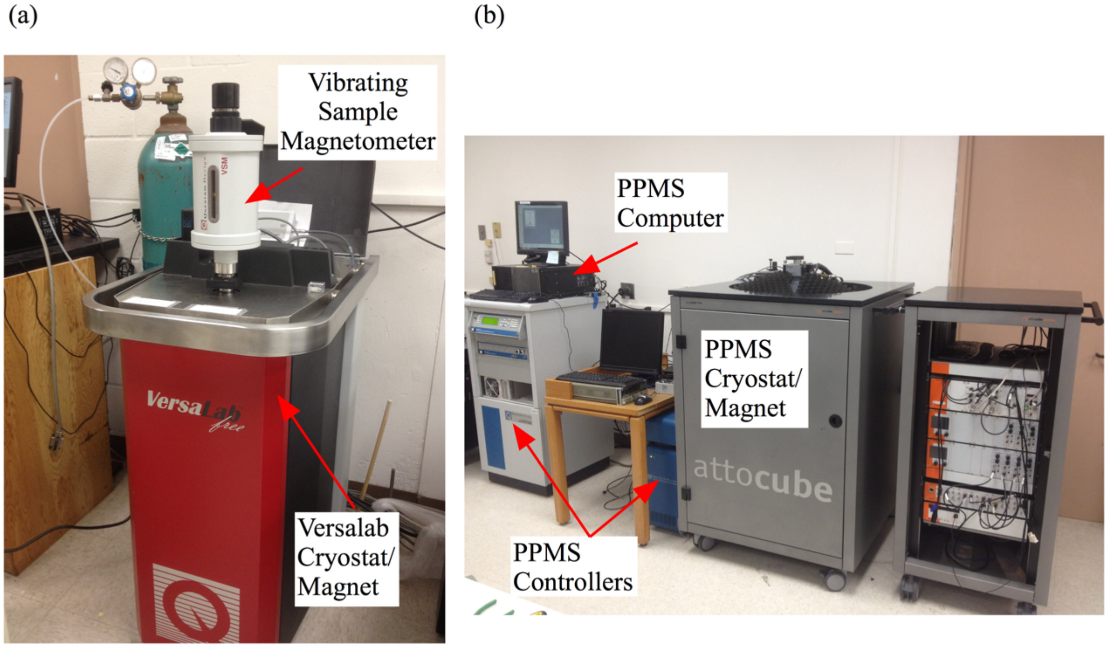

Figure 3.3 – Quantum Design Physical Property Measurement System (PPMS) and Versalab with Vibrating Sample Magnetometer (VSM). The **(a)** Versalab and **(b)** PPMS cryogen chambers with superconducting magnets are shown with the vibrating sample magnetometer on **(a)**. The sample chamber is positioned at the lower portion of the cryogen chamber.

Figure 3.3 shows the *Quantum Design* vibrating sample linear motor and the detection coil that is used in combination with a *Quantum Design* cryogen chamber for varying temperature and magnetic fields. We utilize a *Physical Property Measurement System* (*PPMS*) cryostat which allows measurements from 1.9 K to 400 K with magnetic fields up to 9T (Fig. 3.3a) and a *Versalab* cryostat with variable temperatures from 50 K to 400 K with magnetic fields up to 3T (Fig. 3.3b).

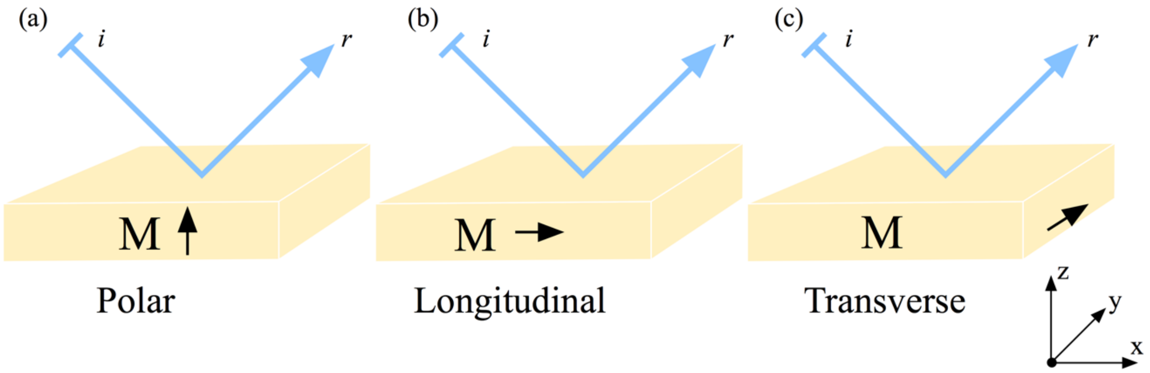

Figure 3.4 – MOKE configurations. (a) Magnetization is perpendicular to the reflection surface. **(b)** Magnetization is parallel to the reflection surface and is in the same cross-section as the incident beam. **(c)** Magnetization is parallel to the reflection surface and is transverse to the incident beam.

MOKE magnetometry is based on the magneto-optical Kerr effect, which dictates that light reflected from the surface of a magnetic specimen will undergo changes in polarization and intensity. The MOKE effect results from difference absorption in magnetic circular dichroism. Depending on the orientation of the magnetization with respect to the direction of the incident light, all three magnetization vector components can be profiled [2,3]. These configurations are denoted: polar, longitudinal and transverse MOKE (Fig. 3.4). Since the Kerr effect is a surface probe, it is restricted to the penetration depth of light inside a material which is given by the skin depth (10-20 nm).

Figure 3.5 shows a photograph of the table-top polar-MOKE measurement set-up and the corresponding schematic. The light emitted from a diode laser (5mW, λ=650nm) travels to a mirror which directs the light into a Glan-Thompson polarizer that is chopped at a reference frequency for lock-in detection (Stanford Research Systems, SR830 DSP). Afterwards, the light is reflected with a mirror into a beam-splitter and the beam aperture

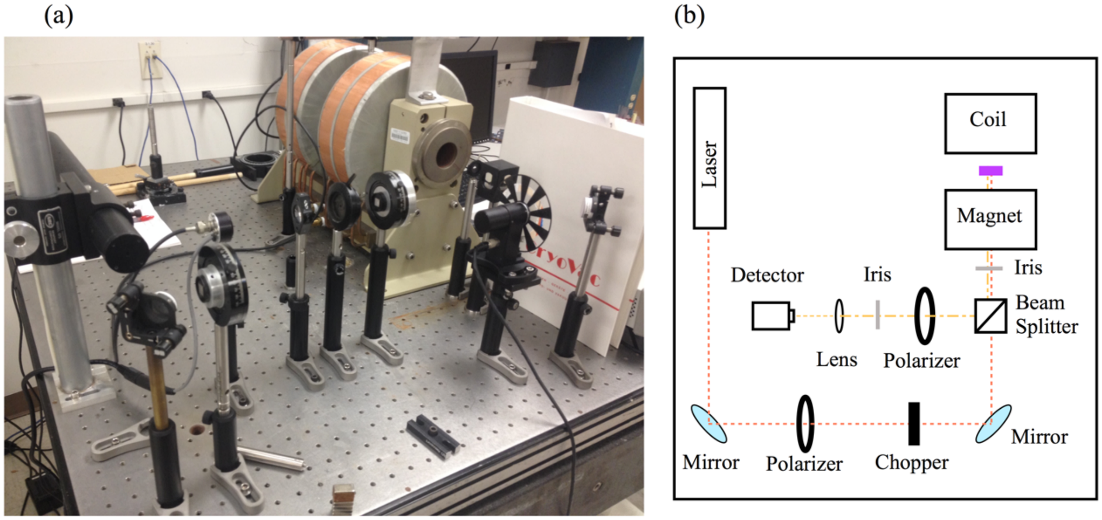

Figure 3.5 – Polar MOKE magnetometer.(a, b) Shows a tabletop polar MOKE magnetometer and its schematic details the light ray path that travels from the laser source to the sample and then the reflected light is directed onto a photo-diode detector.

is reduced with an iris before reaching the magnetic specimen. The magnetic specimen lies perpendicular to magnetic field produced by the electromagnet (GMW Model 5403). Once beam is reflected off the sample, it travels toward a second Glan-Thompson polarizer after being reflected off from the beam-splitter. Next, the beam aperture is reduced again using an iris before it is focused with a lens onto a photo-diode detector synched with the lock-in amplifier. The electromagnet is powered by a bipolar power supply (Kepco Model BOP 100-4M, L Load) and the magnetic field is monitored using a Hall sensor probe (Lakeshore Model 455 DSP). The entire measurement set-up is computer controlled.

3.2.2 Ferromagnetic Resonance

To study the resonant modes resulting from non-homogenous magnetization states and the uniform magnetization state, ferromagnetic resonance (FMR) measurements were performed using a coplanar waveguide technique in fixed frequency mode [4,5]. This technique provides access to a materials effective magnetization, effective damping, effective anisotropy, intrinsic anisotropy and resonant modes from magnetic domains.

When a magnetic specimen is exposed to a static magnetic field, the magnetization $\boldsymbol{M}$ will precess in the direction of the field before a relaxation mechanism damps the precession and the total magnetic moment aligns in the direction of the magnetic field. The precessional motion of the magnetization under a magnetic field is described in terms of the Landau-Lifshitz-Gilbert equation,

$$\partial_t \boldsymbol{M} = -\frac{\gamma}{1+\alpha^2}\,\boldsymbol{M} \times \boldsymbol{H_{eff}} - \frac{\gamma\alpha}{1+\alpha^2}\,\boldsymbol{M} \times \left(\boldsymbol{M} \times \boldsymbol{H_{eff}}\right) \tag{3.4}$$

where the first term of Eq. 3.4 describes the torque acting on the magnetization $\boldsymbol{M}$ due to an effective field $\boldsymbol{H_{eff}}$ and the second term describes the dissipative process that causes the magnetization $\boldsymbol{M}$ precession to damp out in the direction of the effective field $\boldsymbol{H_{eff}}$. The gyromagnetic ratio γ and the damping α are material dependent constants. The effective field $\boldsymbol{H_{eff}}$ describes the total magnetic field acting on the magnetization $\boldsymbol{M}$,

$$\boldsymbol{H_{eff}} = \nabla \cdot \int_{V'} \left(\frac{\nabla \cdot \mathbf{M}}{|\boldsymbol{r}-\boldsymbol{r}'|}\right) \mathrm{d}\mathbf{r}' + H_{ext}\hat{\boldsymbol{k}} + \frac{H_k}{M_S}\left(\hat{\boldsymbol{k}} \times \boldsymbol{M}\right)\hat{\boldsymbol{k}} + 2\frac{A}{M_S^2}\nabla^2 \boldsymbol{M} \tag{3.5}$$

which describes the magnetostatic, Zeeman field along the z-axis, anisotropy and exchange energy.

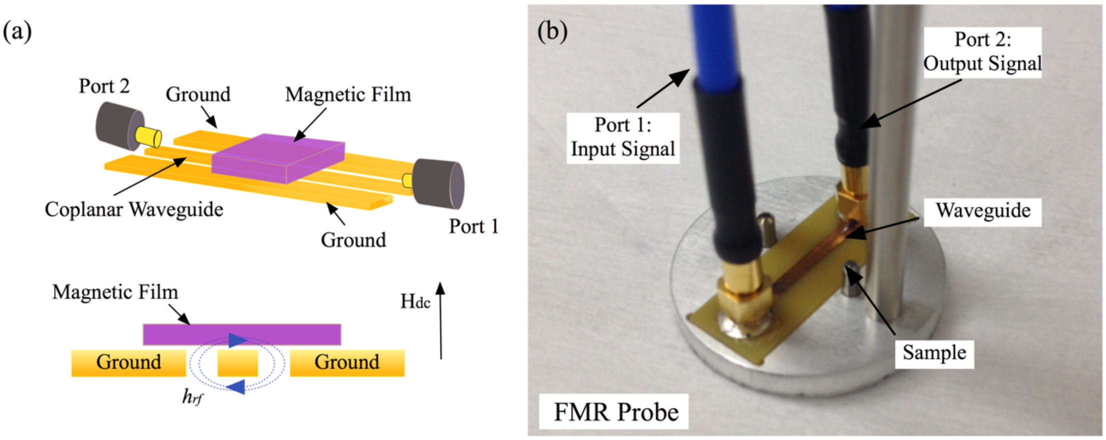

Figure 3.6 – Ferromagnetic resonance. (a, b) Displays the schematic of the coplanar waveguide and an image of the bottom portion of the ferromagnetic resonance probe. The probe has a coplanar waveguide attached to the bottom where the sample is mounted facedown using the sample holder.

Ferromagnetic resonance is based on pumping a magnetic specimen with an *r.f.* field to match the precessional frequency and thus allows H_{eff} to be determined.

Figure 3.6 shows a schematic of the coplanar waveguide with is used to generate the *r.f.* fields. In this geometry, the magnetic specimen is affixed to the top and center of the waveguide and the *r.f.* field results from inputting the signal along the center line of the waveguide. Here, the *r.f.* field lies along the plane of the waveguide and the two grounds next to the center line acts as field flux concentrators. The absorption spectrum ΔS_{12} is obtained from an Agilent Vector Network Analyzer E8363B which provides and collects the incident, reflected and transmitted signals as standard S parameters as a function of frequency. The coplanar waveguide is affixed to a custom probe designed to be used in conjunction with a *Quantum Design PPMS* or *Versalab* cryostat for applying d.c. magnetic fields and varying temperature (Fig. 3.3).

3.2.3 Anisotropic Magnetoresistance

In ferromagnetic materials, the electrical resistance is dependent on the scatter angle between the current and the magnetization (Fig. 3.7). This effect is called anisotropic magnetoresistance. Lower scattering of conduction electrons is expected from magnetic moments aligned perpendicular and orthogonal to the current flow, whereas, moments parallel and anti-parallel to the current flow will result in higher scattering. This can be expressed as,

$$R = R_o + \mathit{\Delta} R \cos^2(\theta), \qquad \mathit{\Delta} R = \frac{R^{||} - R^{\perp}}{(R^{||} + 2R^{\perp})/3} \tag{3.6}$$

where R_o is the ordinary resistance, $\mathit{\Delta} R$ is the anisotropy magnetoresistance and θ is the angle between the magnetization and the current. The physical origin of AMR lies in the spin-orbit coupling which results in spin-dependent scattering of conduction electrons [6].

This type of transport measurement is useful for probing difficult to identify magnetic dynamics as well as macroscopic quantum phenomena in ferromagnetic metals. Although we have utilized an array of imaging techniques, see Chapter 2.3, these are not suited to identify minute magnetic information even from high resolution images given some information is usually lost due to the scattering or transmission nature of the imaging technique. By varying the field-orientation relevant to the fixed current direct we can probe the magnetic configurations of the Fe/Gd specimens along all three vector directions to probe the magnetic domain ordering, volume fraction of magnetic domains and domains walls and potential magnetic phase changes.

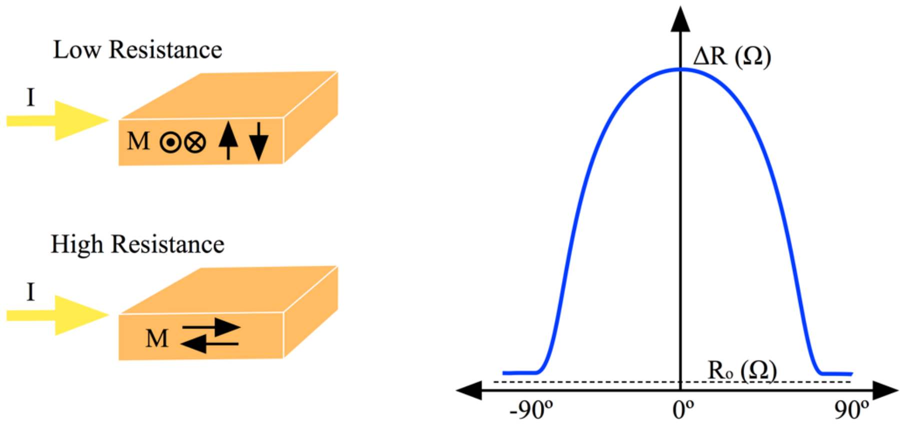

Figure 3.7 – Anisotropic magnetoresistance. (a) Schematic illustrates expected resistance from different configurations of magnetization and current. **(b)** Shows the variation of the anisotropic magnetoresistance as the angle between the fixed current in **(a)** and the varying magnetization from 0^o to $\pm 90^o$.

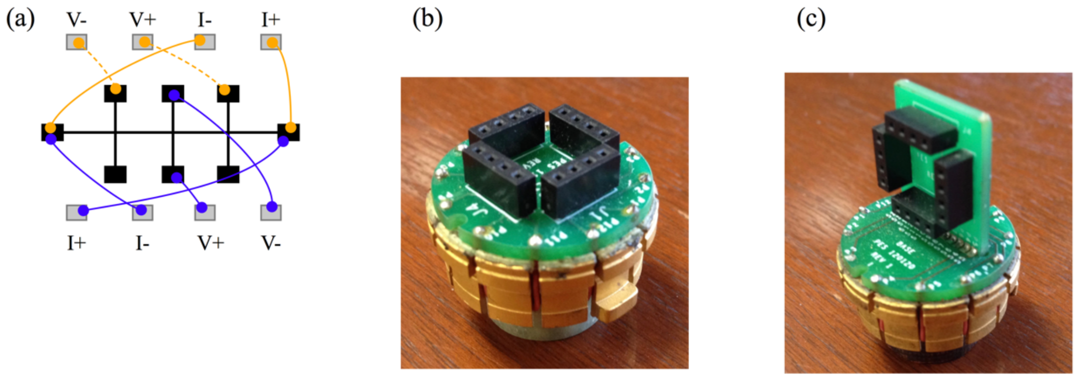

Patterned Thin Film on Chip Holder

Perpendicular Transport Puck

Lontituginal Transport Puck

Figure 3.8 – Sample wiring and transport puck. (a) Shows the wiring schematic for performing both resistivity and Hall resistance measurements on a patterned thin film with eight contact pads. The specimen is mounted onto a chip carrier where the device is affixed and wired. **(b)** Details a transport puck that was designed to have the sample lie on the plane of the puck and perpendicular to the magnetic field. **(c)** Shows a transport puck that holds the chip carrier orthogonal to the puck and in-plane to the magnetic field.

Resistance is measured using the standard 4-point probe technique (Fig. 3.8a) on photo-lithographically defined wires of different widths (1, 5, 10, 20, 50 and 100μm) and fixed lengths (3.5mm). Details on fabrication of the wires is detailed in Chapter 2.4. The *d.c.* and *a.c.* current source is provided through ports inside the *Quantum Design PPMS* cryostat using the Resistivity module. Currents ranging from 1μA to 100μA are used on the wires, with higher currents being used for wider wires. The samples are placed over a transport puck that is inserted into the cryostat (Fig. 3.8b, c). On the transport puck there are four potential channels each consisting of a voltage and a current source (Fig. 3.8b, c). To connect the channel outputs to the sample, Ag wires are soldered on the voltage and current source and then these are connected to the sample using Ag paint.

3.2.4 Hall Resistance

In ferromagnetic materials, the hall resistance ρ_H also refered to as the transverse resistance ρ_{xy}, can exhibit several contributions which arise from different physical mechanisms. In its most general form, the hall resistance is given by

$$\rho_H = \rho_{xy} = \rho_O + \rho_A \tag{3.7}$$

where ρ_O is the ordinary hall effect which is present in all conducting and semiconducting metals and ρ_A is the anomalous hall effect which arises from the magnetic order in the materials. The ordinary hall effect is the result of flowing a current through a metal under the presence of a perpendicular magnetic field. Based on the geometry of Figure 3.9a, the current moving along x-direction can be described as

$$I_x = nqv_xt \cdot w \tag{3.8}$$

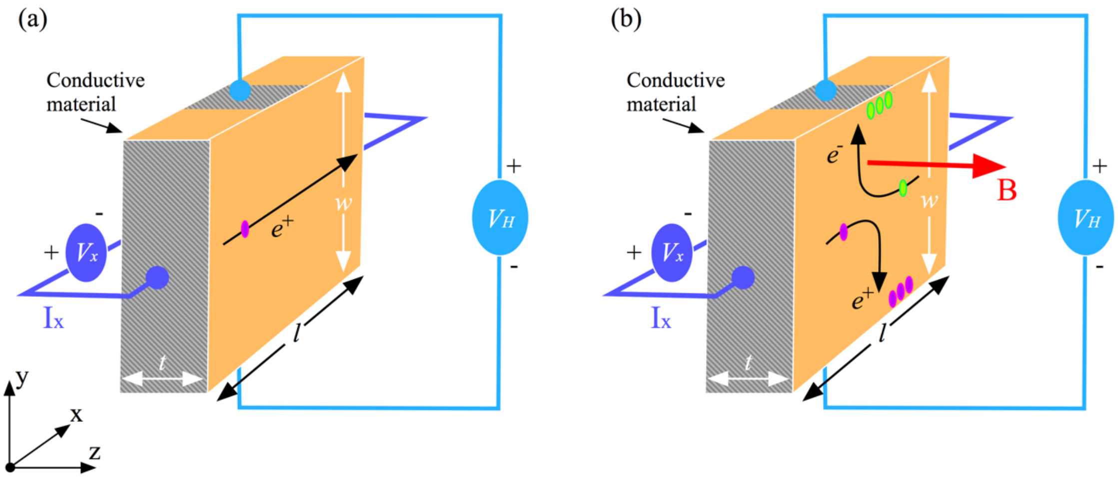

Figure 3.9 – Hall effect. Displays the path the charge carriers will follow across a conductive or semi-conductive material under **(a)** zero-field and a **(b)** field perpendicular to the slab. The path of electrons and holes is shown in **(b)** when these are submitted to a Lorentz force.

where q is the charge carrier, n is the charge carrier density number, v_x is the drift velocity of the charge carriers along the x-direction, $t \cdot w$ is the area of the conduction slab through which the current is pushed. As the charge carriers move along the length of the conducting slab, these will exhibit a Lorenz force $F_L = q\boldsymbol{v}\times \boldsymbol{B}$ that will cause them to deflect toward a side of the slab. Since charge carriers can be electrons or holes, the deflection can be toward the top or bottom of the slab as shown in Fig 3.9b. As charge carriers accumulate along a side of the slab, this produces a transverse electric field E_y which counteracts the Lorentz force. At one point, an equilibrium is reached between both electric and magnetic forces which results in no net flow of charge carries transverse to the direction of the electrical current. This can be expressed as:

$$\boldsymbol{F} = \boldsymbol{F_E} + \boldsymbol{F_L} = q(\boldsymbol{E} + \boldsymbol{v} \times \boldsymbol{B}) = 0 \tag{3.9}$$

$$q\boldsymbol{E} + q\begin{pmatrix} \hat{x} & \hat{y} & \hat{z} \\ v_x & 0 & 0 \\ 0 & 0 & B_z \end{pmatrix} = qE_x\,\hat{x} + q\left(E_y - v_xB_z\right)\hat{y} + qE_z\hat{z} = 0 \tag{3.10}$$

$$E_y = v_xB_z \tag{3.11}$$

The electrical field can be measured as a transverse potential difference V_H between both sides of the slab and takes the form:

$$V_H = \int_0^w E_y d_y = -E_y w \tag{3.12}$$

From equations (2.6), (2.9) and (2.10) it follows that the Hall voltage can be re-written as:

$$V_H = -\frac{I_xB_z}{nqt} \tag{3.13}$$

Based on the slab geometry in Figure 3.9b, if the charge carriers were electrons then the accumulation of negative charges would occur on the top of the slab and we would expect a negative potential difference; conversely, holes would result in positive charge accumulation on the bottom of the slab resulting in a positive voltage difference. In overall, the ordinary Hall effect provides a direct measure of the type of charge carrier and the charge carrier density number of a material.

In magnetic materials, there is an additional Hall voltage contribution that is proportional to the z-component of the magnetization. We recall that the magnetic flux for a magnetic material is given by $\boldsymbol{B} = \boldsymbol{H} + 4\pi\boldsymbol{M_S}$ from which we can re-write the Hall voltage as,

$$V_H = -\frac{I_x}{nqt}(H_z + 4\pi M_z) \tag{3.14}$$

where the first contribution is the ordinary hall effect and the second contribution is the anomalous hall effect. The latter effect is observable in ferromagnetic materials even under zero-field. Since the magnetization changes with magnetic field the anomalous Hall voltage response is proportional to the magnetic hysteresis for perpendicular magnetic fields. Above magnetic saturation, the anomalous Hall voltage remains constant given the magnetization is uniform nd any changes is a result of the ordinary Hall effect.

Hall resistance measurements are simultaneously collected with the resistance measurements using the photo-lithographically defined 8-bar Hall cross detailed in Figure 3.8. This provides a direct one-to-one comparison between both transport measurements and also reduces the measurement time. The details of measurement and wire connectivity to the sample are the same as those detailed in Chapter 3.2.3.

3.2.5 X-ray Reflectometry

To characterize the physical properties of thin films, x-ray reflectivity is a powerful and non-invasive technique that uses electromagnetic radiation with wavelength comparable to the atomic spacing to study information embedded in reflection patterns.

X-ray light is emitted from a source (typically a Cu or Co anode) onto a specimen, where two process can occur: (i) light is absorbed by an atom which results in the ejection of electrons or (ii) light is reflected from the material into a detector. In a crystal material, the light scatters off planes of atoms that are each separated by distance d (Fig. 3.10). To obtain a constructive interference, the X-ray that penetrates the atom planes must travel a whole wavelength inside the material to be in-phase with the wave being reflected off the surface (Fig. 3.10a). This is known as Bragg's law and is expressed as:

$$n\lambda = 2d\sin(\theta) \tag{3.15}$$

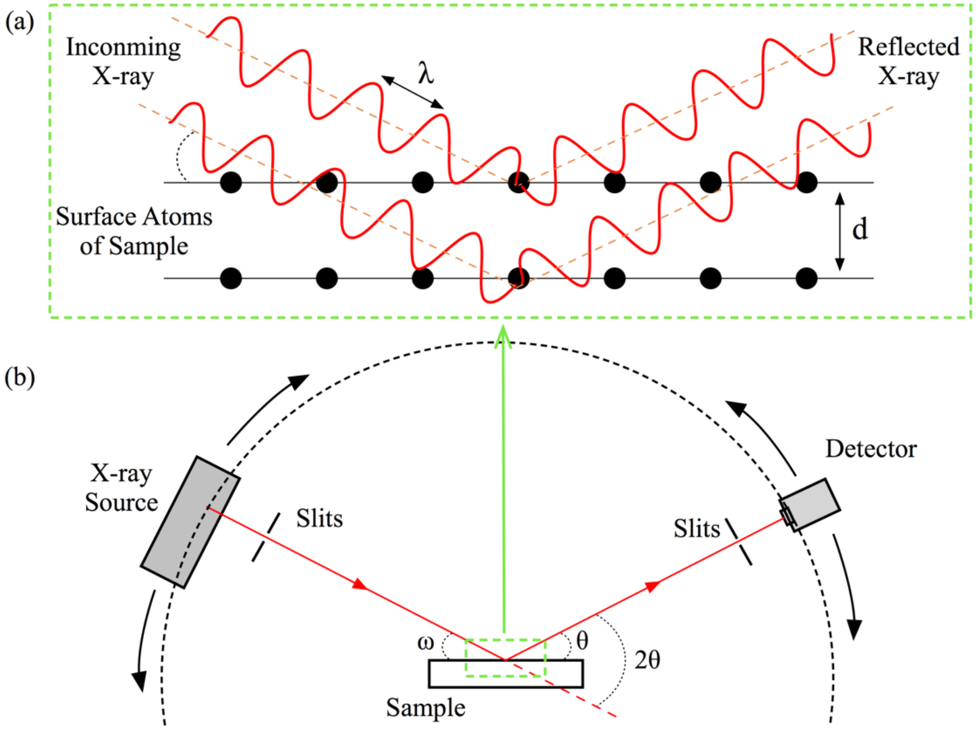

Figure 3.10 – X-ray diffraction. (a) Bragg's law is illustrated with the scattering of two in-phase x-rays incident and reflected off two planes of atoms separated by a distance d. **(b)** The x-ray diffractometers used employed Bragg-Brentano reflection geometry

where n is an integer (n=1, 2, 3…), λ is the wavelength of the x-ray, θ is the angle between the incident x-ray and the surface plane and d is the distance between the planes of atoms. Figure 3.11 shows the small angle reflectivity pattern obtained from a CoZrNb film. At 2θ angles below the critical angle θ_c there is total reflection of the incident x-rays. Then as the incident angle is increased above the critical angle, x-rays begin to penetrate the thin film and we can obtain interference fringes between x-rays scattered from the surface and those scattering off inside the thin film. The periodicity of the fringes is proportional to the thick-

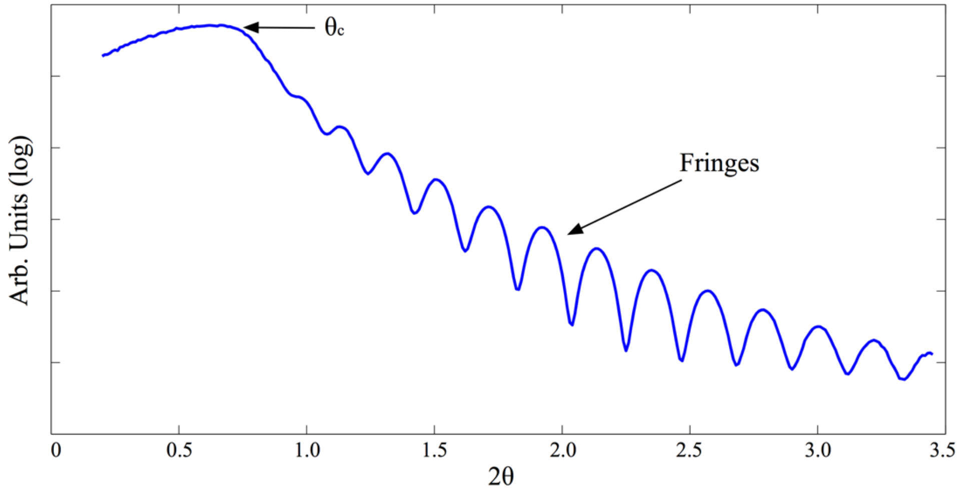

Figure 3.11 – Film thickness. The small angle x-ray scattering from a CoZrNb film is shown over a range of 2θ angles. The well-defined periodic fringes are characteristic of this kind of low angle measurements. Fitting these maxima and minima peaks with Bragg's law allows one to determine the thickness of the film.

ness of the film and the fall of intensity and oscillation decay of the fringes at higher angles provides a measure of the roughness of the film.

We performed x-ray reflectivity using a Bruker Discover D8 diffraction system and a Rigaku x-ray diffraction system with a power rotating anode. X-ray reflectivity was used to calibrate the sputter deposition rate of Ta, Fe and Gd targets prior to depositing the Fe/Gd multilayers. Then, it was used to profile the overall thickness of the Fe/Gd multilayers and determine the order of the layers.

3.3 Imaging Techniques

The temperature and magnetic field dependence of the magnetic domain morphology of the Fe/Gd specimens discussed in this thesis were studied using a variety of real and reciprocal space imaging techniques. Collectively, they have allowed us to identify the magnetic domain wall, observe details field variability of the magnetic domains under different field history, determine field dependent magnetic phase transitions and resolve current and microwave field dynamics of magnetic domains

3.3.1 Lorentz Transmission Electron Microscopy

Transmission electron microscopy (TEM) is an imaging technique employing a beam of high energy electrons (100-1000 keV) as a light source to image features in the order of a few angstroms [7]. The principles of operation are fairly similar to an optical microscope; however, instead of employing the use of glass lenses to focus the light, a TEM uses electromagnetic lenses, e.g. solenoid coils, to steer electrons into a thin beam toward a specimen and onto an image plane. Figure 3.12 shows a simple schematic illustrating the similar ray path between both microscope techniques. In an actual TEM, there are usually several condenser lenses, objective lenses and projector lenses throughout the microscope to optimize the electron beam and resulting image quality. Also, apertures are used at several stages to select specific energy electrons, thus resulting in the ability to control the image contrast. Finally, the image is captured using a CCD camera behind a phosphorescent screen placed at the image plane which emits photons when irradiated with electrons.

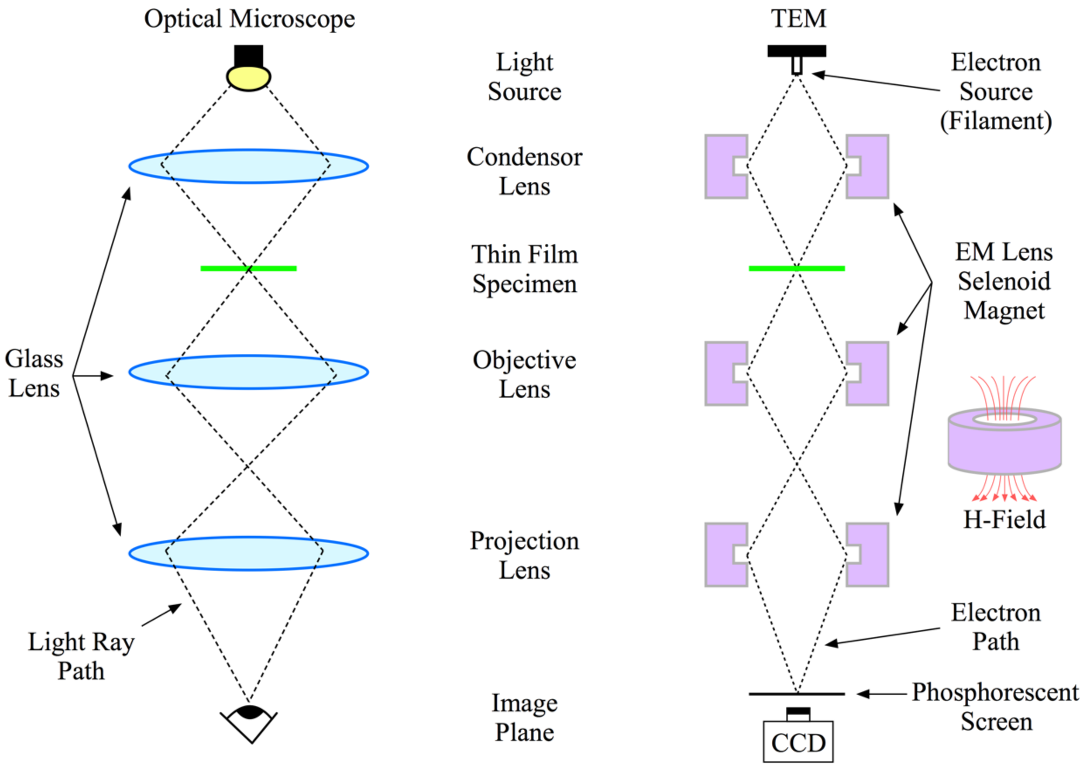

Figure 3.12 – Optical and electron microscope comparison. The ray path of simplified schematics showing both optical and electron microscopes.

A TEM image represents variations of darkness and brightness intensity that directly correlate different thickness averaged densities of the thin film sample. Regions of the sample where fewer electrons are transmitted result in darker areas in the image; conversely, areas where more electrons are transmitted result in brighter areas in the image. When electrons travel through a magnetic specimen, these will exhibit a Lorentz force that will cause the electron to deflect from its original trajectory after being transmitted through the specimen. The Lorentz force is given by

$$\boldsymbol{F_L} = q\boldsymbol{v} \times \boldsymbol{B} \tag{3.16}$$

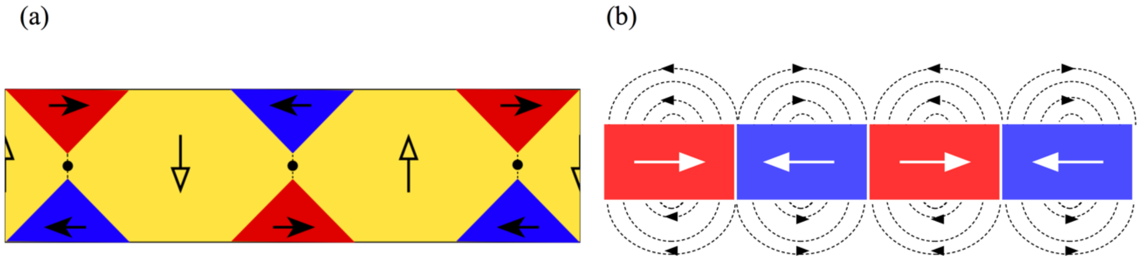

Figure 3.13 – LTEM artifacts from specific domain morphologies. (a) Perpendicular magnetic domains with Néel caps and a Bloch line at the center of the slab. **(b)** Magnetic slab with in-plane magnetic domains.

where $\boldsymbol{v}$ is the velocity of the electron and $\boldsymbol{B}$ is the magnetic induction averaged over the thickness of the magnetic specimen along the trajectory of the electron. From Eq. (2.11), we can expect that only electrons normal to the magnetic induction $\boldsymbol{B}$ field will be subject to a change in trajectory. Due to the nature of the Lorentz force perceived by the electron, this imaging technique is referred to as Lorentz TEM.

In order to resolve the magnetic contrast, there are two main techniques commonly used in Lorentz TEM: Fresnel mode consist of defocusing the image to observe variations of intensity at the domain boundaries [7]. Alternatively, Foucault mode obtains magnetic contrast by blocking light from the objective lens by shifting the aperture off-center while the image is in focus [7]. Each of these techniques allows the retrieval of specific magnetic information: Fresnel mode gives access to the domain wall of magnetic domains, whereas Foucault mode allows mapping the direction of the magnetic domains.

Given the transmission nature of this imaging technique, we can expect a Lorentz TEM image to reveal information from the averaged magnetization across the thickness.

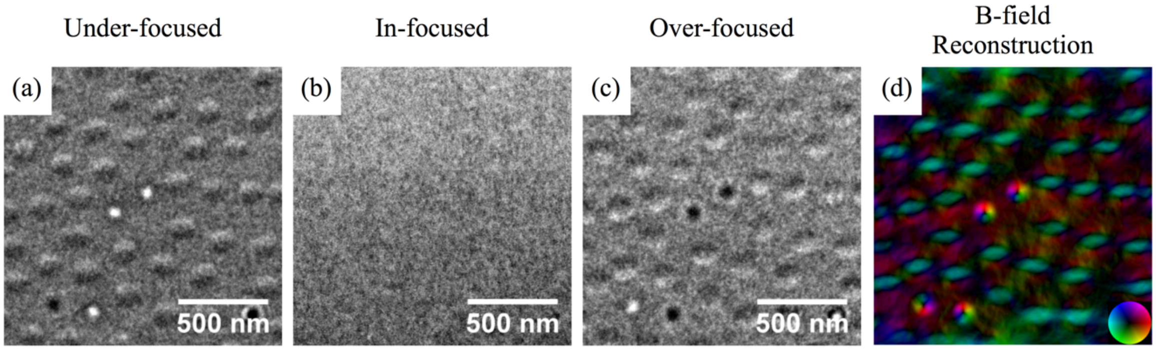

Figure 3.14 – Transport of intensity equation analysis. **(a-c)** Detail Lorentz TEM images captured at different focus positions at the same physical region of an Fe/Gd multilayer under the application of a perpendicular magnetic field at room temperature. **(d)** The color-map shows the in-plane magnetic induction field obtained from analyzing images **(a-c)** using TIE equation.

In some cases, the magnetic domains configurations are not easily identifiable. For example, closure domains are not easily discernable in a thin film because their symmetry at the top and bottom of the magnetic film cancel-out the Lorentz force exhibited by the electron (Fig. 3.13a). Similarly, a thin film that exhibits in-plane magnetic domains will likely not yield magnetic domain contrast given the stray field and magnetization will cancel out some or most of the Lorentz force acting on the electron (Fig. 3.13b). For the latter reasons, some magnetic information can be lost due to the transmission nature of the technique.

Images detailing the field and temperature dependence of Fe/Gd magnetic domains were recorded in Lorentz mode using an FEI Titan equipped with an image aberration corrector at the Center for Advanced Materials Characterization, University of Oregon. The magnetic contrast was obtained in Fresnel mode at three different image plane positions: under-focused, in-focus and over-focused. To facilitate the imaging, the Fe/Gd specimens are deposited on Si3N4 TEM grids (window: 30nm x 0.5mm x 0.5 mm with a 200μm thick frame) at the same time as other substrate for different characterizations.

One can further quantify the local magnetic induction integrated over the thickness of the specimen by means of analysis of under-focused, in-focused and over-focused images using the transport of intensity equation (TIE) in Fresnel-mode Lorentz TEM. The TIE relates the z-derivative of the image intensity $\boldsymbol{I}$ to the phase shift ϕ of the electron,

$$\nabla_{\perp}(\boldsymbol{I}\,\nabla_{\perp}\phi) = -\frac{2\pi}{\lambda}\frac{\partial \boldsymbol{I}}{\partial z}, \qquad \Delta\phi = -\frac{e}{\hbar}\iint \boldsymbol{B}\,d\boldsymbol{S} \tag{3.17}$$

where λ is the wavelength, $\hbar$ is the reduced Planck constant and $\boldsymbol{B}$ is the magnetic induction along the xy-plane [8]. Figure 3.14 shows the images at different focus and the resulting magnetic induction $\boldsymbol{B}$ color map obtained from TIE analysis. This technique provides a one-to-one relationship with the domain wall information in thin films. The under-focused or over-focused images in Fig. 3.14a, c can only provide information about the geometry of the magnetic domain but definite details about the vorticity cannot be deduced. Whereas, the magnetic induction map (Fig. 3.14d) reveals that most textures possess bound pairs of opposite helicity skyrmions where the domain walls wraps around both cylindrical domains continuously without changing its vorticity and allows to determine some cylindrical textures have a domain wall that continuously wraps around the texture.

3.3.2 Full-Field Transmission X-ray Microscopy

X-ray microscopy is a real-space imaging technique based on a materials absorption dependence of circularly polarized x-rays, e.g. x-ray magnetic circular dichroism (XMCD)

[9,10]. Similar to an optical microscope, the light is focused onto a specimen using a condenser lens while an objective lens focuses the light onto a detector. However, the light source for this microscopy technique are synchrotron produced x-ray beams.

Synchrotron x-rays are based on the principle that when electrons change their trajectory these emit energy [11]. If the electrons are accelerated near the speed of light, then the radiation emitted can be ultraviolet or x-ray beams. In order to produce high energy electrons, new synchrotron facilities utilize a linear accelerator to inject bunches of electrons at a velocity comparable to the speed of light into a booster synchrotron ring where these electrons are further accelerated using electric fields [12]. To maintain electrons in the circular path, magnets are used to bend and contain the electrons within the orbital trajectory. Afterwards, the high energy electrons are passed into a large storage ring where these continue to move near the speed of light. Since electrons are moved in straight trajectories, a series of bending magnets are used to deflect electrons from their path to continue circulating in the storage ring. In between bending magnets, periodic arrangements of dipole magnets are placed to generate an alternating static magnetic field which causes the electron beam to move sinusoidally. The latter results in an increase emission of synchrotron radiation as well as an increase of intensity. Depending on the oscillation of the electron beam, these magnets are called wiggler or undulator. At each bending magnet or the end of an undulator or wiggler magnet, a beamline is positioned to capture the energy radiation resulting from changing the trajectory of the electrons. Each beamline is designed to exploit the radiation using a unique experimental technique.

The Lawrence Berkeley National Lab, Advanced Light Source is one of the world's brightest sources of ultraviolet and soft x-ray light [12]. It is a 3rd generation synchrotron

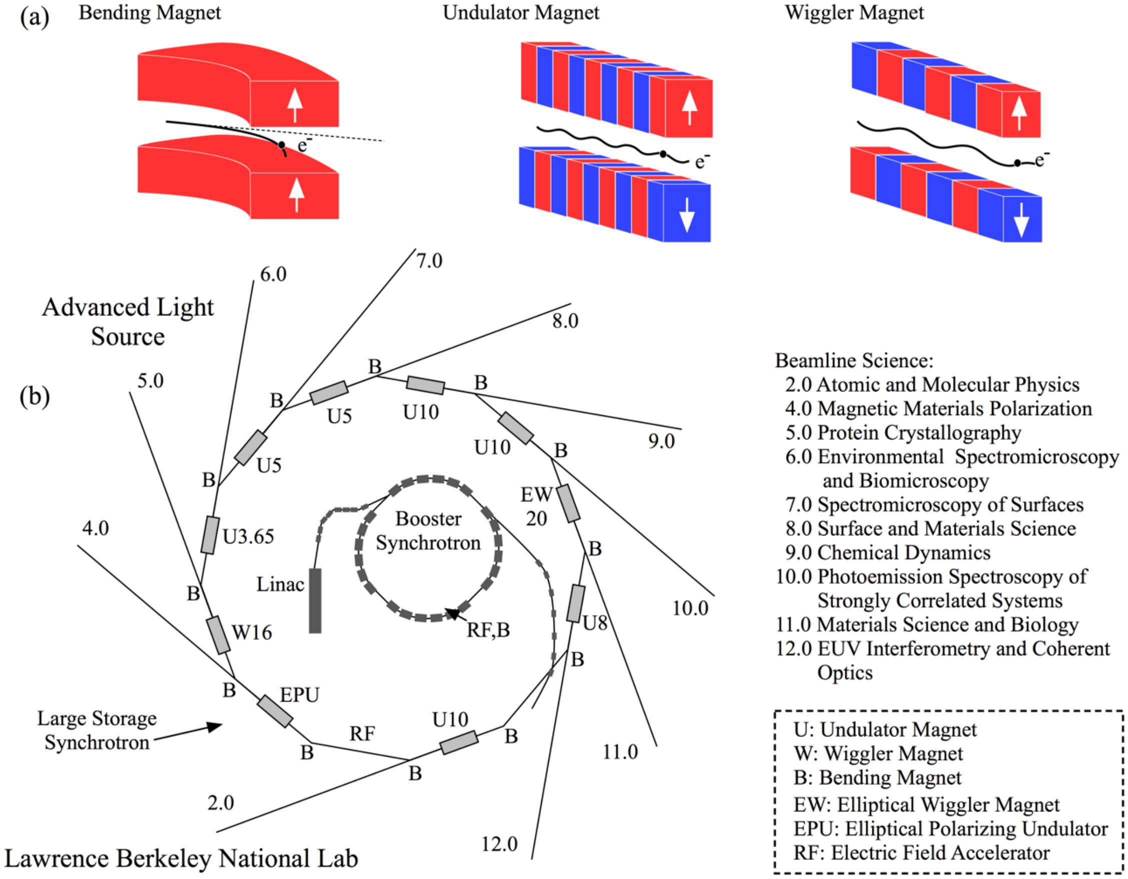

Figure 3.15 – LBNL ALS Synchrotron. (a) Shows the different magnets used at a synchrotron. A bend magnet is used to change the path of the electron to circulate around the storage ring. When the electron travels through a wiggler or oscillator magnet the electron will oscillate sinusoidally (larger/smaller periodicity results in broader/faster electron oscillations). **(b)** Details the layout of the Lawrence Berkeley National Lab, Advanced Light Source with emphasis on the magnets and the beamline end stations. A combination of bend, wiggler and undulator magnets are used to produce variations of energy radiation at different segments of the storage ring. Magnet types are based on the legend. The number next to the type of magnet refers to the period of the dipole magnets, e.g. U10 is an undulator magnet with 10cm period dipole magnets.

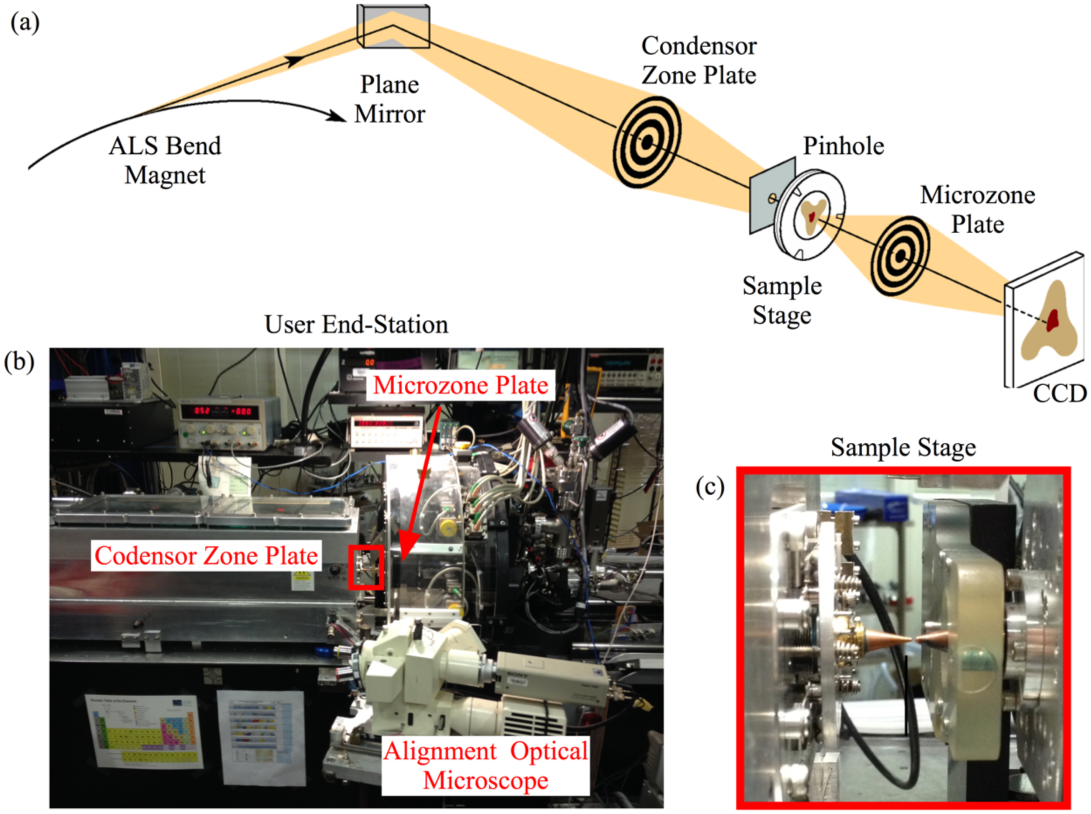

Figure 3.16 - XM1 microscope. (a) The schematic of ALS Beamline 6.1.2 is detailed from the bend magnet to end-station with emphasis on the Fresnel zone plate optics used to focus and collect the transmitted soft x-rays. **(b)** Shows an image of the end-station where the specimen is mounted between the condenser and the micro-zone Fresnel plates. The sample stage is enclosed by a red box. **(c)** An enlarged view of the sample stage in **(b)** is displayed. The sample is mounted between the two copper cones separating vacuum environments where the Fresnel zone plates are placed.

facility with electrons bunches spaced at 500 MHz intervals and possesses a beam intensity of ~1.9GeV. Figure 3.16b shows a schematic of the ALS synchrotron which details the storage ring and the various experimental techniques available.

Soft x-ray full-field transmission microscopy was performed at the Lawrence Berkeley National Lab, Advanced Light Source (ALS, Beamline 6.1.2 XM1) at room temperature. The XM1 microscope end-station offers a spatial resolution between 10 nm and 25 nm, elemental specificity with core level absorption energy in the range of 500eV to 1500eV, a field of view area of 10μm^2 and the potential to apply up to 2kOe in-plane magnetic field and 5kOe perpendicular magnetic field [9,10]. Figure 3.16a, b shows the schematic and a picture of the XM1 microscope at the ALS.

An x-ray microscope employs the use of diffraction plates with concentric gratings to focus light to and from a specimen, called zone plates, because glass lenses are not transparent at x-ray wavelengths. The gratings consist of alternating transparent (SiN) and opaque (Au) rings as shown in the insert of Figure 3.16b. When light is transmitted through the zone plate, these form constructive interference at the x-ray focal point as optical lenses.

To image magnetic domains at XM1, Figure 3.16, the x-ray illumination provided by the ALS bend magnet is projected onto the sample by means of condenser zone plate. To adjust the energy of the x-rays to specific core level absorption edges a pinhole is placed between the sample and the condenser plate, which acts as a linear monochromater. Adjusting the distance between the condenser zone plate and the pinhole allow one the ability to tune the illumination energy. Then the x-ray light transmitted through the sample is projected onto an x-ray sensitive CCD detector by means of a micro-zone plate.

3.3.3 Resonant Soft X-ray Scattering

Soft x-ray scattering is a reciprocal space imaging technique that yields quantitative information of the global properties of specimen. The information is encoded into scatter patterns of varying pixel intensity. Different information can be retrieved from the scatter pattern depending on whether the x-rays are coherent or incoherent. To address this, let us assume that each scattered x-ray has the form,

$$\psi = f(\boldsymbol{r})e^{i\boldsymbol{Q}\boldsymbol{r}} \tag{3.18}$$

where $f(\boldsymbol{r})$ is the scatter factor that contains charge and magnetic information, $\boldsymbol{Q} = \boldsymbol{k_i} - \boldsymbol{k_s}$ is a phase factor describing the momentum transfer between incident and scattered x-rays and $\boldsymbol{r}$ is the lattice site. If the illumination is incoherent, then the intensities of the scattered x-rays are summed,

$$I \propto \sum_n \left|f_n(\boldsymbol{r_n})e^{i\boldsymbol{Q}\boldsymbol{r_n}}\right|^2 \tag{3.19}$$

and as consequence the properties of the specimen are averaged over the illumination area. However, if the x-rays are coherent then the amplitudes of the scatter factors are summed,

$$I \propto \left|\sum_n f_n(\boldsymbol{r_n})e^{i\boldsymbol{Q}\boldsymbol{r_n}}\right|^2 \tag{3.20}$$

and the interference between the scattered x-rays results in a unique diffraction pattern, commonly known as speckle pattern. From this we see that coherent soft x-rays provide the means to map a specimen's complexity onto a scatter image that contains atomic, structural and magnetic information [13]. The technique is called resonant because one can tune the photon energy to a specific absorption edge of the atomic core electrons. In the case of magnetic materials, the contrast of the scatter image is enhanced as a consequence of magnetic x-ray circular magnetic dichroism [14,15].

Since we are interested in the magnetic moment of magnetic specimens, the intensity of the scatter pattern can be written as

$$I(q) \propto |f_m|^2 \propto \left|FT\left(\boldsymbol{M}(\boldsymbol{r})\right)\right|^2 \tag{3.21}$$

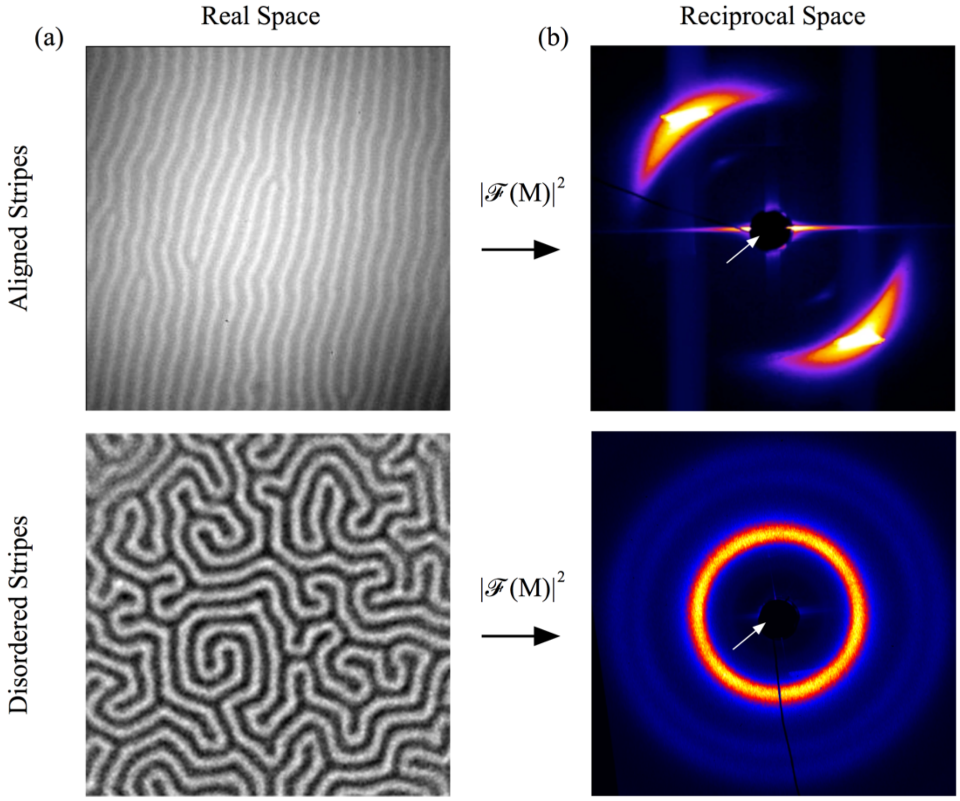

Figure 3.17 – Real and reciprocal space images. The domain morphology at zero-field of Fe/Gdx80 and Fe/Gdx120 captured at room temperature using **(a)** full-field transmission x-ray microscopy and **(b)** resonant soft x-ray scattering are illustrated. The inserted arrow in **(b)** show the beam-stop.

where $\boldsymbol{M}(\boldsymbol{r})$ is the magnetization of specimen. From Eq. 3.19, it follows that the phase information of the magnetization is lost for both coherent and incoherent scattered x-rays and the intensity represents the Fourier transform squared of the magnetization.

Soft x-ray scattering can be performed in two geometries: (i) in transmission, the magnetic scattering is proportional to the out-of-plane magnetization and is ideal for studying films with perpendicular magnetic anisotropy. (ii) Whereas in reflection mode, the magnetic scattering mixes information from all three magnetization components and

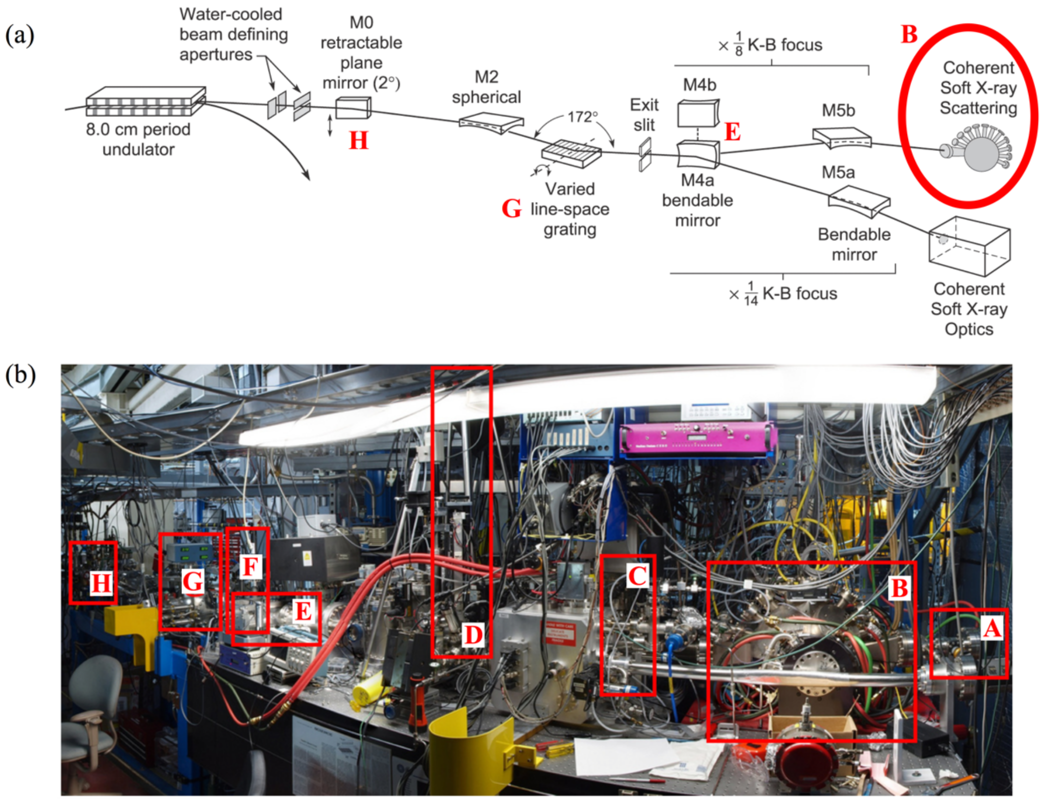

A: CCD Camera
B: Coherent soft x-ray scattering chamber
C: Vaccumm valve (protects the storage ring from being vented)
D: Beampipe to microscope above beamline for checking focus
E: M4 bendable magnet
F: Ti and Cu/Co/Fe/Ne filters for energy calibration
G: Varied Line-Space Grating Monochromator
D: M0 plane mirror

Figure 3.18 – Resonant soft x-ray scattering. (a) The schematic of ALS Beamline 12.0.2 is detailed from the 8cm period undulator magnet to the end-station where the measurements are performed. The schematic emphasizes the different mirrors used to maintain the coherence of the soft x-rays from the source to the sample. **(b)** Shows an image of the end-station where different components are identified.

for this reason is suitable for studying thick films with in-plane anisotropy [14]. Figure 3.17 shows the real and reciprocal space images of disordered perpendicular stripe domains and aligned stripe domains.

Resonant soft x-ray scattering (RSXS) was performed at Lawrence Berkeley National Lab, Advanced Light Source (Beamline 12.0.2) from room temperature to cryogen temperatures (300K – 80K). The end station allows for scattering measurements in reflection and transmission geometry. One can tune the core absorption energy between the range of 200eV to 1000eV and has a minimum exposure time for each scatter pattern of 1 second. The end-station is equipped with an octopolar magnet with a maximum field of 7KOe in every direction. The scattered x-rays are collected with of CCD-camera that is positioned in one of the multiple flanges to capture reflection or transmission x-rays [14]. Samples must be deposited on SiN membranes to enable x-rays to travel through the specimen in transmission geometry.

Figure 3.18 shows the schematic and image of beamline 12.0.2 that is optimized for coherent soft x-ray scattering experiments. The coherent x-ray radiation is a result of an 8cm period undulator magnet. To obtain a fully coherent beam, a pinhole is introduced in front of the sample that blocks most of the x-ray illumination with the exception of narrow region around the center of the beam which is highly coherent. For our RSXS measurements, we did not introduce a pinhole because we were solely interested in studying the magnetic domain distributions as a function of magnetic field and temperature. To protect the detector from direct beam exposure, a beam-stop is placed at the center of the membrane window. The beam-stop also increases visibility of the lower intensity scattered x-rays compared to the direct beam intensity.

3.3.4 Magnetic Force Microscopy

Magnetic force microscopy (MFM) is a scanning probe technique that displaces a physical probe over the surface of a magnetic specimen to indirectly obtain information about the domain morphology. This technique exploits the stray field arising from a magnetic specimen to detect the surface magnetization (Fig. 3.19). The physical probe consists of a sharp tip (~50nm radius) that is coated with a magnetic material and is placed at the end of a cantilever (Fig. 3.20). The tip is then positioned relatively close to the magnetic surface to enable the tip to interact with the stray field which exerts a force onto the tip. To quantify the force on the tip, the cantilever is driven at its resonant frequency and its oscillation is described in terms of Hook's law,

$$F = -kz, \qquad f_r = \frac{1}{2\pi}\sqrt{\frac{k}{m}} \tag{3.22}$$

where k is the spring constant and z is the displacement of the cantilever tip normal to the surface, f_r is the resonant frequency of the cantilever and m is the effective mass of the cantilever. To drive the cantilever, light is shined onto the backside of the tip and then the reflected light is collected by a detector. A feedback loop provides the ability to maintain a fixed excitation on the cantilever, while keeping a constant oscillation in amplitude or frequency. Phase-shifts in either of the latter provide information about the field gradients acting on the tip.

Magnetic force microscopy can be performed in two modes of operations: In constant height mode the tip is scanned at a fixed position above the surface. An image is constructed by collecting the individual line profiles over a specific region of the sample. Usually this mode is only appropriate for specimens with few debris or relatively low surface roughness because the latter can introduce artifacts into the collected signal. In dual-pass mode, the tip is scanned over the surface of the sample in contact-mode to first obtain the topography along the path of the tip. Then the tip is raised to a specified height

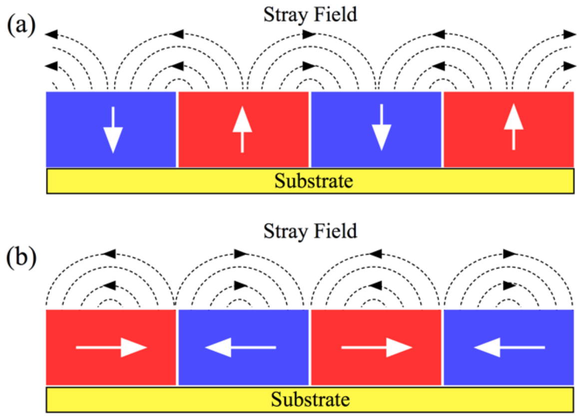

Figure 3.19 – Dipole fields from film surface. The stray field resulting from multi-domain morphologies with **(a)** perpendicular magnetic domains and **(b)** in-plane magnetic domains is shown.

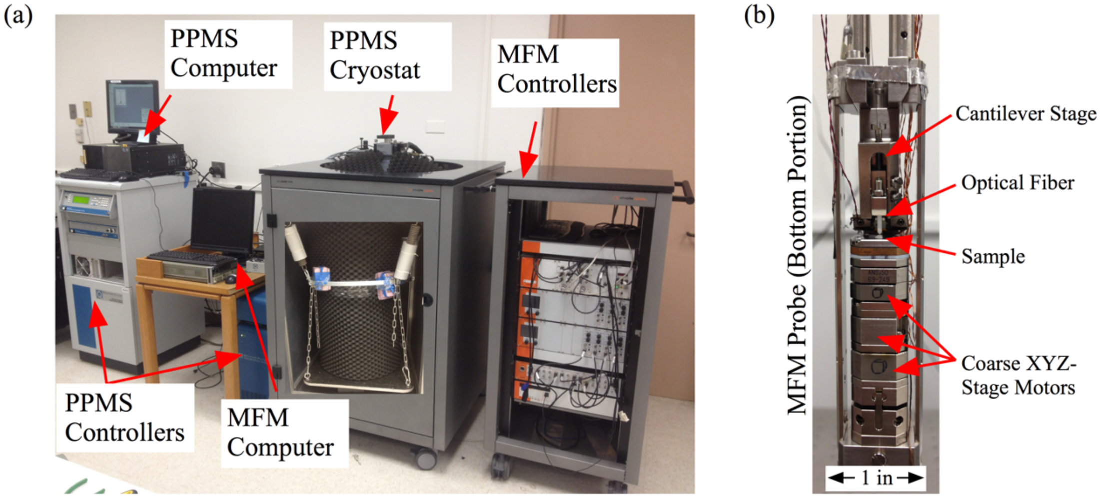

Figure 3.20 – Attocube MFM probe. Shows the experimental devices used to perform magnetic force microscopy on a PPMS cryostat. To reduce vibrations, the PPMS is suspended on springs inside the damping box. **(b)** The components of the MFM probe are detailed. The sample is positioned over the coarse XYZ-stage controllers and the cantilever stage lies over the sample.

and the tip rescans the same path along the recorded surface tomography at a constant elevation. The latter mode removes artifacts from the magnetic topography and provides a closer representation of the surface magnetic domain morphology.

Although this technique is considered relatively non-invasive, for soft-magnetic specimens the magnetic tip can interact with the domains and even displace the magnetic domains within the scanning region. For this reason, probe tips are coated with different kinds of magnetic materials which possess different field coercivity. This facilitates variability in stray field sensitivity and impact on the domain states. Typically, several scans need to be collected at different elevation positions to ensure the magnetic tip influence on the domains is minimal.

Low temperature magnetic force microscopy was performed using an Attocube attoMFM-I in combination with a Quantum Design Physical Property Measurement System cryostat with a 9T superconducting magnet. The MFM is mounted on a probe (Fig. 3.20) that is inserted into the QD PPMS for temperature and field measurements. The MFM is located on the bottom portion of the probe which possess an xyz-stage controller, a piezo-crystal stage and a cantilever holder (Fig. 3.20). The xyz stage facilitates coarse and fine adjustments to position the sample underneath the cantilever where the MFM tip is positioned. An optical fiber transmits the laser light (650um, 3uW) onto the cantilever and then also collect the reflected light from the cantilever into a detector.

3.4 Fabrication Techniques

Most studies presented in this work were conducted on continuous thin films, but in order to study transport properties and current induced dynamics we fabricated wires by means photolithography. The technique uses a very bright light source to embed a specific geometrical pattern defined on a glass mask onto a light sensitive material that is placed over a substrate. It is a simple fabrication process which allows the development of geometrical features with 1μm resolution. In this work, wires with eight-contact pads were primarily fabricated on Si substrate with a thermal oxide layer and SiN membranes.

The following steps detail the fabrication process:

a. Surface cleaning: Substrate that is not very clean undergoes several rinses to remove debris from the surface of the substrate prior to photolitographic fabrication, which consists in: soaking the substrate in acetone for 5 minutes with ultrasonic agitation and then transferring the substrate into a bath of isopropyl alcohol for 5 minutes with ultrasonic agitation. Afterwards, the substrate is rinsed with deionized water and the excess water is blown off with N_2 gun.

b. Spin coating the photoresist: The substrate is placed inside a spin-coater and it is secured to the spinner chuck under vacuum seal. The negative photoresist (Futurrex NR9-1500) is applied over the substrate, avoiding trapping air bubbles, and it is then spin-coated at 4500 rpm for 1 minute. This process results in a uniform coating with thickness ~1μm.

c. Soft baking the photoresist: After the substrate has been spin coated with the photoresist, it is baked at 150°C for 1 minute over a hot-plate to densify the photoresist.

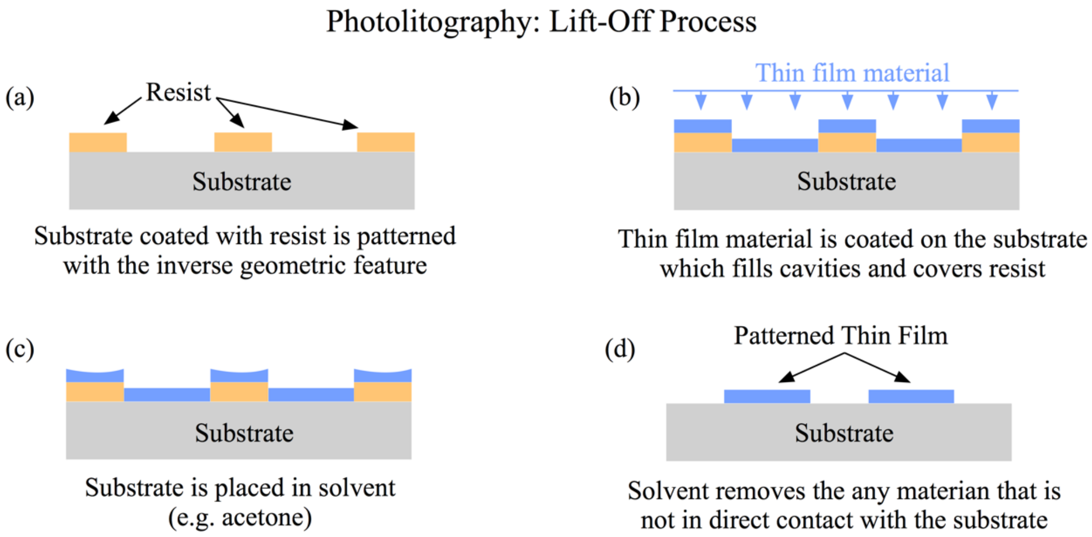

Figure 3.21 –Lift-off process. (a-d) Show the four steps to finalize the development of photo-lithographically patterned films by means of lift off.

d. Mask alignment: The substrate is then transferred to a mask-aligner (Karl Suss MA6), where a glass mask with the desired geometrical feature is positioned over the substrate.

e. Exposure: The photoresist is then exposed with UV light source for 10 seconds.

f. Post-baking: After exposure, the substrate is post-baked at 100°C for 1 minute to hardened the developed photoresist.

g. Development: The substrate is then transferred into a beaker with resist developer (Futurrex RD6) for 10 seconds to remove photoresist from the unexposed areas.

h. Post-process cleaning: To stop the developer from decomposing the photoresist, the substrate is washed with deionized water and the excess water is blown off with an air gun.

Afterwards, a thin film specimen is sputter deposited onto the substrate with the patterned devices which coats areas with and without photoresist (Fig. 3.21a, b). Then the sputtered sample is placed inside an acetone bath which removes the material where the photoresist was present (Fig. 3.21c, d). In the end, the inverse geometrical feature that was originally embedded to the substrate remains.

3.5 References

[1] *Quantum Design - Vibrating sample magnetometer option user manual*, p. 1-2.

[2] J. M. Florczak and E. Dan Dahlberg, *Detecting two magnetization components by the magneto-optical Kerr effect*. J. Appl. Phys. 67, 7520 (1990).

[3] C. Daboo, J. A. C. Bland, R. J. Hicken, A. J. R. Ives and M. J. Baird, *Vectorial magnetometry with the magneto-optic Kerr effect applied to Co/Cu/Co trilayer strucuture.* Phys. Rev. B. **47**, 11852 (1993).

[4] S. S. Kalarickal, P. Krivosik, M. Wu, C. E. Patton, M. L. Schneider, P. Kabos, T. J. Silva, J. Nibarger, *Ferromagnetic resonance linewidth in metallic thin films: Comparison of measurement methods*, J. Appl. Phys. **99**, 093909 (2006).

[5] W. Barry, "*A broad-band automated stripline technique for the simultaneous measurement of complex permittivity and permeability*", *IEEE Trans. Microw. Theory Tech.* **34**, No. 1, 80-84, (1986).

[6] T. R. Mcguire and R. I. Potter. *Anisotropic magnetoresistance in ferromagnetic 3d alloys.* IEEE Trans. Magn. 11, 1018-1038 (1975).

[7] H. Hapster and H. P. Oepen, *Magnetic microscopy of nanostructures* (Springer, Berlin, 2005), p. 67-85.

[8] M. R. Teague, *Deterministic phase retrieval: a Green's function solution*, J. Opt. Soc. Am. **73**, 1434. (1983).

[9] G. Denbeaux, et. al., *A full field transmission X-ray microscope as a tool for high-resolution magnetic imaging*, IEEE Trans. Magn. Mag. **37**, No. 4 (2001).

[10] A. L. Pearson, et. al., *XM-1, the high resolution soft x-ray microscope at the Advanced Light Source*, Proc. SPIE 4146, Soft X-Ray and EUV Imaging Systems, 54 (November 8, 2000).

[11] F. R. Elder, A. M. Gurewitsch, R. V. Langmuir and H. C. Pollock, *Radiation from electrons in a synchrotron*, Phys. Rev. **71**, 829 (1947).

[12] D. Robin for the Superbend team, *Superbend upgrade at the advanced light source, Proceedings of the 2003 Particle Accelerator Conference* (2003).

[13] S. Kevan, *Coherent soft x-ray scattering or studying nanoscale materials*, NSLS II Workshop.

[14] K. Chesnel, J. J. Turner, M. Pfeifer and S. D. Kevan, *Probing complex materials with coherent soft x-rays*. App. Phys. A **92**, 431-437 (2008).

[15] F. van der Veen and F. Pfeiffer*, Coherent x-ray scattering*. J. Phys. Condens. Matter **16**, 5003-5030 (2004).

[16] B. Bhushan, *Handbook of Nanotechnology* (Springer, Berlin, 2010) p. 579-607.

[17] C. Schonenberger and S. F. Alvarado, *Understating magnetic force microscopy*. Z. Phys. B. 80, 373-383 (1990).

Chapter 4

Magnetic Properties of Dipole Skyrmions

4.1 Introduction

Skyrmions are topologically non-trivial cylindrical-like magnetic domains that exhibit novel physics and potential applications to non-volatile memory [1-6]. As described earlier, these textures exist in an array of materials from bulk magnets [7-10] to thin films [11-18] and have been shown to be stable under several physical mechanisms [18-22]. The most heavily studied mechanism to stabilize skyrmions is the Dzyaloshinskii-Moriya interaction (DMI) arising in non-centrosymmetric magnetic materials or thin films with asymmetric heavy metal interface [7-14]. However, topologically similar spin structures can be stabilized by the competition of long-range dipolar energy in a thin film geometry and domain wall energy [16-18], a mechanism by which magnetic stripes and bubbles form [23-39]. Commonly a chiral magnetic bubble is termed a dipole stabilized skyrmion given the resemblance to a Bloch-type DMI interaction skyrmion [2,17,18]. Given these chiral bubbles form under the application of a perpendicular magnetic field they are said to be extrinsically stable [5]. Both these class of topologically protected magnetic features are interesting and there are numerous examples of materials showing them, however, there is a limited understanding of the basic magnetic energetics required to favor their formation. These chiral bubbles or dipole-stabilized skyrmions present a test-bed to explore how the balance of ferromagnetic exchange, anisotropy and dipolar energy results in cylindrical-like domains that are topologically non-trivial.

In this work we explore the formation of dipole-stabilized skyrmions and skyrmion lattices in amorphous Fe/Gd multilayers, with the focus on developing predictive properties that can result in the stabilization of chiral textures. Through thickness, alloy composition and temperature dependent studies of various Fe/Gd films, we find we can control the skyrmion lattice, in temperature and applied magnetic fields, by tuning the material properties of the multilayer structure. This tunability allows us to investigate the skyrmion sensitivity to material properties to manifest ordered and disordered skyrmions. By comparing experimental findings with micromagnetic modeling we show the skyrmion-lattice phase appears for a parameter space with a combination of relatively low perpendicular magnetic anisotropy (~2-4x10^5 ergs/cm^3), low magnetic moment (~350-500 emu/cm^3), low exchange interaction (~5x10^{-7} ergs/cm), and thick films (>40 nm). Our results provide a guideline of magnetic properties required to stabilize these spin textures in thin-film ferromagnets and ferrimagnets.

The Fe/Gd films we have studied consist of multilayer deposited structures of Fe and Gd thin films (each layer <0.4nm) which are antiferromagnetic coupled forming a ferrimagnet. By appropriately choosing the thickness of the layers and the deposition conditions the films develop PMA [38-39]. In general, favorable conditions for the observation of perpendicular magnetic domains requires the uniaxial anisotropy K_U be greater than the shape anisotropy $2\pi M_S^2$ where the ratio of these parameters is defined as a material's Q-factor [24]. For our films, the Q-ratio are less than 1 but by increasing the number of bilayer repetitions (*i.e.* the total film thickness) results in a transition from in-plane magnetization to the formation of perpendicular magnetic domains [40-44]. We will first show Lorentz transmission electron microscopy (TEM), resonant soft x-ray scattering and full-field transmission X-ray microscopy to confirm the presence of skyrmions and skyrmion lattices in our films and determine the sensitivity of the skyrmion formation to the temperature, applied magnetic field range and film thickness. We will then quantify the materials parameters of our films and compare the experimental results to micromagnetic simulations.

4.2 Experimental details

The Fe/Gd specimens are sputter deposited at room temperature in a UHV environment under a 3mTorr Argon environment. To grow the film structures, we alternatively deposit Fe and Gd layers of a specific thickness, and continue process until achieving multilayer with the desired number of layers. Films have a seed/capping layer of Ta (5nm) to protect the films from corrosion. Samples are deposited on a range of different substrate for magnetic and imaging characterization, including 50nm and 200nm SiN membranes and Si substrate with a native oxide layer.

The field and temperature dependence of the magnetic domain morphology is imaged using a variety of techniques, which include: (*i*) LTEM, (*ii*) soft x-ray scattering (SXS) at the Gd M_5 (1198eV) absorption edge and Fe L_3 (708eV) absorption edge at Beam-line 12.0.2 Advanced Light Source, Berkeley National Lab and (*iii*) full-field transmission X-ray microscopy along the Fe L_3 (708eV) absorption edge performed at Beam-line 6.2 Advanced Light Source, Berkeley National Lab.

4.3 Skyrmion lattice formation at room temperature

Figure 4.1 shows the field dependence of the magnetic domain morphology of a [Fe (0.34 nm)/Gd (0.4 nm)]x80 multilayer (total thickness 53.6nm, see Chapter 4.8) imaged by means of Lorentz TEM at room temperature. The under-focused images are obtained as a magnetic field perpendicular to the sample is swept from zero towards magnetic saturation. Each field image is from the same region of the sample but not the same specific area of the sample as the image position shift with applied magnetic field. At zero field the film exhibits stripe domains that have a periodicity of ~124 nm (Fig. 4.1a) and random in-plane order. The images reveal the in-plane magnetization orientation averaged over the thickness of the magnetic domains through variations of darkness/brightness intensity, and domain walls are evidenced by strong and sharp dark/bright contrast changes. Analysis of over/under-focused Lorentz TEM images using the transport-of-intensity equation [45, 46] allows us to determine the projected in-plane magnetic induction, shown as a color map in Fig. 4.1b. Here, the color indicates the direction of the magnetic induction with respect to the color-wheel insert; in a similar fashion, the color intensity details the magnitude of the magnetic induction. The images show that the stripe domains are separated by Bloch walls (Fig. 4.1b) where the in-plane moment of the walls is parallel to the stripes. This arrangement is more clearly observable in the enlarged image (Fig. 4.1c) detailing the enclosed region of Figs. 4.1a and 4.1b, where both the color and vector maps detail the direction of the Bloch wall. Since the films are relatively thick and no DMI is anticipated a Bloch-like domain structure is expected. As will be discussed below there are likely closure domains (*e.g.* Néel caps) at the top and bottom of the films [47]. Evidence of closure domains will not be visible in these images since the orientation of these domains at the top and bottom of the films are opposite in direction and will average to zero in Lorentz TEM images.

As a magnetic field is applied, perpendicular to the film (Figs. 4.1d and 4.1e), the stripes with magnetization parallel to the field grow at the expense of domains opposite to the field. We observe that the stripe domains whose magnetization is opposite to the field begin to collapse into cylindrical domains (Figs. 4.1d and 4.1e). Since the Bloch-line continuously wraps around the cylindrical domain it is defined as a skyrmion with winding number $S = 1$ [2,3]. If the Bloch-line wraps continuously in a clockwise fashion then it has helicity $\gamma = -\pi/2$, whereas if the Bloch-line wraps counter-clockwise direction it has helicity $\gamma = +\pi/2$ [2]. At $H_z = 1450$ Oe, the skyrmions have a diameter of ~71nm and their size does not vary significantly from initial formation to annihilation. The enclosed/enlarged region, detailed by red boxes in Figs. 4.1d and 4.1e, shows the extremities of a stripe domain collapsing into a skyrmion (Fig. 4.1f), as well as, as the color/vector map representation of the magnetic textures enclosed. At this magnetic field strength, the domain morphology consists of a combination of disordered stripe domains and skyrmions (Figs. 4.1c and 4.1d).

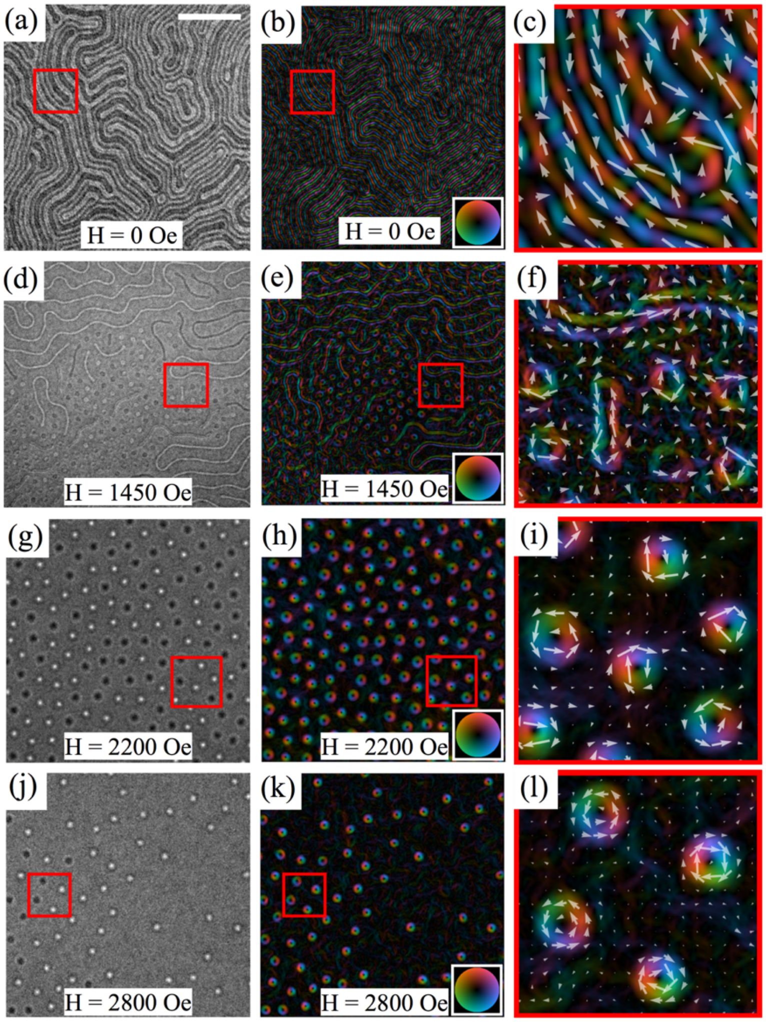

Figure 4.1 – Real space imaging of the field-dependent magnetic domain morphology of [Fe (0.34 nm)/Gd (0.4 nm)]x80. Under-focused Lorentz TEM images (first column) measured at room temperature and their corresponding magnetic induction color maps (second column) are detailed. The images are captured as a perpendicular magnetic field is applied from zero-field to magnetic saturation. Four different magnetic states are observed as the field is swept, including: disordered stripe domains (**a, b**), stripe-to-skyrmion transition (**d, e**), skyrmion lattice (**g, h**) and disordered skyrmions (**j, k**). Enclosed regions in the first two columns are enlarged to detail the in-plane magnetic domain configuration using both color and vector magnetic induction maps in the third column **(c, f, i)**. The scale bar in **a** corresponds to 1μm.

As the magnetic field is further increased, the entire film fills with dipole skyrmions with an equal population of the two possible helicities (Figs. 4.1g and 4.1h). The two different helicities ($S = 1$, $\gamma = \pm\pi/2$) appear as dark and light cylindrical textures in Fig. 4.1g and they arrange into a weakly-ordered hexagonal lattice (Figs. 4.1g and 4.1h). This skyrmion lattice is stable for a wide range of magnetic fields spanning from 1700 to 2400 Oe. By increasing the magnetic field further, the skyrmion lattice dissociates into a disordered isolated skyrmion state where these textures begin to collapse as the film reaches magnetic saturation (Figs. 4.1j and 4.1k).

4.4 Temperature dependence of the skyrmion phase

Using a combination of real-space imaging and reciprocal-space scattering techniques we explored the dependence on temperature and applied magnetic fields that result in the formation of the skyrmion phase for two Fe-Gd compositions. From scattering patterns obtained by means of resonant soft x-ray scattering, see Chapter 4.5, we identified four regions emphasizing long-range ordered magnetic states including: (*i*) disordered stripe domains, (*ii*) a stripe-to-skyrmion transition, (*iii*) a skyrmion lattice and (*iv*) uniform magnetization. Then using images obtained from LTEM and transmission soft x-ray microscopy we supplemented our findings in the magnetic phase map. From real-space images, we identified an additional region detailing (*v*) disordered skyrmions that occurs after the skyrmion lattice dissociates. Since disordered skyrmions do not have any long-range order, this region is not easily determined in scattering experiments.

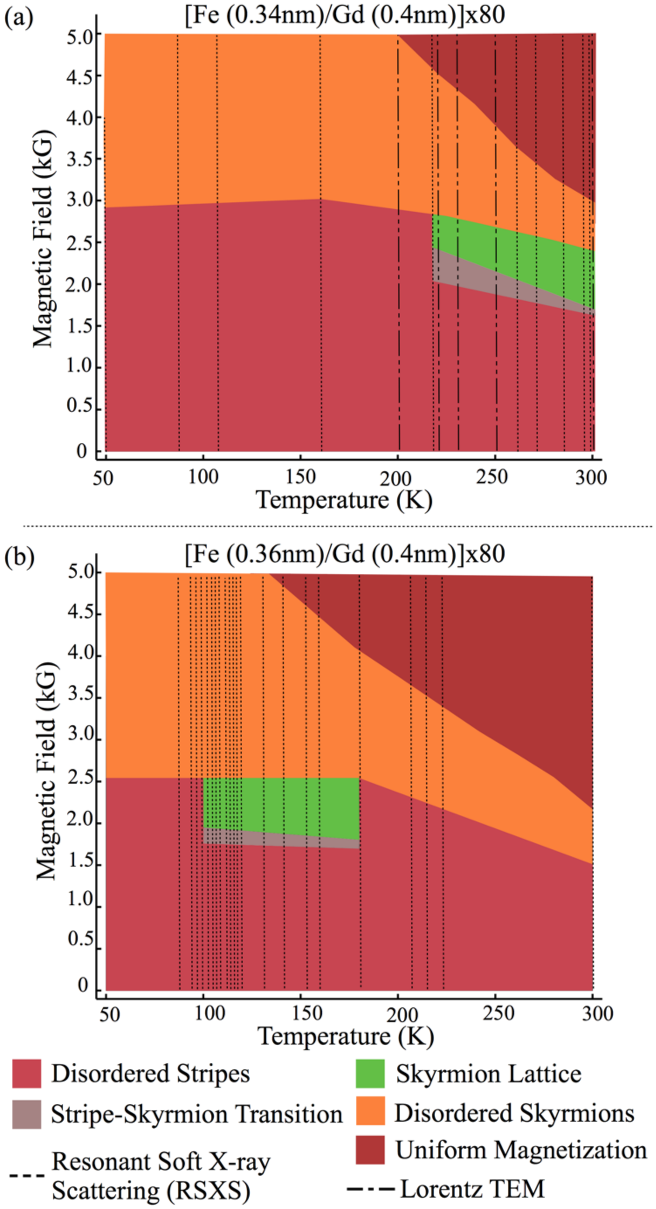

Figure 4.2 – Magnetic field and temperature dependence of the skyrmion phase. The magnetic phase diagram for two Fe/Gd film structures are shown: **(a)** [Fe (0.34 nm)/Gd (0.4 nm)]x80 exhibits a broad skyrmion phase around room temperature, and **(b)** [Fe (0.36 nm)/Gd (0.4 nm)]x80 shows a similar skyrmion phase that is shifted to lower temperatures. These magnetic phase maps are constructed using data from four different imaging techniques: resonant soft X-ray scattering, LTEM and transmission X-ray microscopy (at room temperature only). The marker-lines detail the temperature and imaging technique used to scan the domain morphology.

Figure 4.2 summarizes the various magnetic domain configurations observed when an applied field, perpendicular to the film applied from zero-field to magnetic saturation at detailed temperatures from 300K to 50K. We find that the [Fe (0.34 nm) /Gd (0.4nm)]x80 multilayer exhibits a similar domain morphology, as previously described with LTEM, with a skyrmion lattice that extends from room temperature to 220K for a wide range of applied magnetic fields (Fig. 4.2a). At temperatures where no skyrmion phase exists, the Fe/Gd film primarily exhibits disordered stripe domains. In the case we modify the Fe-content of the Fe/Gd structure to [Fe (0.36nm) /Gd (0.4nm)]x80, we find a similar broad skyrmion phase that is shifted to lower temperatures, spanning a temperature window from 180K to 100K (Fig. 4.2b). Here, it is evident that the formation of a skyrmion phase is sensitive to the Fe/Gd composition and is tunable to a temperature range of interest.

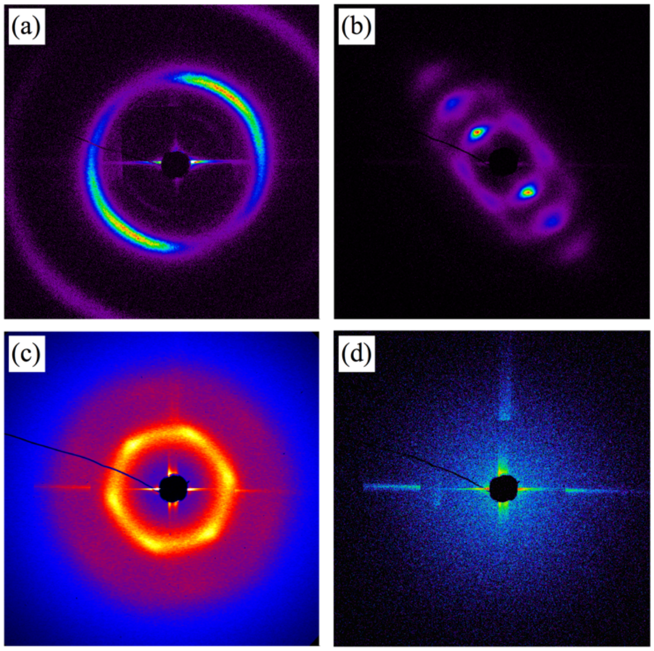

Figure 4.3 – Reciprocal space imaging of the field-dependent magnetic domain morphology of [Fe (0.34 nm)/Gd (0.4 nm)]x80. The scatter images obtained at room temperature detail the four magnetic phases observable using this technique: **(a)** disordered stripe domains, **(b)** coexisting stripes and skyrmions, **(c)** skyrmion lattice and **(d)** uniform magnetization. **(a)** The diffraction image is obtained along the Fe L_3 (708eV) absorption edge at zero-field at 85K. **(b, c)** These diffraction images are both obtained at room temperature along the Gd M_5 (1180eV) absorption edge at **(b)** $H_z = 1500$ Oe and **(c)** $H_z = 1900$ Oe. **(d)** The saturated state is obtained along the Fe L_3 (708eV) absorption edge at $H_z= 5000$ Oe at room temperature.

4.5 Resonant soft x-ray scattering

Figure 4.3 shows diffraction images exemplifying the different magnetic phases that are observable in [Fe (0.34nm) / Gd (0.4nm)]x80 along the Gd M_5 (1198eV) absorption edge and Fe L_3 (708eV) absorption edge. The disordered stripe domains are characterized by a ring-like scatter pattern (Fig. 4.3a) which agrees with our observation of disordered domains in LTEM and full-field transmission X-ray microscopy. Figure 4.3b shows the typical diffraction image obtained from the coexistence of stripes and skyrmions which depicts evidence of 6 Bragg peaks where two peaks exhibit higher intensity than the other four peaks. The skyrmion phase is depicted by a six-fold scatter pattern where the Bragg peaks possess near equal intensity indicating the presence of a hexagonal lattice of cylindrical-like magnetic features (Fig. 4.3c). Last, the uniform magnetization domain is depicted by a flat diffraction image, where there is no evidence of magnetic contrast (Fig. 4.3d).

4.6 Thickness dependence of the skyrmion phase

To further explore the formation of a skyrmion lattice at room temperature, we varied the number of Fe/Gd bilayer repetitions in the multilayer to investigate the role of the thin film magnetostatic energy on the skyrmion phase. The multilayers studied consisted of [Fe (0.34nm)/ Gd(0.41nm)]$_{xN}$ where N = 40, 80 and 120 repetitions where only the latter two film structures exhibited evidence of perpendicular magnetized stripe-like domains in their magnetic hysteresis loops (Fig. 4.4); whereas [Fe (0.34nm)/ Gd(0.41nm)]$_{x40}$ appears consistent with in-plane magnetic domains. This suggests that as the number of bilayers is increased, we gain magnetostatic energy to form perpendicular magnetic domains. Similar observations of a thickness driven spin reorientation of the magnetization, from in-plane to perpendicular, with increasing thickness have has been reported for numerous systems including hcp(0001) Co films [41-42].

When examining the field-dependence of the domain morphology by means of transmission soft x-ray microscopy measured at the Fe L_3 (708eV) absorption edge we verified that N = 40 film does not show any perpendicular magnetic domains while the N = 80 and N = 120 repeat films exhibited both stripe and skyrmion magnetic domain textures consistent with Fig. 4.1. The [Fe (0.34nm)/ Gd(0.41nm)]$_{x80}$ film exhibits stripe domains at zero applied field where the contrast is sensitive to the out-of-plane magnetization (unlike LTEM which is sensitive to the in-plane magnetization) (Fig. 4.4a). Here domains with magnetization parallel/anti-parallel to the perpendicular direction appear as dark/white textures. The presence of a small remanent in-plane magnetic field in the measurement causes the stripe domains to align in the direction of this field. With a modest out-of-plane field (H_z = 500, 625 Oe), we observe the stripes begin to pinch into cylindrical textures that occupy the same physical space of the original stripe (Fig. 4.4b-c). At this field there is a near equal population of stripes and aligned cylindrical domains. When the field is further increased (H_z = 750 Oe), we find all the stripes have pinched into aligned cylindrical textures that do not arrange into a close packing lattice (Fig. 4.4d). As the field is further increased, the cylindrical domains dissipate (Fig. 4.4d) and we are left with the cylindrical textures that first formed (Fig. 4.4b-c). This suggests that we observe two different magnetic domains as a consequence of the in-plane field. In one case, the Bloch-line of most stripes aligns in the direction of the in-plane field which results in the formation of magnetic bubbles (zero-chirality) when a perpendicular field is applied as described in Ref. 16; whereas, stripes with random Bloch-line arrangement result in skyrmions (chiral textures) as we have previously shown. Specifically, we have shown a skyrmion molecule [16] is made up of a bound pair of opposite helicity skyrmions which can also be stabilized in Fe/Gd films as a result of applying a fixed in-plane field and then applying a perpendicular magnetic field.

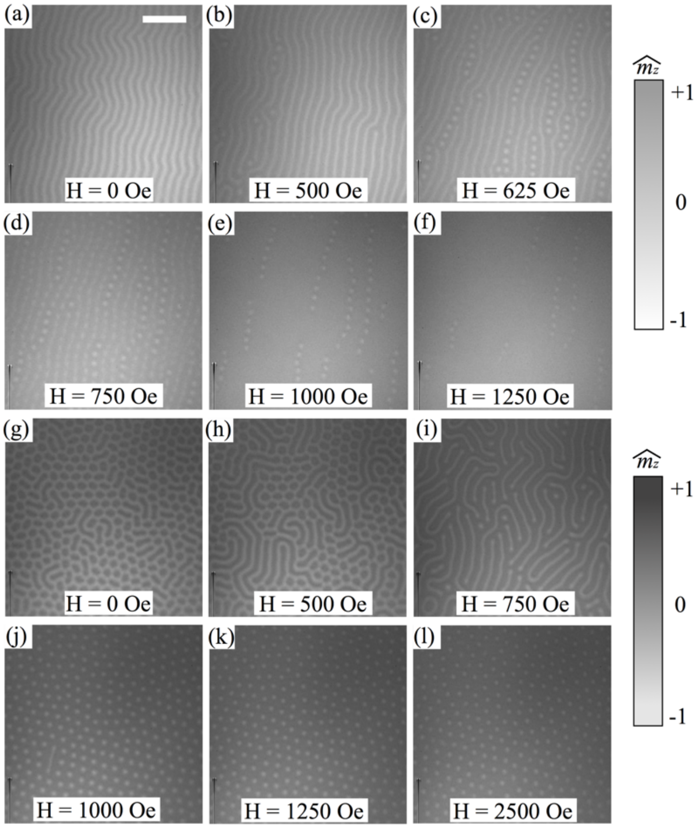

Figure 4.4 – Film thickness dependence of [Fe (0.34 nm)/Gd (0.41nm)]xN. The domain morphology, obtained by X-ray microscopy, for Fe/Gd multilayers with different bilayer repetitions are detailed, as a perpendicular magnetic field is applied from zero-field to magnetic saturation. **(a-f)** [Fe (0.34nm)/ Gd(0.41nm)]$_{x80}$ exhibits stripe domains at zero-field **(a)** that pinch off into skyrmions as the magnetic field is increased **(b-c)**. Above $H_z =$ 750Oe the cylindrical textures begin to collapse in aligned clusters **(e-f)** until no skyrmions can be observed in the field of view. **(g-l)** [Fe (0.34nm)/ Gd(0.41nm)]$_{x120}$ exhibits disordered stripe domains at zero field **(g)** that collapse begins to collapse into skyrmions as the magnetic field is increased **(h)**. These skyrmions arrange into closed-pack hexagonal lattice from $H_z =$ 800 Oe to 2500 Oe **(j-l)**. The scale bar in **a** corresponds to 1μm.

The thickest film studied, [Fe (0.34nm)/Gd(0.41nm)]$_{x120}$, showed disordered stripe domains (white domains) and dumbbell domains (dark domains) at zero-field. Here the remanent in-plane field is insufficient to cause the stripes to order, as observed previously.

When a perpendicular field is applied, the dumbbell domains begin to merge to form disordered stripes (Fig. 4.4h) and by H_z =750 Oe the stripes with magnetization opposite to the field begin to collapse into skyrmions (Fig. 4.4i). By slightly increasing the field again, all the stripes have collapsed into skyrmions and these have arranged into a weakly coupled hexagonal lattice which spans from H_z= 800 Oe to 2500 Oe (Fig. 4.4j-l). We find the skyrmions have a diameter of ~70nm and that the size does not vary significantly from their initial formation to annihilation. The variation of film thickness, clearly demonstrates that skyrmions, like bubbles, require a specific ratio of magnetic properties ad film thickness for these magnetic textures to become favorable [24,26].

4.7 Characterization of temperature dependent magnetic hysteresis and ferromagnetic resonance frequency

Inspection of the magnetic hysteresis of [Fe (0.34 nm)/Gd (0.4 nm)]x80 and [Fe (0.36 nm)/Gd (0.4 nm)]x80 reveal the loops are characteristic of a film exhibiting perpendicular magnetized stripe-like magnetic domain structure at room temperature [23,25,26,35] (Fig. 4.5a, b). This agrees with our experimental observation of disordered stripe domains at zero-field. A text-book example of a stripe-domain hysteresis loop occurs in [Fe (0.36 nm)/Gd (0.4 nm)]x80 at room temperature (Fig. 4.5a) which depicts a small hysteresis around the saturation field. This hysteresis is associated with the mechanism in which stripe domains form and collapse from cylindrical domains.

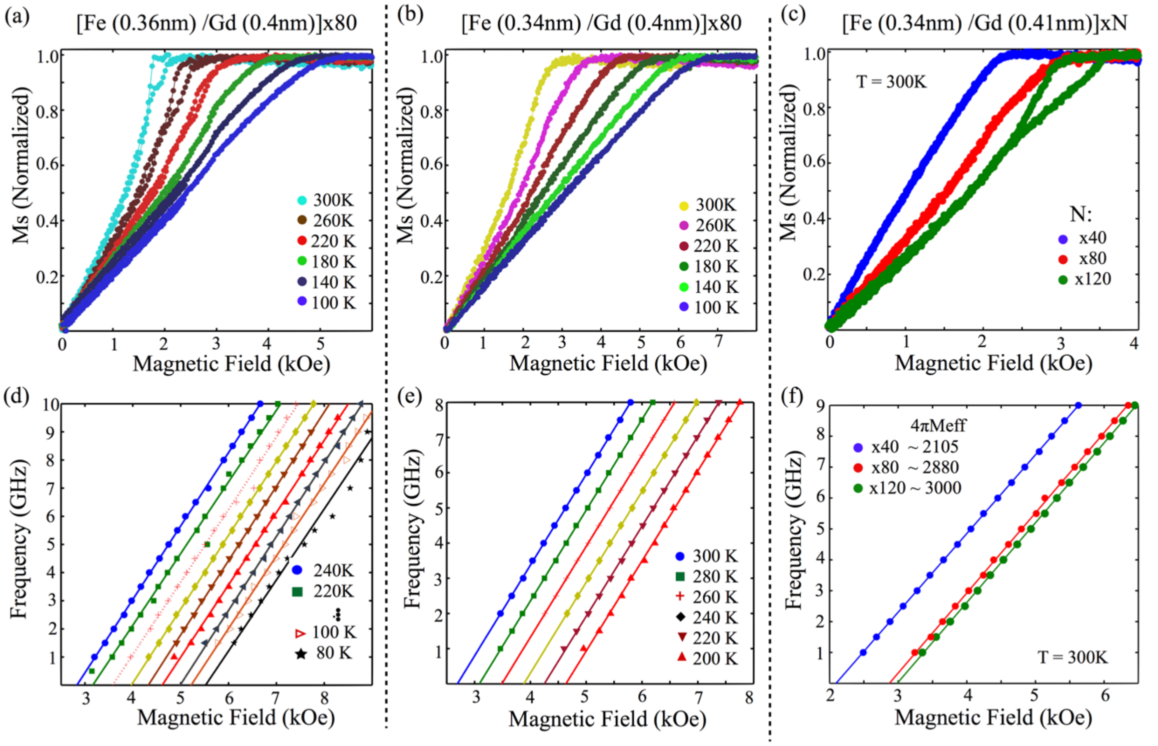

Figure 4.5 – Magnetic properties of Fe/Gd films. (a, b, c) The magnetic hysteresis loops and **(d, e, f)** the Kittel resonance are detailed for Fe/Gd films presented in this work. **(a, b, c)** Show the temperature dependent magnetic hysteresis loops for [Fe (0.36nm)/Gd (0.4nm)]x80, [Fe (0.34nm) /Gd (0.4nm)]x80 and [Fe (0.34nm) /Gd (0.41nm)]xN where N is 40, 80 and 120 repetitions. The films are saturated with a magnetic field of ±10 kOe, but for ease of viewing a smaller field range is illustrated. **(d, e, f)** Depict the field-dependent resonance resulting from the precession of the homogenous magnetization for the Fe/Gd films in **(a, b, c)**.

As the temperature is reduced, in Figure 4.5a, the hysteresis around the nucleation field becomes smaller and softer and the nucleation field is shifted to higher magnetic fields until no identifiable nucleation field exists in [Fe (0.36 nm)/Gd (0.4 nm)]x80. This suggests that the dipolar interaction strength is increasing as the temperature is reduced. Here, our macroscopic magnetic profile agrees with our experimental observation of disordered stripe domains from room temperature down to 200K in [Fe (0.36 nm)/Gd (0.4 nm)]x80. When the temperature is reduced further, the magnetic hysteresis loop appears to suggest the film has undergone a spin-reorientation transition (SRT), yet a closer inspection reveals the films potentially exhibit perpendicular magnetic domains. To verify the orientation of the magnetization, we performed in-plane field magnetic hysteresis measurement and found that the magnetization appears to begin undergoing a temperature driven spin-reorientation transition of the magnetization as we decrease the temperature (Fig 4.6a); however, the magnetization never fully goes in-plane. The in-plane magnetic hysteresis is characteristic of thin films exhibiting stripe domains - they detail that the magnetization lies on both the perpendicular and along the plane of the thin film. If the [Fe (0.36 nm)/Gd (0.4 nm)]x80 had undergone an SRT of the magnetization, then we should expect the in-plane loops to become square-like and have a negative switching field H_k in this measurement geometry. As the temperature is reduced, the switching field H_k decreases rapidly (Fig. 4.6b), but does not become negative. Even at 20K, the [Fe (0.36 nm)/Gd (0.4 nm)]x80 shows evidence of perpendicular magnetic domains. This is also observable in the temperature dependence of the intrinsic anisotropy (Fig. 4.8). Similar observations can be made for [Fe (0.34 nm)/Gd (0.4 nm)]x80. At temperatures where [Fe (0.36 nm)/Gd (0.4 nm)]x80 and [Fe (0.34 nm)/Gd (0.4 nm)]x80 exhibit a skyrmion phase their perpendicular magnetic hysteresis loops are comparable with the exception of different switching fields.

In the case of Fe/Gd bilayer repetitions are varied, we find evidence of perpendicular magnetic domains as the number of bilayers are increased (Fig. 4.5c). The film studied is [Fe (0.34nm) /Gd (0.41nm)]$_{xN}$ where the number bilayer repetitions include N = 40, 80 and 120. At 40 repetitions, there hysteresis clearly shows the magnetization prefers lying along the plane of the film. Above 40 repetitions, the Fe/Gd appears to build sufficient magnetostatic energy to force the system to break into perpendicular magnetic

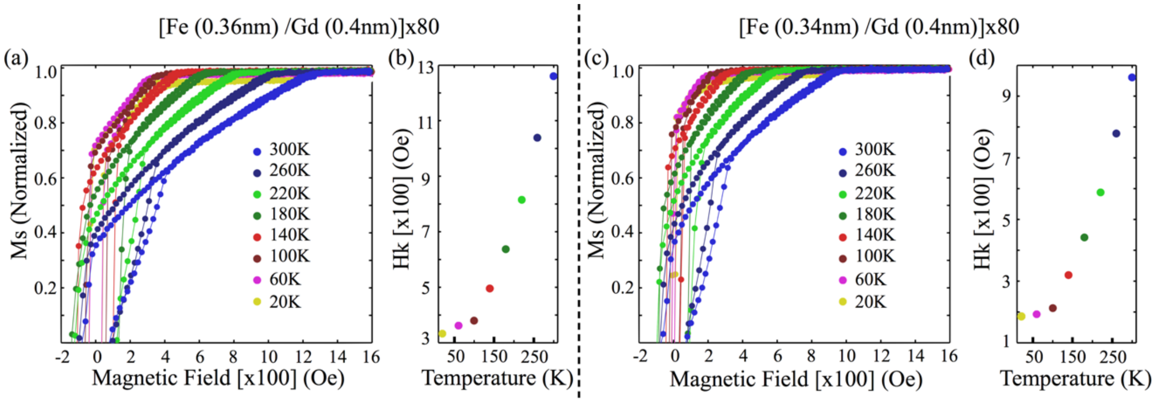

Figure 4.6 – In-plane magnetic properties of Fe/Gd films. (a, c) The temperature dependent normalized in-plane magnetic hysteresis loops are detailed for [Fe (0.36nm) /Gd (0.4nm)]x80 and [Fe (0.34nm) /Gd (0.4nm)]x80. From **(a, c)** the temperature dependent switching field, H_k, is extracted and is illustrated in **(b, d)**. As the temperature is reduced, the switching field decreases swiftly but does not become negative as expected for a perpendicular magnetized films that is characterized by a square hysteresis loop. The films are saturated with a magnetic field of ±10 kOe, but for ease of viewing a smaller field range is illustrated.

domains. We note the magnetic hysteresis is similar to those observed in [Fe (0.36 nm)/Gd (0.4 nm)]x80 and [Fe (0.34 nm)/Gd (0.4 nm)]x80 when a skyrmion phase is present. Then, by further increasing bilayer repetitions, we find that [Fe (0.34nm) /Gd (0.41nm)]x120 shows a magnetic hysteresis loop that also suggests a domain morphology with perpendicular magnetized stripe-like magnetic domains.

Cape and Lehman [26] have calculated the magnetization curves for both the bubble-lattice array and the parallel-stripe array structures and show that both ground states can exhibit near identical magnetic hysteresis profiles. Among the differences, is the slope and shift of the nucleation and collapse critical fields. For instance, the nucleation field of the stripe phase is given by a sharp kink of the magnetization, as detailed previously; whereas, the bubble-lattice phase will show a softer slope change in magnetization around the same nucleation field like that observed in [Fe (0.34nm) /Gd (0.41nm)]x120 (Fig 4.4a, b). All in all, the magnetization curves provide a good macroscopic depiction of the domain morphologies present in the thin films detailed.

To determine required anisotropy at which skyrmions form, we performed ferromagnetic resonance measurements in fixed frequency mode while a perpendicular magnetic field is scanned. By looking at the resonance resulting from the homogenous magnetization precession, known as the Kittel resonance, we can determine the effective magnetization of the specimen. All Fe/Gd films exhibit a positive effective magnetization $4\pi M_{eff}$ which indicates they possess weak perpendicular magnetic anisotropy (Fig. 4.5d, e). Both [Fe (0.34 nm)/Gd (0.4 nm)]x80 and [Fe (0.36 nm)/Gd (0.4 nm)]x80 show a linear increase of the effective magnetization $4\pi M_{eff}$ as the temperature is reduced (Fig. 4.5d, e) which suggests the film becomes more in-plane as the temperature is reduced. For the [Fe (0.34nm) /Gd (0.41nm)] films, we only detail the Kittel resonance at room temperature for all three different bilayer structures. We find that $4\pi M_{eff}$ deviates between 40 repetitions and higher number of bilayer repetitions (Fig. 4.5f). This suggests a microstructural change occurred during the deposition of the 40 repetition stack which resulted in a slightly different film; whereas, both 80 and 120 repetitions have very close effective magnetization values.

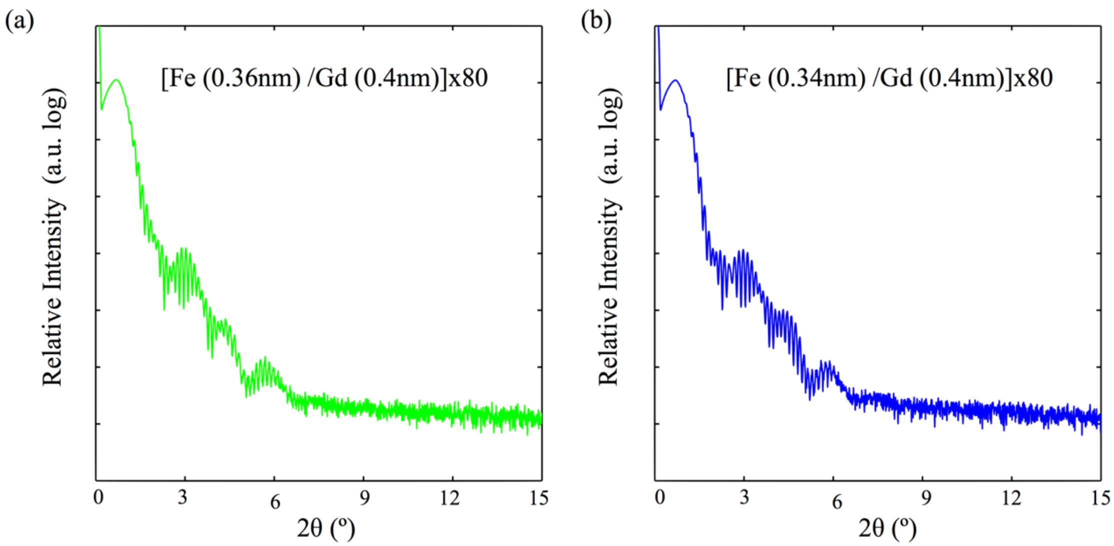

Figure 4.7 – X-ray Reflectivity. The small angle reflectivity for **(a)** [Fe (0.36 nm)/Gd (0.4 nm)]x80 and **(b)** [Fe (0.34 nm)/Gd (0.4 nm)]x80 are detailed from 2θ angles 0º to 15º.

4.8 Small angle x-ray scattering

Small angle x-ray reflectivity (XRR) measurements were performed on the Fe/Gd films to determine accurately the thickness of the Fe/Gd multilayers and to resolve information regarding the bilayers (Fig. 4.7). From the XRR data, we find two oscillating waves superimposed that correspond to the Fe/Gd multilayers (fast oscillations) and the Ta capping layer (slow oscillations). By fitting the XRR data to the modified Bragg law, we find both films are thinner than the expected deposited thickness – [Fe (0.36 nm)/Gd (0.4 nm)]x80 is 51.7 nm and [Fe (0.34 nm)/Gd (0.4 nm)]x80 is 53.6 nm – which suggests the deposited ultra-thin Fe and Gd layers intermix. Both Fe/Gd films show no evidence of super-lattice peaks at any 2θ angles. This suggest the films do not have well defined bilayers throughout the film thickness. Given the individual layers are each a few monolayers thick, strong intermixing between the layers can be expected. As a result, the thin film likely consist of continuously varying alloy-like layers.

4.9 Magnetic and ferromagnetic resonance properties

From magnetic hysteresis loops (Fig. 4.5) measured both by magnetometry and magneto optical Kerr effect measurements, we determine that the Fe/Gd ferrimagnetic moment is Gd rich for these films at all measurement temperatures. This is consistent with measurements of bulk alloys with similar compositions. Both Fe/Gd films show relatively low magnetic moment that varies similarly with decreasing temperature (Fig. 4.8a). The slightly stronger dependence of M_S *vs*. T for the [Fe(0.34nm)/Gd(0.4nm)]x80 is also consistent with the lower Fe content that lead to a higher low-temperature moment and lower T_c compared to the higher Fe content films. At temperatures where the Fe/Gd films exhibit a skyrmion phase, the magnetic moments are similar (Fig. 4.8a) thus does not explain the shift of the skyrmion phase to a different temperature range (Fig. 4.2).

To characterize the anisotropy FMR measurements were performed with perpendicular fields above magnetic saturation (Fig. 4.5). The resonance fields vary linearly with applied magnetic field as expected from the Kittel formula [48], $f = \frac{\gamma_e}{2\pi}(H_{dc} - 4\pi M_S + H_k)$ where γ_e is the e^- gyromagnetic ratio, H_{dc} is the applied field, $4\pi M_S$ is the demagnetization field, M_S is the saturation magnetization and $H_K = 2 \cdot K_U / M_S$ is the perpendicular anisotropy field where K_U is the uniaxial perpendicular anisotropy that is developed in the thin-film growth process. The intercept with the field axis when frequency becomes zero is given when $H_{dc} = 4\pi M_S - H_k = 4\pi M_{eff}$. For all of our films the intercept is

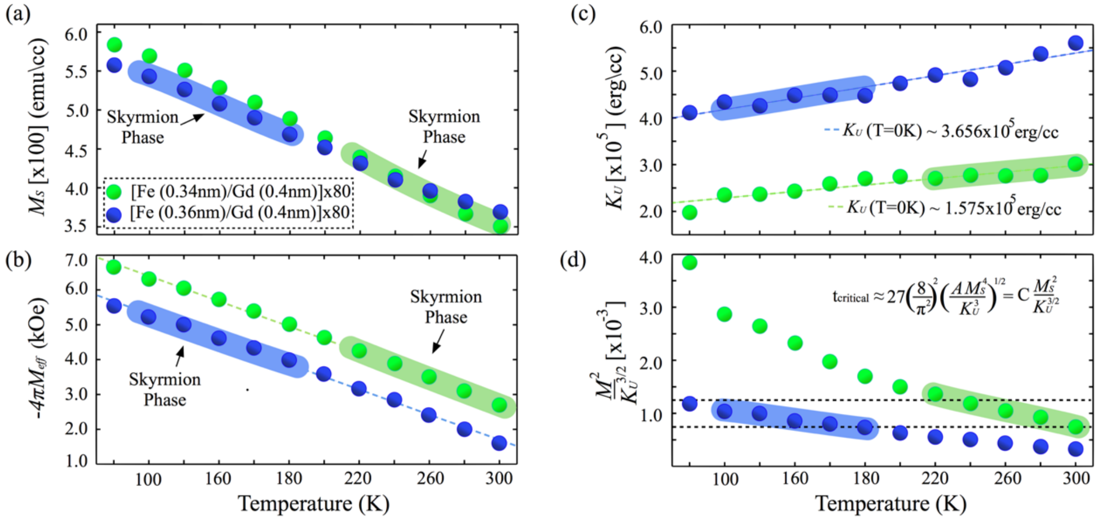

Figure 4.8 – Temperature dependent magnetic and ferromagnetic resonance properties. The magnetization **(a)**, effective magnetization **(b)**, uniaxial anisotropy **(c)** and the $M_S^2/K_U^{3/2}$ ratio **(d)** are shown for **[**Fe (0.34nm)/Gd (0.4nm)]x80 and [Fe (0.36nm)/Gd (0.4nm)]x80. The region in temperature where each Fe/Gd film exhibits a skyrmion phase has been shaded to serve a guide to the eye. By linearly fitting the uniaxial anisotropy with temperature, we can conclude that K_U is positive at absolute-zero (**c**). The enclosed region with dashed lines in **(d)** represents a window of $M_S^2/K_U^{3/2}$values were the both Fe/Gd films exhibit a skyrmion phase.

positive (Fig. 4.5) indicating a relatively weak induced perpendicular anisotropy such that $K_U < K_D = 2\pi M_S^2$ or $Q = K_U/K_d < 1$ so the effective anisotropy is in-plane. The extracted values for M_S, $4\pi M_{eff}$ and K_U are given in Figs. 4.8a-c, respectively, as a function of temperature. As the temperature is reduced, both M_S and $4\pi M_{eff}$ increase roughly linearly with temperature which suggests the films become more in-plane (Fig. 4.8a, b) while a modest decrease of the intrinsic perpendicular anisotropy is observed with decreasing temperature (Fig. 4.8d). This atypical temperature dependence of the intrinsic anisotropy has been previously reported for RE-rich Fe/Gd films with a small bilayer periodicity $t_{Fe} + t_{Gd} \leq 1.4$nm (the Fe/Gd films detailed in this work have a period < 0.8nm) [49,50]. The increase in anisotropy with increasing Fe layer thickness is observed in a series of films and appears to be a general feature of the Fe/Gd system. We have further indicated in Fig. 4.8 the regions in temperature where we observe the skyrmion lattice phase.

The fact that domains and skyrmion lattices are only observed for film thickness above a critical thickness is consistent with earlier studies of films where $K_U<K_d$ [40-44]. There are theoretical estimates for the critical thickness for the onset of weak stripe domains given by [Refs. 41, 43]:

$$t_1 \sim 17.7\sqrt{A}\, M_S^2 / K_U^{3/2} \tag{4.2}$$

where A is the exchange parameter. The predicted value for the thickness at which the magnetization rotates from in plane to out of plane with stripe domains is given by [Refs. 28, 41, 44]:

$$t_2 \sim 27.2\sqrt{A}\, M_S^2 / K_U^{3/2} \tag{4.2}$$

In both cases the critical thickness scales as $M_S^2/K_U^{3/2}$. In Fig. 4d we plot this ratio as a function of temperature. We see this ratio increases with decreasing temperature reflecting the strong temperature dependence of the saturation magnetization. We also find that we experimentally observe the skyrmion phase for the same range of this ratio from 0.735x10^{-3} to 1.359x10^{-3} as shown in Fig. 4.8d. While neither the values of M_S or K_U appear predictive for determining the temperature range where we observe the skyrmion the ratio as $M_S^2/K_U^{3/2}$ does provide a guideline to the formation of the skyrmion phase for the Fe/Gd system.

The only material parameter in Eqs. (4.1) and (4.2) we do not have a quantitative measure of is the exchange stiffness constant A, however, a qualitative measure can be deduced from noting that no super-lattice peaks are observable in small angle x-ray reflectometry (Fig. 4.7). This suggest that there is strong intermixing between the Fe and Gd layers; as a consequence, we can assume the Fe/Gd films are layered alloy-like structures that resemble an Fe-Gd alloys of similar composition. For this reason, we assume an exchange stiffness A between 2 - 5x10^{-7} erg/cm based on values reported for similar Fe-Gd alloys [51-54]. Using these values of A we would predict a t_I in the range 50.2 nm < t_I < 79.4 nm in reasonable agreement for the transition from in-plane to stripe phase between 40 and 80 repeats as observe experimentally.

4.10 Micromagnetic modeling

To understand the mechanism stabilizing the skyrmion phase, we performed numerical simulations of the Landau-Lifshitz-Gilbert (LLG) equation, utilizing the FASTMag [55] solver for a magnetic slab that is 2000 nm x 2000 nm x 80 nm. The input magnetic parameters were obtained from experiment (for further details see Figure captions and Methods). Shown in Fig. 4.9 is the field evolution of equilibrium states that results for M_S = 400 emu/cm^3, K_U = 4x10^5 erg/cm^3 and A= 5x10^{-7} erg/cm. These values are within the range of magnetic properties of both [Fe (0.34nm) /Gd (0.4nm)]x80 and [Fe (0.36nm) /Gd (0.4nm)]x80 (Fig. 4.8). Initially the slab is saturated along the z-axis and then the perpendicular field is reduced to zero-field. At any field step the slab is allowed 30 ns to relax into an equilibrium state. Figures 4.9a (top view) and 4.9b (side view) are the results at zero-field that exhibit a configuration of disordered stripe domains similar to those observed in Fig. 4.1. The typical domain periodicity is ~183 nm. The cross-section view of the magnetization across the film thickness along the line given in Fig. 4.9a reveals a Bloch-like wall configuration at the center of the slab (Fig. 4.9b m_y component) while near the top and bottom of the film there are flux closure caps (Fig. 4.9b, m_x component). This domain arrangement is expected given the low Q-factor ($Q \sim 0.4$) as previously determined by resonant x-ray scattering from Fe/Gd films [47].

When a magnetic field is applied perpendicular to the slab, the stripe domain with magnetization opposite to the field direction collapse into individual skyrmions (Fig. 4.9c-e). As the magnetic field is increased further, the chiral textures arrange into a hexagonal lattice that exists from $H_{dc} = 1700$ Oe to 2300 Oe (Figs. 4.9f, g, n-r). The typical skyrmion size is ~83 nm and the separation is given by ~128 nm at $H_{dc} = 1700$ Oe. As the magnetic field is increased, the skyrmion size decreases to 53 nm at $H_{dc} = 2700$ Oe. The skyrmion size, separation and field history are in good agreement with our experimental observation. For Figs. 4.9a, c-g and n-r we plot the m_z component for magnetization which can be compared to the contrast in Fig. 4.4.

For the skyrmions that form in Fig. 4.9 the domain walls are Bloch-like in the center of the film and we find a roughly 50% percent chance of the two helicities. This can be seen in Fig. 4.9g where we plot the m_x component of magnetization at the center of the slab for H_{dc} =1700 Oe. The skyrmions where m_x component is red above the skyrmion and blue below have one circulation of the domain wall and we characterize it by a winding number $S = 1$, $\gamma = -\pi/2$. The skyrmions where m_x component is blue above the skyrmion and red below have the opposite circulation and we characterize it by a winding number $S = 1$, $\gamma = \pi/2$. These results agree with the LTEM images of Fig. 4.1. By tracking the orientation of the in-plane components of the domain walls in Fig. 4.9 with increasing applied field we

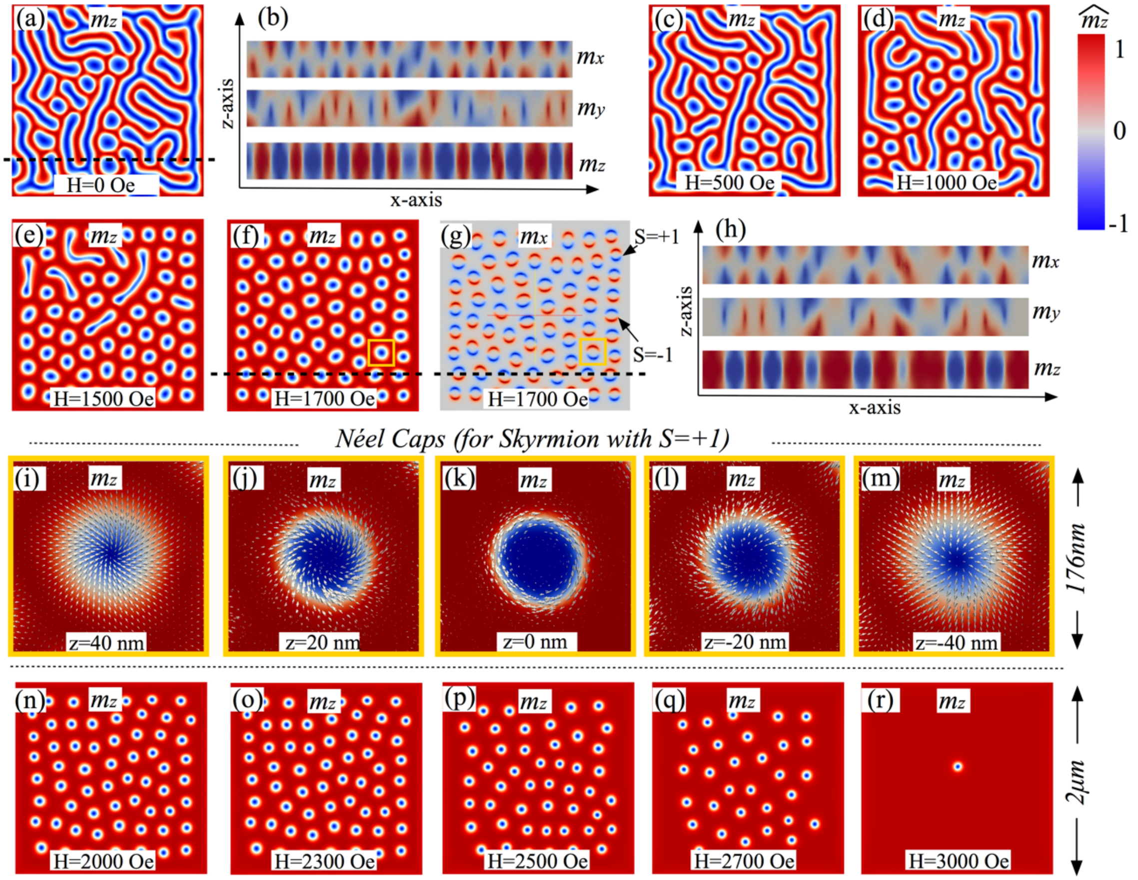

Figure 4.9 – Micromagnetic modeling of domain morphology. (a-r) [M_S = 400 emu/cm^3, K_U=4x10^5 erg/cm^3 and A=5x10^{-7} erg/cm] The equilibrium states illustrate the field dependent domain morphology at several magnetic fields that capture the domain evolution from a stripe to a skyrmion phase. These equilibrium state primarily depict the top side view of the magnetization along the z-axis (m_z) at the top surface of the slab (z=40nm). The magnetization (m_z) is represented by regions in red (+m_z) and blue (-m_z); whereas the in-plane magnetization (m_x, m_y) is represented by white regions surrounding the blue features. **(b, h)** Illustrates the lateral magnetization components (m_x, m_y, m_z) across the film thickness for the disordered stripe domains in **(a)** and the skyrmion phase in **(f, g)** along the dashed line. Inspection along the lateral magnetization reveals a Bloch-like wall configuration with closure domains in both states. The chirality of the skyrmions is depicted in **(g)** along top side-view of m_x across the center of the slab. **(i-m)** Detail the magnetization distribution at different depths (z=40, 20, 0, -20, -40nm) for a skyrmion with chirality S = +1, γ= -π/2 that is enclosed in a box in **(f, g).** At each depth, the perpendicular magnetization is represented by blue (-m_z) and red (+m_z) regions and the in-plane magnetization distribution (m_x and m_y) is depicted by white arrows. The white arrows illustrate how the magnetization of the closure domains and Bloch-line arrange at different depths of the slab. **(n-r)** Detail the field evolution from an ordered skyrmions to disordered skyrmions.

find that the chirality of the skyrmions is determined by the chirality of the walls of the original domain. There are also examples of bubbles that form where the m_x component is either red or blue above and below the bubble and we characterize this by a winding number S=0. Such bubbles are also observed in LTEM experiments.

Shown in Fig. 4.9h is the magnetic projection through the thickness of the film for the dashed line shown in Figs. 4.9f and 4.9g. The m_z projection shows that the core of the skyrmion extends through the thickness of the film but narrows slightly near the top and bottom of the film. The m_y projection shows the circulating Bloch walls around each skyrmion and the m_x projection shows the existence of closure domains at the top and bottom of the films (this is shown in more detail in Fig. 4.9i-m). These closure domains will not be seen in the experimental images in Figs. 4.1 and 4.4 because both LTEM and transmission x-ray microscopy average over of the thickness of the film. As seen in Fig. 4.9h the closure domains have the opposite sign at the top and bottom of the films and will average out in a transmission experiment.

The details of the domain-wall structure for one S= 1, $\gamma = -\pi/2$ skyrmion are shown in Fig. 4.9i-m. Shown are slices for different depths within the slab where the color gives m_z and the arrows give the direction of the in-plane magnetic component and length corresponds to the magnitude of m_x and m_y. At the center of the slab (z = 0nm), m_x and m_y continuously wrap around the skyrmion forming a Bloch wall and the wall width is the narrowest. As one progresses towards the top (z = 40 nm) or bottom (z = -40nm) surface you see the domain wall broadens and becomes more Néel like. At the top surface the in-plane magnetization points mostly radially in forming the Néel caps. At the bottom surface

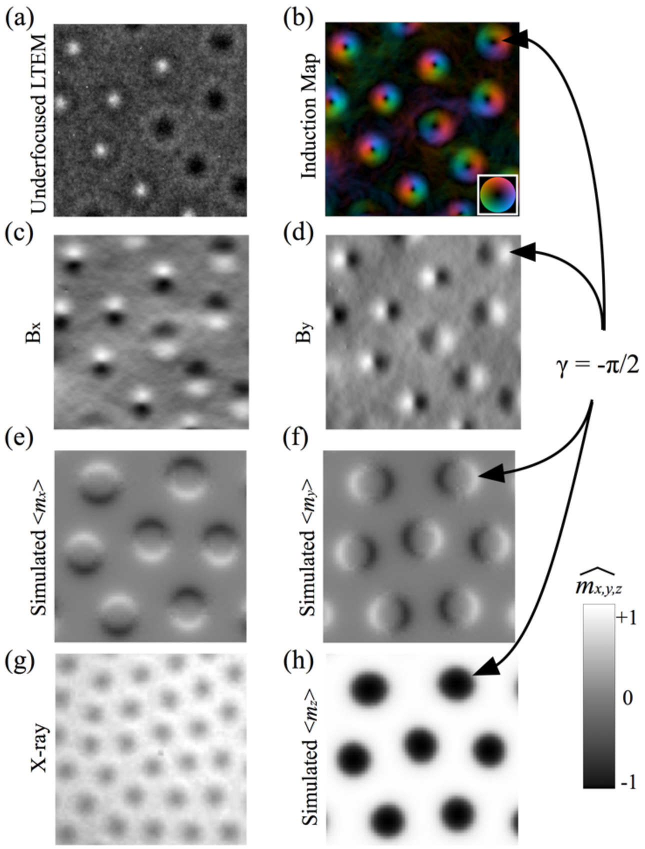

Figure 4.10 - Comparison between numerical and experimental observation of skyrmions. (a, b) Under-focused LTEM image and its corresponding magnetic induction map illustrate the Bloch-line arrangement of the skyrmions. **(c, d)** The individual in-plane components of the magnetic induction B_x and B_y are obtained from **(b)**. **(e, f)** Detail a numerical computed average magnetization across the slab for $<m_x>$ and $<m_y>$. **(g)** A transmission X-ray microscopy of the skyrmion phase solely shows the presence of cylindrical domains which resembles the average magnetization across the slab for $<m_z>$ in **(h)**. A skyrmion with S = 1, $\gamma = \pi/2$ is referenced to directly compare experimental and numerical results in **(b, d, f, h)**. The scale bar references the micromagnetic domain states.

the in-plane magnetization now points away from the skyrmion center. For a skyrmion with opposite helicity, the wrapping of m_x and m_y toward the center of the skyrmion core is inverted; while, the Néel cap configuration at the top and bottom of the slab is the same.

For higher fields the skyrmions become disordered and begin to disappear, first at the edges and then throughout the film as the field approaches magnetic saturation (Figs. 4.9n-r). Overall, the field dependent domain morphology is in good agreement with our experimental observations. Here the micromagnetic model suggests the chiral bubble domains form due to minimization of competing demagnetization energy and domain wall energy, and that thermal fluctuations are not required for their formation since this is a zero-temperature model. To compare our numerical results to our experimental observations of chiral cylindrical textures we computed the magnetization projection averaged over the film thickness. This is shown in Fig. 4.10 for $<m_z>$ and $<m_x>$ and are compared to selected LTEM and x-ray images. There is no signature of the different helicities of the $<m_z>$ as expected and consistent the x-ray images. The $<m_x>$ and $<m_y>$ projection is only sensitive to the Bloch nature of the wall as seen in LTEM.

Next, we discuss the magnetic properties required to stabilize a dipolar field driven skyrmion phase. As we have demonstrated the composition of the Fe/Gd specimen directly correlates the temperature and applied magnetic field range in which skyrmions become favorable particularly a window of $M_S^2/K_U^{3/2}$ values. To understand the effect of exchange A in the formation of a skyrmion phase we simulated magnetic domains similar to those in Fig. 4.9 for a fixed applied field H_z = 2000 Oe and M_S = 400 emu/cm^3 and various K_U and A values are shown in Fig. 4.11a. We find that modest changes in either of these parameters leads to different equilibrium states. For instance, as K_U is increased, the skyrmion lattice quickly becomes less correlated and the skyrmion size begins to vary. Increasing the exchange A, for any fixed K_U except K_U = 2x10^5 erg/cm^3, results in a skyrmion arrangement

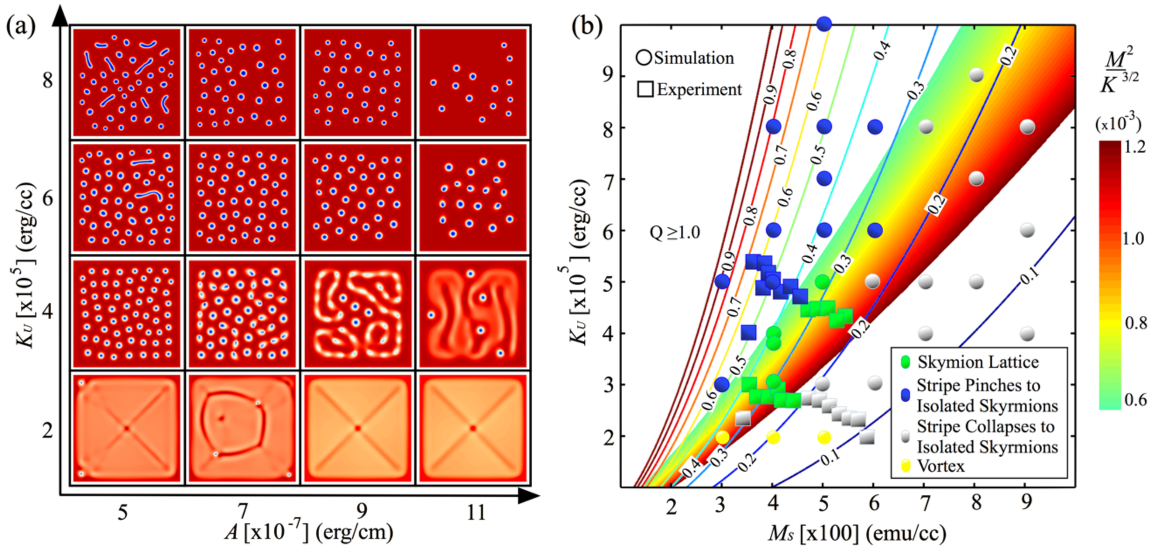

Figure 4.11 – Skyrmion phase stability in magnetic phase maps. (a) The top side view of equilibrium states that form at H_z = 2000 Oe are investigated under different ratios of K_U and A for a fixed M_S = 400 emu/cm^3. These equilibrium states detail the magnetization along the z-axis (m_z) at the top surface of the slab (z=40nm). The magnetization (m_z) is represented by regions in red (+m_z) and blue (-m_z); whereas the in-plane magnetization (m_x, m_y) is represented by white regions surrounding the blue features. **(b)** The formation of a skyrmion lattice is explored in terms of varying M_S and K_U for a fixed A = 5x10^{-7} erg/cm using a combination of experimental results (□) and simulations (○). Contour lines detail the corresponding Q-factor in this magnetic phase region, which denotes the balance between anisotropy energy K_U and magneto-static energy $2\pi M_S^2$.

that becomes more disordered. For a fixed M_S, a close packing lattice of skyrmions is only achievable in a narrow region of both K_U and A. Our modeling suggests a modest value of the exchange parameter is a critical parameter that determines the long-range order of skyrmions forming a lattice, and supports the existence of a weak exchange in these Gd-rich Fe/Gd films.

4.11 Discussion

Using a combination of numerical simulations and experimental data, we have constructed a K_U-M_S phase map (for a fixed A = 5x10^{-7} erg/cm) that illustrates the measured and calculated magnetic domains at zero-field and applied field values (Fig. 4.11b). In the phase map, the Q-ratio is also plotted in the foreground with contour lines depicting variations in $Q = K_U/2\pi M_S^2$ for domain states with Q<1. The Q-ratio serves as a heuristic to estimate volume fraction distributions of perpendicular domains and Néel caps in these thick Fe/Gd films. We recall that when films exhibit a Q-ratio greater than 1, the domain morphology favors perpendicular domains with negligible Néel caps; likewise, as Q decreases below 1 the volume fraction of the Néel caps grows and the perpendicular domains occupy a lower volume fraction.

Inspecting the domain states when the anisotropy is very low ($K_U \leq$ 2x10^5 erg/ cm^3) such that the thickness is below t_I (Eq. 1) we find the magnetization is in-plane and as a result of the geometry of the slab, the system favors the formation of an in-plane vortex configuration. For larger K_U (or lower M_S) the film transitions to out-of-plane magnetic domains. The two predominant magnetic configurations consist of labyrinth domains at zero-field that form skyrmions when a field is applied perpendicular to the slab. What differentiates the regions are the mechanisms by which the skyrmions form, in one case: (i) the stripes pinch-off into chiral bubbles as seen in Fig. 4.9, and in the other (ii) the extremities of the stripe collapse to form single chiral bubbles that do not arrange in a lattice as seen in Co/Pt multilayers [56] for instance. For only a small region of K_U and M_S values do we observe the skyrmions arranging in a close packing lattice; in addition, this region exists at Q-value ratios from 0.2 to 0.4 which suggests the overall domain structure of perpendicular domains and Néel caps is fairly comparable. As we move away from the skyrmion lattice region, the distance between the cylindrical textures increases until they become disordered.

In the foreground of Fig. 4.11b we also detail the range of $M_S^2/K_U^{3/2}$ values where an ordered skyrmion phase is observable numerically and experimentally. Equilibrium states within this region of varying M_S and K_U will share similar critical thickness t_l, for a fixed A, at which weak perpendicular stripe domains will form, but only a small region of low M_S and K_U results in a close packing lattice of skyrmions. Large M_S and K_U result in stripe domains that form disordered chiral bubbles. This suggests that the critical thickness is not a sole determinate of ordered skyrmions.

The LTEM images (Fig. 4.1) and numerical simulations (Fig. 4.9, 4.11) suggests the stabilization of these skyrmions is purely driven by competing dipolar and exchange energies and that no DMI is present in these films. The LTEM images show two helicity textures with an equal population distribution in the skyrmion phase. If some DMI were present, then the system would likely favor the formation of a chiral domain compared to the other, as well as a Néel cap orientation over the other which is not the case here. The fact that we numerically observe the stabilization of the same 2-helicity skyrmions on a slab with no DMI supports this observation. Given the nature of these skyrmions, these films could potentially also be designed to host anti-skyrmions as recently theoretically predicted [57]. Unlike bubble domains which typically observed in materials with $Q > 1$ and exhibit strong PMA, our chiral cylindrical domains appear in a material parameter space where $Q < 1$ and the formation of perpendicular domains results from a thickness driven domain morphology rearrangement [40-44].

In conclusion, we have demonstrated the existence of skyrmion lattice in Fe/Gd films by means of real and reciprocal space imaging techniques. We have shown that by tuning the magnetic properties and film thickness we can control the stabilization of a skyrmion phase in temperature and applied magnetic fields. The simplicity of the magnetic material and the easily tunable properties makes it of interest as a potential test bed for studying physics of skyrmions, as well as, for potential memory technologies. Furthermore, the universality of our numerical model presents a roadmap to design new classes of materials that can exhibit dipolar field driven skyrmions.

Acknowledgement: Chapter 4 is a reprint of the journal article: S. A. Montoya, S. Couture, J. J. Chess, J. C. T. Lee, N. Kent, D. Henze, S. K. Sinha, M.-Y. Im, S. D. Kevan, P. Fischer, B. J. McMorran, V. Lomakin, S. Roy and E. E. Fullerton. *Tailoring magnetic energies to stabilize dipole skyrmions and skyrmion lattices*. PRB Submitted. arXiv:1608.01368 (2016). The dissertation author was the primary author of this article.

4.12 References

[1] T. H. R. Skyrme, *A unified field theory of mesons and baryons*. Nuclear Phys. 31, 556-569 (1962).

[2] N. Nagaosa and Y. Tokura, *Topological properties and dynamics of magnetic skyrmions*. Nat. Nanotechnol. **8**, 899-911 (2013).

[3] H.-B. Braun, *Topological effects in nanomagnetism: from superparamagnetism to chiral quantum solitons.* Adv. Phys. **61:1**, 1-116 (2012).

[4] S. P. Parkin, M. Hayashi and L. Thomas, *Magnetic domain-wall racetrack memory*, Science **320**, 190-194 (2008).

[5] N. S. Kiselev, A. N. Bogdanov, R. Schafer and U. K. Robler, *Chiral skyrmions in thin magnetic films: new objects for magnetic storage technologies*. J. Phys. D: Appl. Phys. **44**, 392001 (2011).

[6] A. Fert, V. Cros and J. Sampaio, *Skyrmions on the track*. Nature Nanotech. **8**, 152–156 (2013).

[7] S. Mühlbauer, B. Binz, F. Jonietz, C. Pfleiderer, A. Rosch, A. Neubauer, R. Georgii and P. Böni. *Skyrmion lattice in a chiral magnet*. Science **323**, 915-919 (2009)

[8] W. Münzer, A. Neubauer, T. Adams, S. Mühlbauer, C. Fran, F. Jonietz, R. Georgii, P. Böni, B. Pedersen, M. Schmidt, A. Rosch and C. Pfleiderer. *Skyrmion lattice in the doped semiconductor FeCoSi*, Phys. Rev. *B*. **81**, 041203(R) (2010).

[9] X. Z. Yu, Y. Onose, N. Kamazawa, J. H. Park, J. H. Han, Y. Matsui, N. Nagaosa and Y. Tokura. *Real-space observation of a two-dimensional skyrmion crystal*. Nature **465**, 901–904 (2010).

[10] S. Seki, X. Z. Yu, S. Ishiwata and Y. Tokura, *Observation of skyrmions in a multiferroic material.* Science **336**, 198-201 (2012).

[11] X. Z. Yu, N. Kanazawa, Y. Onose, K. Kimoto, W. Z. Zhang, S. Ishiwata, Y. Matsui and Y. Tokura. *Near room-temperature formation of a skyrmion crystal in thin-films of the helimagnet FeGe.* Nat. Mater. **10**, 106-109 (2011).

[12] W. Jiang, P. Upadhyaya, W. Zhang, G. Yu, M. B. Jungfleisch, F. Y. Fradin, J. E. Pearson, Y. Tserkovnyak, K. L. Wang, O. Heinonen, S. G. E. te Velthuis, A. Hoffmann. *Blowing Magnetic Skyrmion Bubbles.* Science **349**, 283 (2015).

[13] C. Moreau-Luchaire, C. Moutafis, N. Reyren, J. Sampaio, C. A. F. Vaz, N. Van Horne, K. Bouzehouane, K. Garcia, C. Deranlot, P. Warnicke, P. Wohlhüter, J.-M. George, M. Weigand, J. Raabe, V. Cros and A. Fert. *Additive interfacial chiral interaction in multilayers for stabilization of small individual skyrmions at room temperature,* Nat. Nanotech. **11**, 444-448 (2016).

[14] S. Woo, K. Litzius, B. Krüger, M.-Y. Im, L. Caretta, K. Richter, M. Mann, A. Krone, R. M. Reeve, M. Weigand, P. Agrawal, I. Lemesh, M.-A. Mawass, P. Fischer, M. Kläui and G. S. D. Beach. *Observation of room-temperature magnetic skyrmions and their current-driven dynamics in ultrathin metallic ferromagnets*. Nat. Mat. **15**, 501-506 (2016).

[15] W. Wang, Y. Zhang, G. Xu, L. Peng, B. Ding, Y. Wang, Z. Hou, X. Zhang, X. Li, E. Liu, S. Wang, J. Cai, F. Wang, J. Li, F. Hu, G. Wu, B. Shen and X.-X. Zhang. *A centrosymmetric hexagonal magnet with superstable biskyrmion magnetic nanodomains in a wide temperature range of 100K-340K*. Adv. Mater. 1521-4095 (2016).

[16] J. C. T Lee, J. J. Chess, S. A. Montoya, X. Shi, N. Tamura, S. K. Mishra, P. Fischer, B. J. McMorran, S. K. Sinha, E. E. Fullerton, S. D. Kevan and S. Roy. *Synthesizing skyrmion bound pairs in Fe-Gd films*. Appl. Phys. Lett. **109**, 022402 (2016).

[17] X. Z. Yu, K. Shibata, W. Koshibae, Y. Tokunaga, Y. Kaneko, T. Nagai, K. Kimoto, Y. Taguchi, N. Nagaosa and Y. Tokura. *Thermally activated helicity reversal of skyrmions*. Phys. Rev. *B* **93**, 134417 (2016).

[18] X. Z. Yu, M. Mostovoy, Y. Tokunaga, W. Zhang, K. Kimoto, Y. Matsui, Y. Kaneko, N. Nagaosa and Y. Tokura. *Magnetic stripes and skyrmions with helicity reversals*. Proc. Natl Acad. Sci. USA **109**, 8856–8860 (2012).

[19] I. Dzyaloshinskii*, A thermodynamic theory of "weak" ferromagnetism of antiferromagnetics*. J. Phys. Chem. Solids **4**, 241–255 (1958).

[20] T. Moriya, *Anisotropic superexchange interaction and weak ferromagnetism*. Phys. Rev. Lett. **120**, 91–98 (1960).

[21] S. Heinze, K. von Bergmann, M. Menzel, J. Brede, A. Kubetzka, R. Wiesendanger, G. Bihlmayer and S. Blüger. *Spontaneous atomic-scale magnetic skyrmion lattice in two dimensions.* Nature Phys. **7**, 713-718 (2011).

[22] T. Okubo, S. Chung and H. Kawamura, *Multiple-q states and the skyrmion lattice of the triangular-lattice heisenberg antiferromagnet under magnetic fields*. Phys. Rev. Lett. **108**, 017206 (2012).

[23] C. Kittel, *Physical theory of ferromagnetic domains*. Rev. Mod. Phys. **21**, 541 (1949).

[24] C. Kooy and U. Enz, *Experimental and theoretical study of the domain configuration in thin layers of* $BaFe_{12}O_{19}$. Philips, Res. Rep. **15**, 7 (1960).

[25] Y. S. Lin, J. Grundy and E. A. Giess, *Bubble domains in magnetostatically coupled garnet films*. Appl. Phys. Lett. **23**, 485–487 (1973).

[26] J. A. Cape and W. Lehman, *Magnetic domain structures in thin uniaxial plates with perpendicular easy axis.* J. Appl. Phys. **42**, 13 (1971).

[27] A. Thiele, *Theory of the static stability of cylindrical domains in uniaxial platelets*. J. Appl. Phys. **41**, 1139 (1970).

[28] Z. Malek and V. Kambersky, *On the theory of the domain structure of thin films of magnetically uni-axial materials*. Czech. J. Phys. **8**, 416 (1958).

[29] C. Kittel, *Theory of the structure of ferromagnetic domains in films and small particles.* Phys. Rev. **70**, 965 (1946).

[30] O. Hellwig, A. Berger, J. B. Kortright and E. E. Fullerton, *Domain structure and magnetization reversal of antiferromagnetically coupled perpendicular films*. J. Magn. Magn. Mater. **319**, 13-55 (2007).

[31] M. Seul, L. O. Monar, L. O'Gorman and R. Wolfe, *Morphology and local structure in labyrinthine stripe domain phase.* Science **254**, 1616-1618 (1991).

[32] M. Seul and R. Wolfe, *Evolution of disorder in magnetic stripes domains I. Transverse instabilities and disclination unbinding in lamellar patterns*. Phys. Rev. A **46**, 7519-33 (1992).

[33] M. Seul and R. Wolfe, *Evolution of disorder in magnetic stripes domains I. Hairpins and labyrinth patterns versus branches and comb patterns formed by growing minority component.* Phys. Rev. *A* **46**, 7534 (1992).

[34] A. P. Malozemoff, J. C. Slonczewski and R. Wolfe, *Magnetic Domain Walls in Bubble Materials* (Academic Press, 1979) p306-314.

[35] A. Hubert and R. Schäfer, Magnetic Domains (Springer, Berlin, 1998), p. 499 p. 509.

[36] T. Suzuki, *A study of magnetization distribution of submicron bubbles in sputtered Ho-Co thin films.* J. Magn. Magn. Mater. 31-34, 1009–1010 (1983).

[37] A. H. Eschenfelder, *Magnetic Bubble Technology* (Springer, Berlin, 1981), p.210-224.

[38] P. Chaudhari, J. J. Cuomo and R. J. Gambino*, Amorphous metallic films for magneto-optic applications.* Appl. Phys. Lett. **22**, 337 (1973).

[39] N. Sato and N. Habu, *Amorphous rare-earth-transition-metal thin films with an artificial layered structure*. J. Appl. Phys. **61**, 4287 (1987).

[40] M. W. Muller, *Domain formation in a ferrimagnet plate*. J. Appl. Phys. **38**, 6 (1967).

[41] M. Hehn, S. Padovani, K. Ounadjela and J. P. Bucher, *Nanoscale magnetic domain structures in epitaxial cobalt films*. Phys. Rev. *B* **54**, 3428 (1996).

[42] D. M. Donnet, K. M. Krishnan and Y. Yajima, *Domain structures in epitaxially grown cobalt thin films.* J. Phys. D: Appl. Phys. **28** (1995).

[43] N. Saito, H. Fujiwara and Y. Sugita, *A new type of magnetic domain structure in negative magnetostriction Ni-Fe films.* J. Phys. Soc. Jpn. **19**, 1116 (1964).

[44] D. J. Craik and P. V. Cooper, *The evaluation of magnetic bubble domain specimens*. Phys. Lett. **41A**, 255 (1972).

[45] M. R. Teague, *Deterministic phase retrieval: a Green's function solution.* JOSA **73**, 1434-1441 (1983).

[46] M. De Graef and Y. Zhu, *Magnetic imaging and its applications to materials* (Academic Press, 2000) Vol. 36, p. 58-68.

[47] J. Miguel, J. F. Peters, O. M. Toulemonde, S. S. Dhesi, N. B. Brookes and J. B. Goedkoop. *X-ray resonant magnetic scattering study of magnetic stripe domains in a-GdFe thin films.* Phys. Rev. *B* **74**, 094437 (2006).

[48] C. Kittel, *On the theory of ferromagnetic resonance absorption.* Phys. Rev. **73** 155 (1948).

[49] E. Stavrou and E. Roll, *Magnetic anisotropy in Gd\(FeCo) and Gd\Fe multilayers for high density magneto-optical recording.* J. Appl. Phys. **85**, 5971 (1999).

[50] E. Stavrou, R. Sbiaa, T. Suzuki, S. Knappmann and K. Roll, *Magnetic anisotropy and spin reorientation effects in Gd\(Fe, Co) multilayers for high density magneto-optical recording.* J. Appl. Phys. **87**, 6899 (2000).

[51] C. Vittoria, P. Lubitz and V. Ritz, *Magnetic Properties of amorphous and crystalline* $GdFe_2$. J. Appl. Phys. **49**, 4908 (1978).

[52] Y. Mimura, N. Imamura, T. Kobayashi, A. Okada and Y. Kushiro. *Magnetic Properties of amorphous alloy films of Fe with Gd, Tb, Ho, or Er.* J. Appl. Phys. **49**, 1208 (1978).

[53] M. Mansuripur and M. F. Ruane, *Mean-field analysis of amorphous rare earth-transition metal alloys for thermomagnetic recording*. IEEE Trans. Magn. Mag. **22**, No. 1 (1986).

[54] P. Lubitz, J. Schelleng and C. Vittoria, *Microwave magnetic properties of gadolinium-iron films.* Solid State Comm. **18**, 995 (1976).

[55] R. Chang, S. Li, M. V. Lubarda, B. Livshitz and V. Lomakin, *FastMag: Fast micromagnetic simulator for complex magnetic structures.* J. Appl. Phys. **109**,

07D358 (2011).

[56] J. E. Davies, O. Hellwig, E.E. Fullerton, G. Denbeaux, J. B. Kortright and K. Liu, *Magnetization reversal of Co/Pt multilayers: Microscopic origin of high field magnetic irreversibility*. Phys. Rev. B. **70**, 22 (2004).

[57] W. Koshibae and N. Nagaosa, *Theory of antiskyrmions in magnets*. Nat. Comm. **7**, 10542 (2016).

Chapter 5

Resonant Properties of Dipole Skyrmions

5.1 Introduction

Skyrmions have been suggested as a building block for next generation mobile technologies [1-3]. In order to facilitate the detection, control and manipulation of these magnetic textures, it is necessary to understand their dynamic response. Recently, it was shown that skyrmions stabilized by DMI exhibit local spin wave interactions that are independent of the class of material in which they form [4]. Insulating, semiconducting and metallic systems all exhibit similar spin-wave excitations that are solely dependent on the resonant mode and perturbation geometry [4, 5]. The skyrmion dynamics under an in-plane microwave field is numerically predicted to result in the clockwise or counter-clockwise rotation of the spins inside the skyrmion core [6]; whereas a perpendicular *r.f.* field perturbation results in the skyrmion core expansion and contraction, termed a breathing mode [6-8]. However, there is no current evidence that suggests that skyrmions stabilized by different mechanisms should exhibit similar spin wave modes.

Here we describe the rich spectrum of resonant modes that result from magnetic domains ranging from stripes, magnetic bubbles and dipole-stabilized skyrmions in amorphous Fe/Gd multilayers. The formation of skyrmions and skyrmion bound pairs in this class of material was previously reported in Refs. 9 and 10. Utilizing a broad-band coplanar waveguide technique, we have studied the resonant behavior of the magnetic textures as a function of temperature and thickness. In addition, we have performed numerical simulations of the Landau-Lifshitz-Gilbert (LLG) equation under time-dependent *r.f.* magnetic fields to determine the resonant modes and spin configurations of these magnetic domains. Our modeling results in frequency-field dispersions that agree with our experimental observations, and suggest the existence of new localized spin wave modes.

5.2 Temperature dependence of the resonant modes

To clearly distinguish the resonant properties that arise from a dipole skyrmion phase, we investigated the temperature dependence of an [Fe(0.36nm)/Gd(0.4nm)]x80 multilayer [9,10]. This sample exhibits disordered stripe domains above 180K for magnetic fields below saturation and further shows a transition from disordered stripes to a dipole skyrmion lattice from 180K to 100K when a magnetic field is applied perpendicular to the film [9,10]. Unlike in DMI materials, the dipole skyrmion phase consists of an equal population of domains with two possible helicities. As described in Chapter 4.4, these magnetic domains are primarily identified with soft x-ray scattering and LTEM. When we

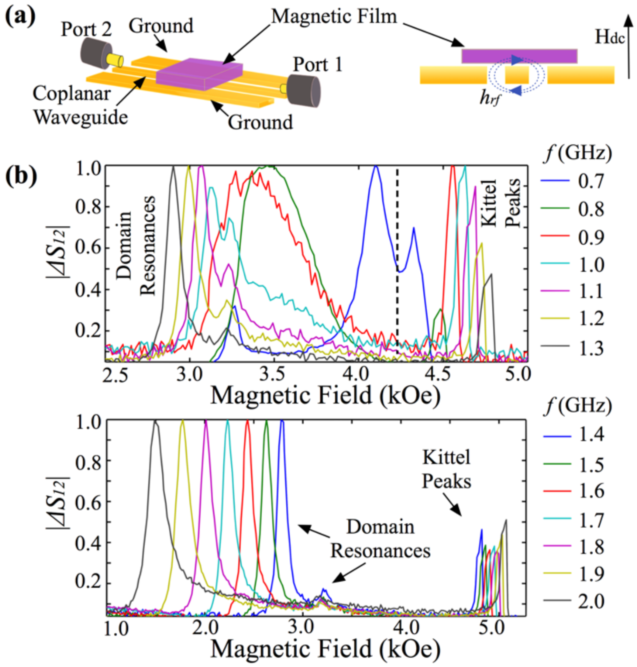

Figure 5.1 – Magnetic morphology and absorption spectra. (a) Shows the schematic of the experimental set-up. **(b)** The normalized absorption spectra, measured at 160K, is obtained while sweeping a perpendicular magnetic field, from H_z= -10 KOe to +10 KOe, at a fixed frequency h_{rf} pump field. Resonances at/above the saturation field exhibit a smaller line-width than resonances elicited by non-homogenous magnetic textures.

probe the system with a fixed pump field h_{rf} parallel to the film while sweeping a perpendicular H_{dc} we obtain absorption spectra $\Delta|S_{12}|$ showcasing up to four resonance peaks at each fixed frequency (Fig. 5.1b).

Figure 5.1b shows the field dependence of $\Delta|S_{12}|$ for 14 different frequencies measured at 160K while sweeping H_{dc} from negative to positive magnetic saturation (in Fig. 5.1b we only show the absorption spectra from zero-field to magnetic saturation). At each frequency, the absorption peak occurring at the highest resonate field is the Kittel resonance peak [11, 12] arising from the precession of the homogeneous magnetization state of the film when the magnetic film is saturated. The absorption peaks observed at lower resonant fields are associated with non-homogenous magnetic states, *i.e.* stripe domains, bubbles and skyrmions. By fitting the Kittel peak with a Lorentzian profile we obtain the field dependence of the precession frequency (Fig. 5.2a). As expected from the Kittel formula [11,12], $f = \frac{\gamma_e}{2\pi}(H_{dc} - 4\pi M_{eff})$, where $4\pi M_{eff} = 4\pi M_S - H_k$ and M_S is the saturation magnetization and H_k is the perpendicular magnetic anisotropy field. The resonant field increases linearly with frequency and this linear behavior shifts to higher resonant fields as the temperature is decreased (Fig. 5.2a). Extrapolating the Kittel peak to $f = 0$ GHz gives the effective magnetization $4\pi M_{eff}$ (Fig. 5.2b). From the fact that $4\pi M_{eff}$ is positive we know the film possesses a weak perpendicular magnetic anisotropy which is less than the thin-film shape anisotropy and $4\pi M_{eff}$ becomes more positive as we decrease T. From M_S (Fig. 4.8) and $4\pi M_{eff}$ (Fig. 5.2b), we determine the effective perpendicular magnetic anisotropy K_{eff} as plotted in Fig. 5.2c decreases as we reduce the temperature (Fig. 5.2c). Also shown in Fig. 5.2c is the intrinsic anisotropy K_U which decreases with temperature as we have reported in Ref. [10] and shown in Chapter 4.9.

The Kittel resonance peaks line-width is typically small (ΔH~100 Oe) which suggests the effective Gilbert damping α is low. By fitting the line width, ΔH, as a function of the FMR frequency to $\Delta H = \frac{4\pi f \cdot \alpha}{\gamma_e} + \Delta H_o$, where ΔH_o is the inhomogeneous broadening and γ_e is the e^- gyromagnetic ratio, we find that the effective Gilbert damping α decreases monotonically from 0.0167 to 0.0078 with temperature (Fig. 5.2b). Compared to reported values for Gd-rich Fe-Gd ferrimagnets [13, 14], the α values are in good agreement.

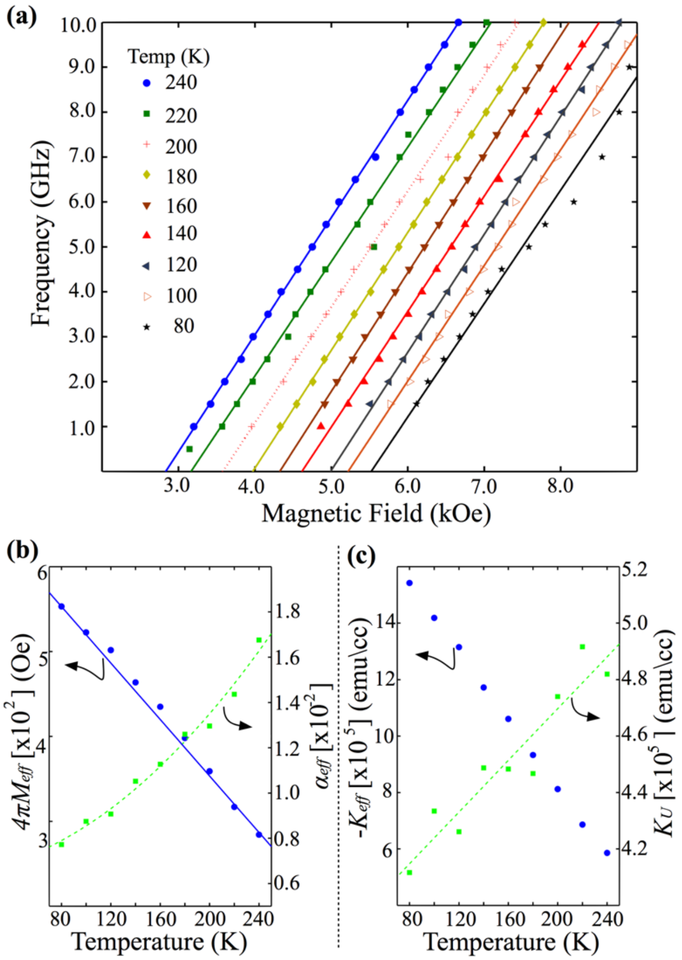

Figure 5.2 – Resonance and magnetic properties of [Fe (0.36nm) / Gd (0.4nm)]x80. (a) The field dependence of the resonance resulting from the precession of the homogenous magnetization, e.g. Kittel mode, is shown from 240K to 80K. **(b)** Fitting results from **(a)** and the line-width of the Kittel peaks, like those in Figure 1d, we determine the temperature dependence of the effective magnetization and effective damping. **(g)** The effective and uniaxial anisotropy are calculated from results in **(b)** and Figure 4.8.

From data like that shown in Fig. 5.1b measured from 240K to 80K, we have extracted all the resonant modes from the FMR spectra by fitting the peaks with Lorentzian profiles and plotted their normalized peak value intensity in frequency-field *f-H* phase diagrams in Fig. 5.3 and Fig 5.4. In Fig. 5.3 the field history was the same as that described for Fig. 5.1d, sweeping the field from negative saturation to positive saturation. In Fig. 5.4 the sample is first magnetically saturated in a positive field, then the magnetic field is reduced to zero-field before scanning the resonance spectra from zero-field to positive magnetic saturation. In both cases we measure the resonant spectra from remanence to positive saturation. For each resonance spectra, the intensity of each peak (normalized to the highest intensity peak at each fixed frequency) is given by the size of the symbol. We see that at each temperature there are two resonant mode regions. The first is above magnetic saturation and is described by the Kittel formula (as discussed above). The second region is below the saturation field where there are typically 2 or 3 mode branches that increase in frequency with decreasing field. In most cases, above $f = 2.5$ GHz the highest absorption peak is given by the uniform mode. However, at lower frequencies we observe very high-intensity modes resulting from the low-field magnetic textures.

Using magnetic phase maps from Fig. 4.2 we can overlay on the *f-H* diagrams the specific magnetic textures at each field and temperature. We have identified up to five different field regions: (I) disordered stripes, (II) coexisting stripes and skyrmions, (III) skyrmion lattice, (IV) disordered isolated skyrmions and (V) magnetic saturation and these magnetic states are shown on Fig. 5.3 and Fig. 5.4. At temperatures where no skyrmion phase is present, 240 K to 200 K (Fig. 5.3a-c, 5.4a-c), we observe the low-field mode branches decrease in frequency with increasing field and reach a minimum that correspond

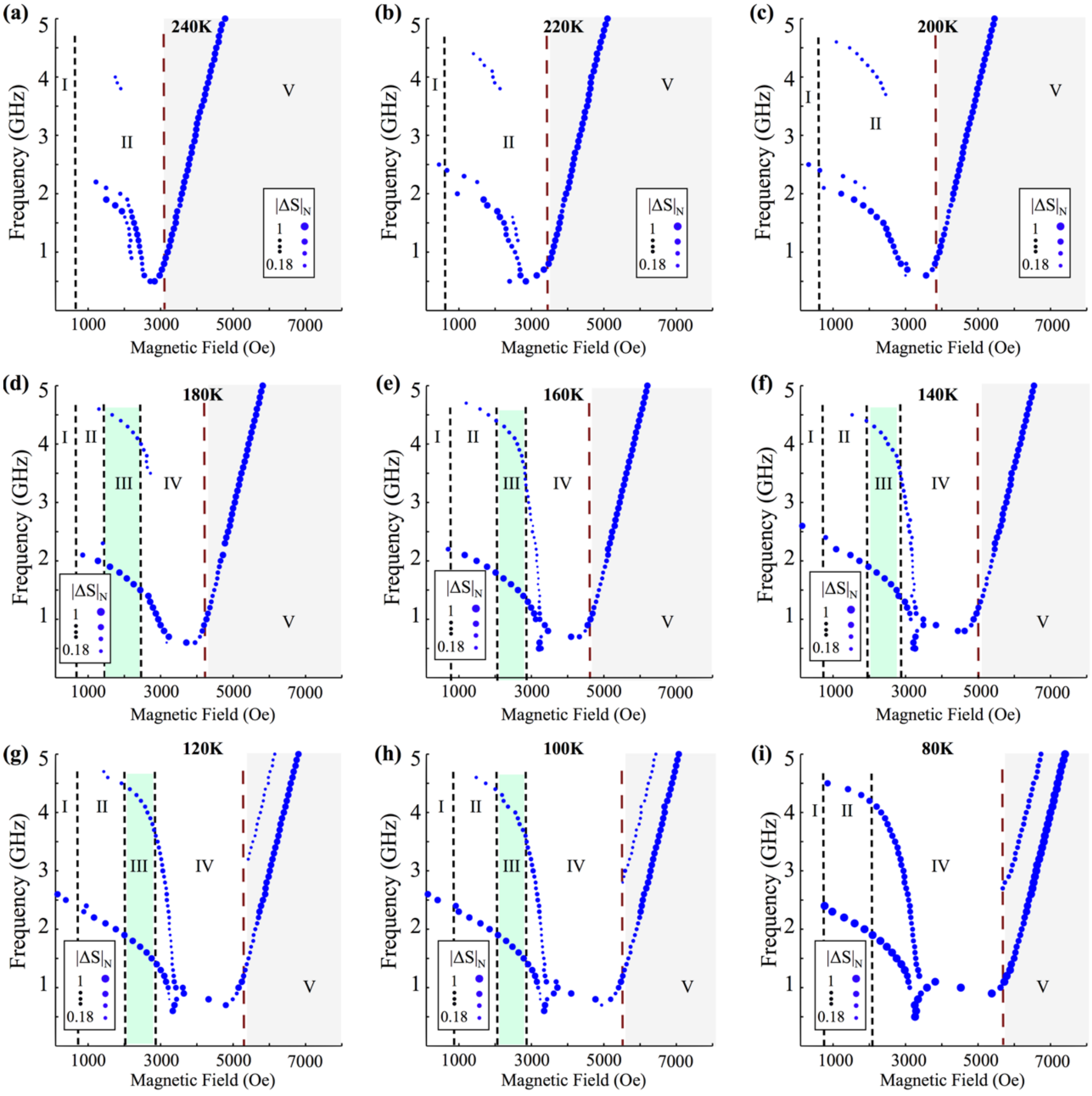

Figure 5.3 – Temperature dependence of the resonant modes of [Fe (0.36nm) / Gd (0.4nm)]x80. The frequency-field *f*-H dispersions illustrate the resonant modes that exist at temperatures ranging from 240K to 80K. These *f*-H dispersions were constructed from measurements were the perpendicular magnetic field is swept from H_z= -10 kOe to +10 kOe at each fixed frequency, and detail the resonances observed from zero-field to 8000 Oe. At each temperature, several regions are identified that correspond to specific domain morphologies: (I) stripes, (II) coexisting stripes and skyrmions, (III) skyrmion lattice, (IV) disordered skyrmions, and (V) Kittel region. The saturation field H_{sat} is obtained from magnetic hysteresis measurements performed in the same geometry.

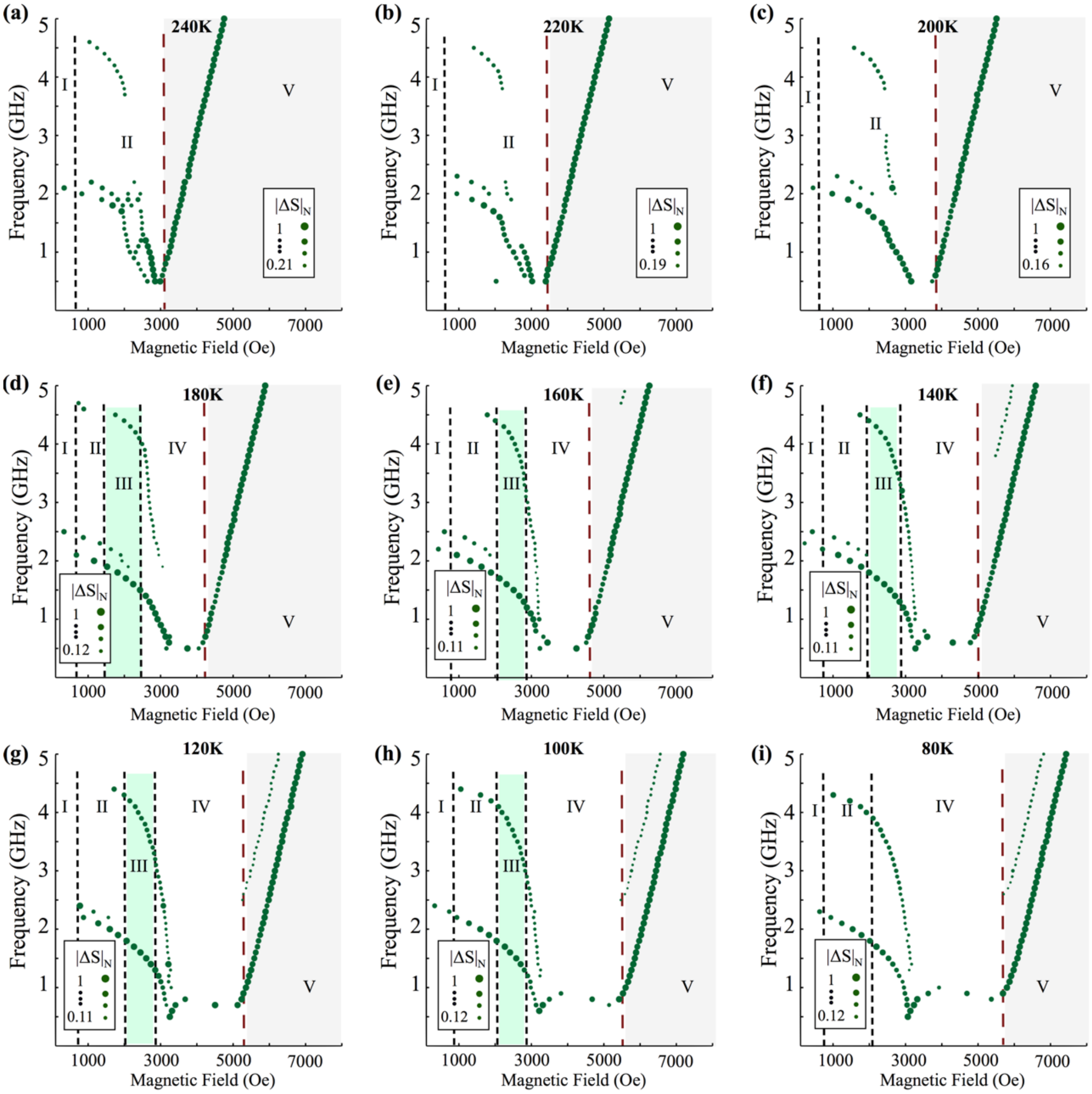

Figure 5.4 - Temperature dependence of the resonant modes of [Fe (0.36nm) / Gd (0.4nm)]x80 under a different field history. The frequency-field *f*-H dispersions from 240K to 80K were constructed from measurements were the perpendicular magnetic field is swept from H_z= 0 Oe to 10 kOe at each fixed frequency. At each temperature, several regions are identified that correspond to different magnetization states: (I) stripes, (II) coexisting stripes and skyrmions, (III) skyrmion lattice, (IV) disordered skyrmions, and (V) Kittel region. The saturation field H_{sat} is obtained from magnetic hysteresis measurements performed in the same geometry.

to the saturation field which can be estimated from extrapolating the linear Kittel peak in the high-field region. As we decrease the temperature we see the extrapolation of the low-field modes that branch to zero frequency occurs at lower magnetic fields than the saturation field. As the temperature is further reduced this gap increases. Here, the magnetic field at which the mode branches reach zero frequency does not change considerably with temperature and instead the gap increase is associated with the Kittel peak shifting to higher fields as the magnetization increases and the anisotropy decreases. Also we observe that there is no splitting of the low-field mode-branches at magnetic fields where the skyrmion phase is present in contrast to what is seen in materials where skyrmions are stabilized by DMI [4, 5]. Since skyrmions in Fe/Gd films are not a result of a field-driven phase transition from a helical to skyrmion phase, like in DMI materials, one might expect a continuous variation of the modes.

The low-field modes resulting from sweeping the magnetic field from negative saturation to positive saturation occurs in two branches, one branch below $f \sim 2.5$GHz and a second branch occurring around $f \sim 4.5$GHz that becomes more pronounced at lower temperatures. At higher temperatures the lower frequency branch shows two modes that becomes a single mode-branch with reduced temperature. From 180 K to 80 K, there are two mode branches resulting from the non-homogenous magnetic states that decline from $f \sim 4.5$GHz and 2.3GHz (Fig. 5.3d-i). In this temperature range, 180 K to 80 K, these two mode branches are fairly similar which suggests the domain morphology eliciting them is similar as well.

At low temperatures, 120K to 80K, we also observe a secondary mode-branch that appears above magnetic saturation (Fig. 5.3g-i). This mode occurs at lower resonant fields than the Kittel peaks and have much lower absorption intensity. The spacing in resonant field between the secondary mode branch and the Kittel mode branch is nearly parallel with the Kittel peak. Usually, a single resonance is expected above magnetic saturation, e.g. the Kittel resonance, yet variations in surface anisotropy in the thin film can result in the excitation of spin-wave resonances by either uniform or varying *r.f.* fields [15, 16].

In the case of the second field history, we find the resonant mode branches are similar to those elicited when the Fe/Gd specimen is scanned from negative to positive magnetic saturation, with the exception of an additional mode-branch appearing around $f \sim 2.5$ GHz at temperature spanning from 180 K to 120K (Fig. 5.4d-g). The presence of this additional mode-branch indicates a variation in the domain morphology as a result of the different field history. As the temperature is reduced from 180 K to 100 K we further observe that the mode-branch appearing at $f \sim 2.3$ GHz shifts upwards in frequency toward the mode-branch at $f \sim 2.5$ GHz until a single resonant branch is observable (Fig. 5.4d-h). Above magnetic saturation, we observe the presence of two mode-branches in a larger temperature range spanning from 160 K to 80 K (Fig. 5.4e-i). As before, the mode-branch occurring at the highest field corresponds to the Kittel peak and the lower intensity mode branch is potentially a spin-wave resonance [15, 16]. It is possible that the new field history results in spins pinning more weakly along the defects of the thin film, which is the reason we observe a second mode-branch appear above magnetic saturation at higher temperatures.

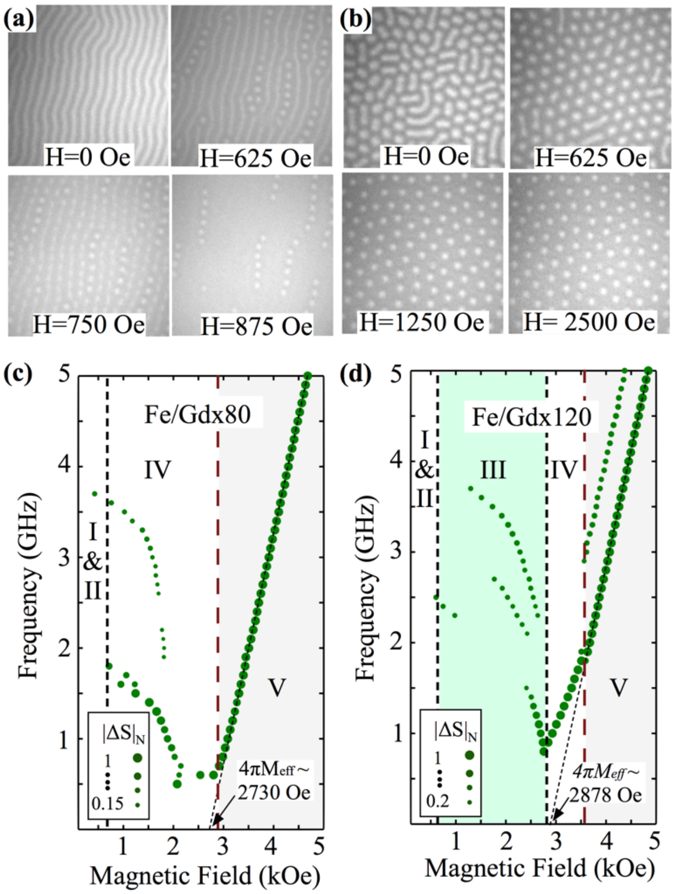

Figure 5.5 – Film thickness dependence of the resonant modes at room temperature. (a, b) Detail the domain morphology field evolution of [Fe (0.34nm) /Gd(0.41nm)]x80 and [Fe (0.34nm) /Gd(0.41nm)]x120 under positive perpendicular magnetic fields. The images are obtained with transmission X-ray microscopy along the Fe L_3 (708 eV) absorption edge, where white features depict magnetization ($-m_z$) and gray regions exhibit magnetization ($+m_z$). **(c, d)** The *f*-H dispersions for the latter Fe/Gd films show the field-varying resonant modes observed at room temperature. From images like **(a, b)** we correlate the modes to specific domain morphologies: (I) stripes, (II) coexisting stripes and skyrmions, (III) skyrmion lattice, (IV) disordered skyrmions and (V) Kittel region.

5.3 Thickness dependence of the resonant modes

We further studied the thickness dependence of the resonant modes in Fe/Gd multilayers that exhibits a close packing lattice of skyrmions at room temperature. Using full-field transmission soft X-ray microscopy, at the Fe L_3 (706 eV) absorption edge, we first investigated the field-dependent domain morphology of [Fe(0.34nm)/Gd(0.41nm)]xN with different bilayer N = 40, 80 and 120 repetitions. The latter two structures are the only ones that showcase perpendicular magnetic domains in this configuration, where [Fe(0.34nm)/Gd(0.41nm)]x80 depicts stripe domains that pinch into cylindrical domains (Fig. 5a) and [Fe(0.34nm)/Gd(0.41nm)]x120 shows disordered stripe domains that collapse into skyrmions which arrange into a close packing lattice (Fig. 5.5b).

When these domains states are probed with an in-plane *r.f.* pump field h_{rf}, we find the resulting *f-H* dispersions are qualitatively similar even though the domain morphologies are distinct (Fig. 5.5c, d). Above magnetic saturation, the comparable effective magnetization $4\pi M_{eff}$ suggests the films have the same average magnetic properties (Fig. 5.5c, d insert); hence, variations in domain morphology and resonant modes are a result of magnetostatic energy differences arising from different total film thickness. Comparing the *f-H* dispersions of [Fe(0.34nm)/Gd(0.4nm)]x80 and [Fe(0.34nm)/Gd(0.41nm)]x80, when a skyrmion phase is present (Fig. 5.3d-h, 5.5c), we find that both display almost identical resonant mode braches above and below magnetic saturation. The ordering of skyrmions, whether in a close-packing lattice or aligned skyrmions, is not reflected in the *f-H* dispersions. As the number of bilayer repetitions is increased, [Fe(0.34nm)/Gd(0.41nm)]x120, we observe the resonant mode branches shift closer to magnetic saturation and collapse near the saturation field (Fig. 5.5d). At and above magnetic saturation (Fig. 5.5c, d), the resonance frequency of [Fe(0.34nm)/Gd(0.41nm)]x80 and [Fe(0.34nm)/Gd(0.41nm)]x120 linearly increase with field as expected for the uniform magnetization.

5.4 Micromagnetic modeling

To determine the micromagnetic nature of the modes observed, we performed numerical simulations of the Landau-Lifshitz-Gilbert (LLG) equation under time-dependent *a.c.* magnetic fields, utilizing the FASTMag solver [17]. We use the magnetic parameters where a skyrmion lattice forms numerically (from Ref. [10]: $M_S = 400$ emu/cm^3, $K_U = 4\text{x}10^5$ erg/cm^3 and $A = 5\text{x}10^{-7}$ erg/cm) which are consistent with the magnetic properties of [Fe(0.36nm)/Gd(0.4nm)]x80.

5.4.1 Domain states, susceptibility and resonant modes

First, we explored the field-dependent equilibrium states that form in a slab with volume of 2μm x 2μm x 80nm that is discretized with 10-nm tetrahedra. The simulation is first saturated with a perpendicular magnetic field and then the field is reduced to $H_z = 0$ Oe and allowed to reach equilibrium in 30 ns. Then the perpendicular magnetic field is increased from $H_z = 0$ Oe to 4000 Oe in discrete steps and the slab is allowed to reach an equilibrium state in 30 ns. The field history is similar to the experimental protocol used for the results in Fig. 5.4. After reducing to zero field we find the remanent state consists of stripe domains with random in-plane order (Fig. 5.6a) that is similar to experimental observations (Fig. 4.1). Inspecting a cross-section of the slab, across the thickness, reveals a domain morphology consisting of perpendicular domains with domain walls that are Bloch-like in the center of film and become more Néel-like towards each surface forming closure domains. Given the transmission geometry nature of the experimental imaging

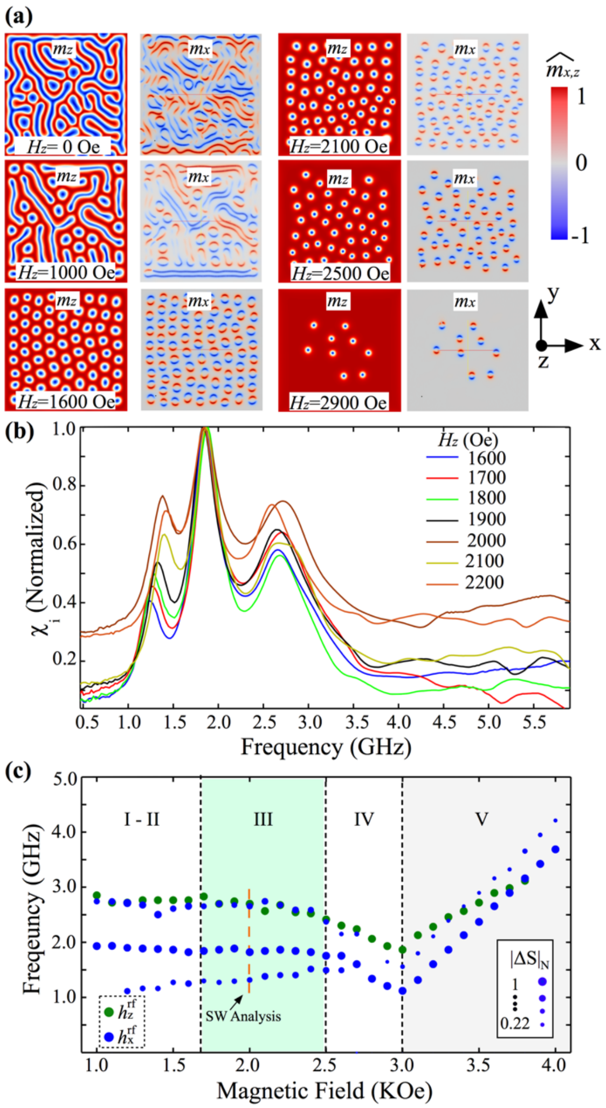

Figure 5.6 – Domain morphology and susceptibility. (a) The field dependent domain morphology at H_z = 0 Oe, 1200 Oe, 1600 Oe, 2500 Oe and 2900 Oe showcase the evolution of disordered stripe domains to ordered skyrmions to disordered skyrmions (m_z at z = 40nm, top side view). The in-plane magnetization along the center of the slab reveals the helicity of these textures (m_x at z = 0nm, top side view). The magnetization distribution (m_x, m_z) of these equilibrium states is based on the red/blue color-bar. **(b)** The numerically computed susceptibility that results from whole slab at several fixed H_z fields is detailed. **(c)** Fitting the resonance spectra with n-Lorenztian peaks allows us to construct frequency-field *f*-H dispersions. The marker size corresponds to the normalized intensity of the susceptibility at each fixed H_z field and the marker color distinguishes the resonance spectra from either exciting the equilibrium states with an *r.f.* field h_{rf} along the x-axis or the z-axis. Using the equilibrium states, as those in **(a)**, we correlate resonant modes to specific domain textures: (I-II) stripes and coexisting stripes and skyrmions, (III) skyrmion lattice, (IV) disordered skyrmions and (V) Kittel region.

techniques used and the symmetry of the Néel caps, this will require a 3-dimensional imaging of domain walls [18]. As a perpendicular field is applied, the stripe domains begin to collapse into an equal population of skyrmions with two possible helicities S = 1, $\gamma = \pm\pi/2$ (Fig. 5.6). Increasing the field further, the skyrmions arrange into a close packing lattice that spans from $H_z = 1600$ to 2400 Oe (Fig. 5.6). After $H_z = 2400$ Oe, the skyrmions become disordered and begin to collapse as the field is increased to magnetic saturation. Overall the field-dependent domain morphologies are in good agreement with our experimental observations [10].

To determine the dynamic response, we perturbed the magnetization states with a pulse field along the x-axis or z-axis, with an amplitude of $h_x = h_z = 100$ Oe, that results in a susceptibility spectrum (Fig 5.6b). To obtain the susceptibility $\chi(\omega)$, the dynamics of the magnetization in time-domain are recorded when exposed to the pulse field. Afterwards, both the excitation field and the magnetization response are Fourier transformed using fast Fourier transform (FFT) approach. It follows that the susceptibility in frequency domain is given by:

$$\chi(\omega) = \frac{M(\omega)}{H(\omega)} = \chi'(\omega) + i\chi''(\omega) \tag{5.1}$$

where ω is the frequency, $M(\omega)$ magnetization and $H(\omega)$ field pulse in frequency domain; furthermore, $\chi'(\omega)$ is the real part of $\chi(\omega)$ that reflects the sensitivity of the magnetization under a field and $\chi''(\omega)$ is the imaginary part of $\chi(\omega)$ that reflects the dissipation of energy being absorbed. By fitting the various $\chi''(\omega)$ resonant peaks with Lorentzian profiles from both perturbation geometries, we obtain a *f-H* dispersion with up

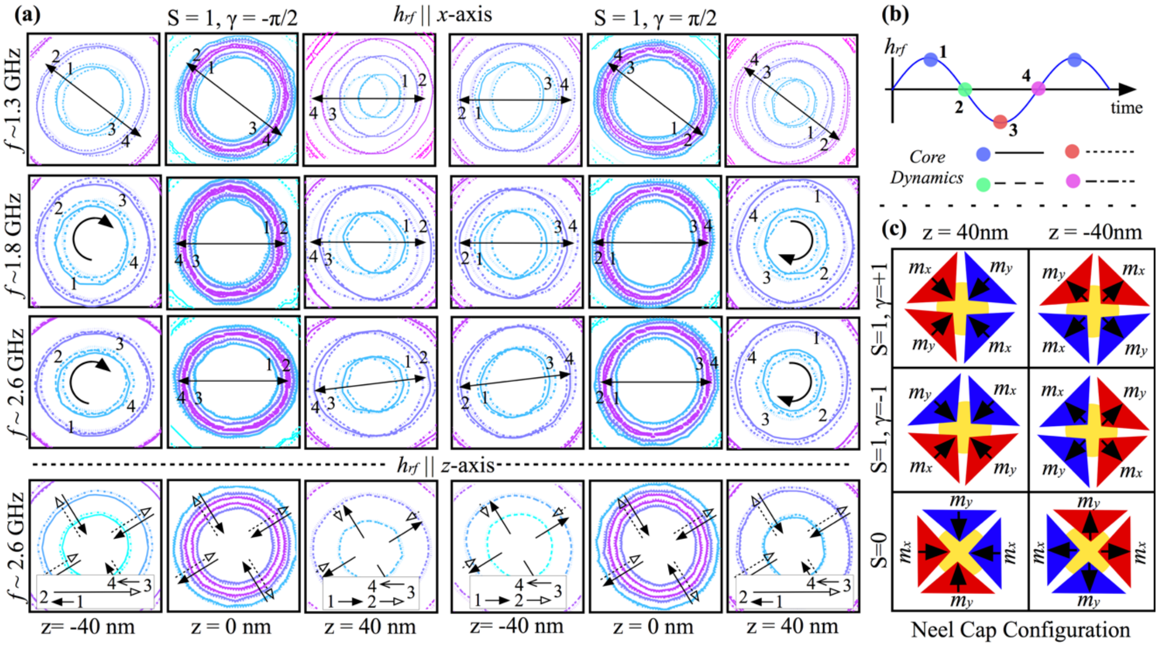

Figure 5.7 – Skyrmion spin-wave modes. (a) The skyrmion spin wave dynamics observed from perturbing the skyrmion phase, at H_z= 2000 Oe, along both x-axis and z-axis geometries are detailed for both skyrmion helicities. Using contour plots, the motion of the skyrmion is traced along three different depths positions (z = -40 nm, 0 nm, 40 nm) for each resonant mode. Different contour lines depict position of the skyrmion with reference of the sinusoidal pulse field **(b)** and arrows are used as guide for the eye to describe the motion of the spin-wave. **(c)** Illustrates a cartoon of the Néel cap configuration of m_x and m_y around a skyrmion (S = 1) and bubble (S = 0) at the top and bottom of the slab. Further details on this Néel cap configuration are detailed in the Chapter 5.4.5.

to three mode branches appearing in the non-homogeneous magnetization region that are similar in frequency to the lower frequency mode branch observed experimentally and two mode branches in the saturated state (Fig 5.6c). The non-Kittel modes appearing above magnetic saturation are explored further in Chapter 5.4.7. In order to resolve what dynamic magnetization configurations appear in the mode-branch, of the susceptibility spectra detailed, we apply a sinusoidal *a.c.* magnetic field and record snapshots of the magnetic domain evolution during a sinusoidal field cycle [6] (Fig. 5.7b). Our modeling suggests a variety of localized spin wave modes exist that give rise to the observed mode-branch and depends on the helicity of the skyrmions (Fig. 5.7a).

Here we describe the spin wave configurations resulting from an in-plane sinusoidal field h^{rf}_x at resonant frequencies: $f \sim 1.3$ GHz, 1.8 GHz, 2.6 GHz at $H_z = 2000$ Oe (Figs. 5.6c, 5.7a) which depicts the dynamics of a skyrmion lattice that forms at this field. At each resonant frequency the entire magnetic feature resonates with the following properties: (i) the localized spin-wave is asymmetrical on the top and bottom of the skyrmion domain and (ii) a skyrmion with opposite helicity shows the inverse spin-wave mode. To show this complex spin-wave behavior, we detail the displacement of the magnetic texture using contour lines at different quadrant positions for a single sinusoidal pulse (Fig. 5.7b). Figure 5.7a shows the spin-wave motion of the out-of-plane magnetization at three different depth positions of the slab (top surface, center and bottom surface) for both helicity skyrmions ($S = 1, \gamma = \pm\pi/2$). Given the symmetry of the spin-wave mode response for skyrmions with opposite helicity, we describe in detail only the behavior for an ($S = 1, \gamma = -\pi/2$) skyrmion. First, the localized spin-wave associated with the $f \sim 1.3$ GHz branch consists of a linear displacement of the skyrmion top from right-to-left-to-right position during a sinusoidal pulse cycle. Given the back and forth displacement during the pulse field cycle, we refer to it as localized 'linear' spin-wave mode. The skyrmion bottom exhibits a linear displacement from right-to-left-to-right that is rotated by ~135°. In the case of the $f \sim 1.8$ GHz spin-wave, a similar linear displacement, from right-to-left-to-right, is observed on the top of the skyrmion, however, the bottom part of the skyrmion rotates in clock-wise motion. Last, the $f \sim 2.6$GHz spin-wave displacement is similar to that of the $f \sim 1.8$ GHz mode with the exception that the linear displacement occurs at a small tilted angle away from the perturbation field along the x-axis. From inspecting the spin-wave motion for all three mode-branches, we find that greater displacement is towards the surface of the slab which is the region where the Néel caps have a larger presence.

The spin-wave mode associated with a perturbation along the z-axis, consists of a breathing-like displacement where the skyrmion expands and contracts under the sinusoidal field. This spin-wave mode is similar to that reported by Mochizuki, *et al.* [Ref. 6] in DMI skyrmion materials. Here, the skyrmion domain expands/contracts non-uniformly throughout the thickness of the slab: for an ($S = 1$, $\gamma = -\pi/2$) skyrmion, the core contracts and expands at the top of the slab; whereas at the bottom, the core expands and then contracts. The inverse dynamics is also observed for a skyrmion with opposite helicity. Altogether, the breathing displacement for a skyrmion is weaker than the motion resulting from perturbing the same equilibrium state with a sinusoidal field $h^{rf}{}_{\mathrm{x}}$ pulse. In the case of the Néel caps, we also observe a breathing-like displacement that also twists from right-to-left around the skyrmion.

A closer inspection of the Néel cap configuration throughout the film thickness, reveals the in-plane magnetization components, m_x and m_y, have a twist of ~90° from bottom to top for both helicity skyrmions (Fig. 5.7c, 5.11). In the case of an ($S = 1$, $\gamma = -\pi/2$) skyrmion the twist from top to bottom is of ~ +90°, whereas, an ($S = 1$, $\gamma = \pi/2$) skyrmion has a twist of ~ -90°. Typically, a Bloch-like domain structure distribution consists of Néel caps with mirror image planes from the bottom to top of the film (Fig. 5.7c, 5.11). This twisted arrangement of the Néel caps is only observed in the skyrmion domain states and does not occur in bubble domains, e.g. $S = 0$ (Fig. 5.7c, 5.11).

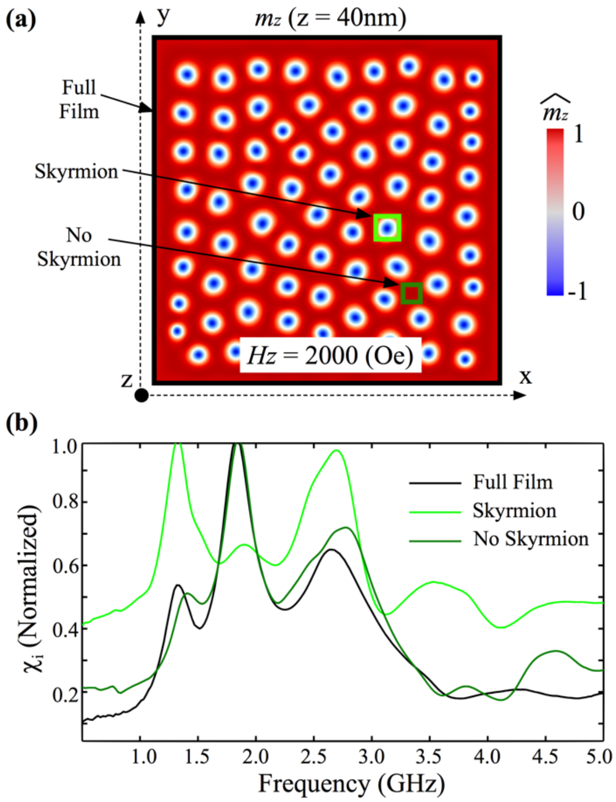

Figure 5.8 – Localized susceptibility. The susceptibility contribution of specific regions of the skyrmion phase stabilized at H_z= 2000 Oe are compared to investigate the source of the resonance spectra. The analyzed areas are shown on the top-side view of the domain morphology with contributions along m_z (a) and m_x (b). The regions highlight a single skyrmion, no skyrmion domain and the resonance spectra is compared to that of the whole film. (c) The complex susceptibility (χ_i) reveals the three different areas resonate at the same frequency with variations in absorption intensity.

5.4.2 Localized susceptibility

To further probe the spin-waves, we performed localized susceptibility modeling on the skyrmion lattice phase when H_z = 2000 Oe, by analyzing local volume regions that either contains a single skyrmion or an area between skyrmions as shown in Fig. 5.8a and then compared it to the susceptibility averaged over the whole slab (Fig. 5.8a). The regions examined result in similar resonance spectra with some differences in normalized peak amplitude (Fig. 5.8b) – the skyrmion domain showcases stronger fluctuations at resonances occurring at *f* ~ 1.3 GHz and 2.6 GHz, in contrast, a region without a skyrmion resonates strongest at *f* ~ 1.8 GHz. Overall the localized susceptibility indicates the whole slab containing the non-homogenous magnetic textures resonates at the same frequencies and no single magnetic features drives the skyrmion localized skin-wave modes.

5.4.3 Effects on susceptibility resulting from exchange length variations

As we have detailed in Chapter 4.10 and 4.11, the exchange coupling *A* plays an important role in the skyrmion long range order, as well as, the size of the skyrmion, volume fraction of perpendicular domain and Néel caps, etc. To investigate how variations of exchange length *A* affect the skyrmion resonant properties, we varied the *A* strength from 4 to 6x10^{-7} erg/cm, fixing M_S = 400 emu/cm^3 and K_U = 4x10^5 erg/cm^3, and modeled the susceptibility from resulting from the equilibrium states at H_z= 2000 Oe (Fig. 5.9a). All these exchange coupling values result in an ordered skyrmion phase (Fig. 5.9b-d) with resonances appearing at *f* ~ 1.3GHz, 1.8G Hz and 2.6 GHz. As the exchange coupling is increased the absorption intensity solely varies at resonances elicited at *f*~ 1.3 GHz and 2.6 GHz, which we know are related to the skyrmion domain (Fig. 5.8). Interestingly, these resonate at different maximum/minima intensities depending on the exchange coupling strength. In the case of *A* = 6x10^{-7} erg/cm, the two primary resonances appear at *f* ~ 1.8 GHz and 2.6 GHz; whereas, for *A* = 4x10^{-7} erg/cm the primary resonances appear at *f* ~

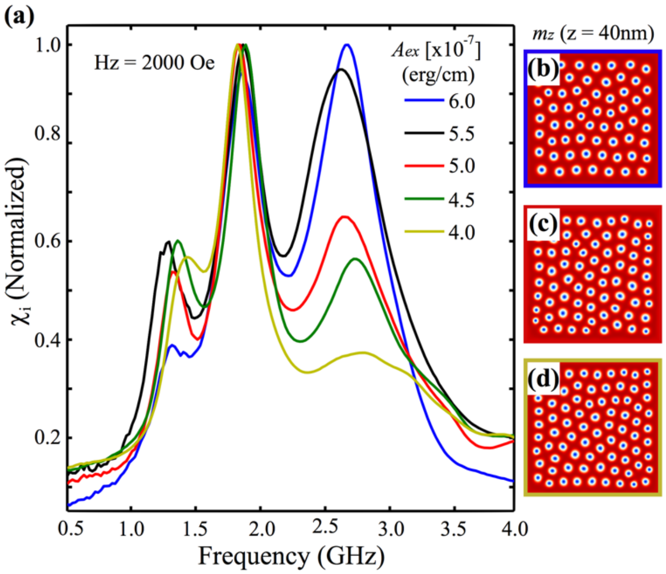

Figure 5.9 – Effects of different exchange length on susceptibility.(a) The susceptibility for different exchange A strength is computed for a fixed field $H_z = 2000$ Oe. The top-side magnetization states detail m_z at the top of the slab (z = 40 nm) under $H_z = 2000$ Oe for different exchange: **(b)** $A = 6\text{x}10^{-7}$ erg/cm, **(c)** $A = 5\text{x}10^{-7}$ erg/cm and **(d)** $A = 4\text{x}10^{-7}$ erg/cm.

1.3 GHz and 1.8 GHz. This evidence suggests that our inability to experimentally detect the mode-branch appearing around *f* ~ 1.3 GHz in the Fe/Gd films is likely a result of either: (i) the exchange coupling is higher than numerically assumed or (ii) the intensity absorption at this resonance is weak enough that we are unable to discern it.

5.4.4 Susceptibility and resonant modes from domains states under small bias in-plane magnetic field

The numerical modelling accurately replicates the lower frequency mode-branches from the *f-H* dispersions detailed for [Fe(0.36nm)/Gd(0.4nm)]x80, where a skyrmion phase is present. It does not reproduce the experimental mode branch occurring at *f* ~ 4.4 GHz.

For this reason, we also considered modeling the response of a domain morphology consisting of a combination of bubbles and skyrmions because it is possible to experimentally stabilize both textures in amorphous Fe/Gd multilayers [17,18]. We achieve this by applying a constant small in-plane field along the x-direction with an amplitude of H_x = 60 Oe while a perpendicular magnetic field is varied. We find that disordered stripe domains become ordered and align transverse to the H_x field at H_z = 0 Oe (Fig. 5.10a). Examining the in-plane magnetization at the top and the center of the slab reveals the Néel caps align in the direction of the constant H_x field, which results in the Bloch-line pointing orthogonal to the fixed H_x in-plane field (Fig. 5.10a, 5.12). The ordering of the Néel caps and Bloch-line under an in-plane field is described further in Chapter 5.4.5 and 5.4.6.

Subsequently, as perpendicular field is applied while keeping the in-plane field constant, the stripe domains begin to collapse into cylindrical-like domains (Fig. 5.10a). Unlike in the results shown in Fig. 5.6 where a majority of the magnetic features are skyrmions we observe that the application of an in-plane field results primarily in the formation of bubble domains (S = 0) and some skyrmions which all arrange into a close-packing lattice that exists from H_z = 1600 Oe to H_z = 2400 Oe. We observe the Bloch-line for the bubbles aligns in the direction of the in-plane H_x field as opposed to circling the domain as seen in the skyrmion phase. As the perpendicular field is increased further, the bubbles and skyrmions become disordered and these textures begin to dissipate toward magnetic saturation with bubbles collapsing at lower fields than skyrmions (Fig. 5.10a). Given the topological nature of skyrmions, a higher annihilation field is required compared to bubbles. Experimentally we observed that with in-plane fields can also result in bound skyrmion pairs of opposite chirality [9].

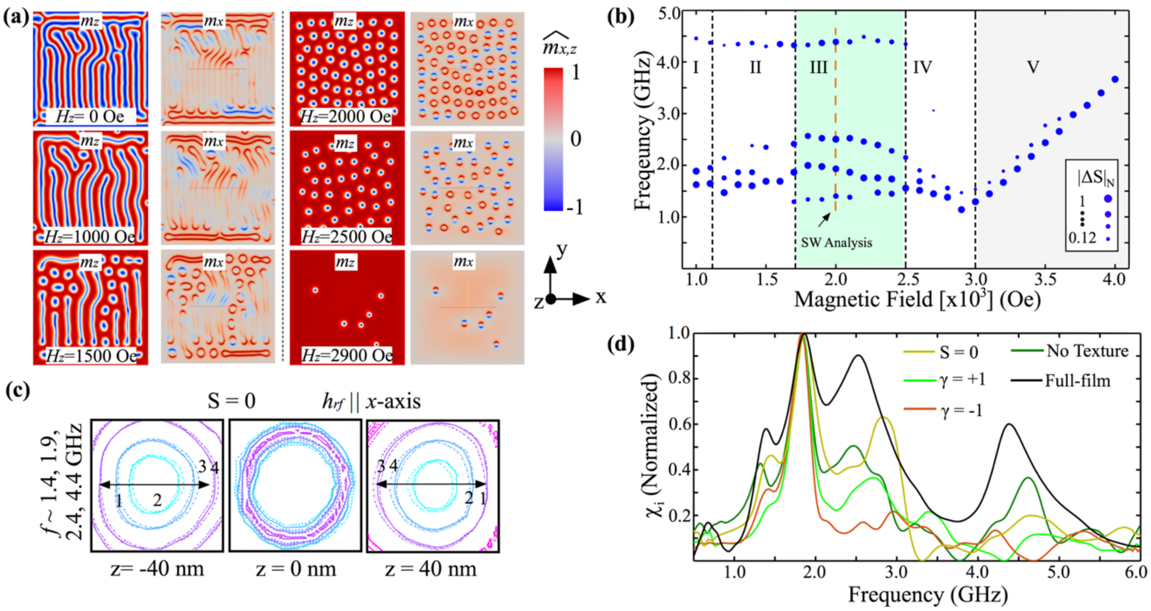

Figure 5.10 - Resonance properties from mixture of bubbles and skyrmions. (a) The perpendicular field-dependence of equilibrium states with a constant H_x field show the evolution of aligned stripes to cylindrical domains (topside, z=40nm, m_z). The cross-section across the center of the slab (z=0nm) shows magnetic texture have a mixture of Bloch-line ordering (top side, m_x). **(b)** The computed susceptibility spectra for magnetization states like those in **(a)** result in four mode-branches below magnetic saturation and two-mode branches above magnetic saturation. The magnetization states observed include: (I) stripes, (II) coexisting stripes and cylindrical domains, (III) ordered lattice of cylindrical domains, (IV) disordered cylindrical domains and (V) Kittel region. **(c)** The spin-wave dynamics associated with a bubble domain when probed under an in-plane sinusoidal pulse field. **(d)** Localized susceptibility resulting from the various textures observed at H_z = 2000 Oe.

Applying the same a.c. field perturbations, as described before, results in a comparable susceptibility spectrum like the one elicited from equilibrium states without a constant in-plane field (Fig. 5.6c) together with an additional mode branch appearing at f ~ 4.4 GHz (Fig. 5.10b). In the f-H diagram, we overlay the different magnetic textures that form under a magnetic field based on results like those in Fig. 5.10a. The magnetization states include: (I) stripes, (II) coexisting stripes and cylindrical domains, (III) ordered lattice of cylindrical domains, (IV) disordered cylindrical domains and a (V) Kittel region. We find the mode-branch at $f \sim 4.4$ GHz is fairly constant with increasing field even as the magnetic textures change from stripes to an ordered lattice of cylindrical domains and decays sharply in resonant frequency and intensity when the slab exhibits disordered cylindrical domains.

When exposing the magnetic configurations that form at $H_z = 2000$ Oe to a sinusoidal a.c. field along either $h^{rf}{}_{\mathrm{x}}$ or $h^{rf}{}_{\mathrm{z}}$ at one of the resonant frequencies ($f \sim 1.4$ GHz, 1.9 GHz, 2.4 GHz and 4.4 GHz) we can determine the spin-wave configurations that appear for both chirality cylindrical domains. The skyrmions (S = 1, $\gamma = \pm \pi/2$) exhibit the equivalent localized spin-wave modes previously described at similar resonant frequency. In contrast the bubble domains (S = 0) exhibit the same localized spin wave dynamics at all of the four resonant frequencies. The bubble domains exhibit a linear displacement of the core in the direction of the oscillating field $h^{rf}{}_{\mathrm{x}}$ pulse (Fig. 5.10c). The top of the bubble shifts from left-to-right-to-left, whereas at the bottom, the motion is from right-to-left-to-right. Probing the textures with a perpendicular sinusoidal a.c. field $h^{rf}{}_{\mathrm{z}}$ results in a similar breathing-like spin wave excitation for both bubbles and skyrmions, as detailed before. The difference in dynamics between bubble domains and skyrmions is attributed to the ordering of the Néel caps and Bloch-line around the perpendicular cylindrical domain. Bubbles, unlike skyrmions, exhibit Néel caps with mirror symmetry planes at the top and bottom of the cylindrical domain (Fig. 5.7c, 5.11). Furthermore, the alignment of the closure domains and Bloch-line in the direction of the in-plane H_x field is anticipated to result in a linear displacement of the bubble domain core.

Localized susceptibility measurements from each class of texture present at H_z = 2000 Oe reveals the resonant mode-branch at *f* ~ 4.4 GHz primarily results from fluctuations of domains with magnetization in the direction of the +H_z field and also bubble domains (Fig. 5.10e). Since the susceptibility spectrum is the average response of all non-homogenous magnetic textures, it follows that magnetic domains that occupy a larger presence at any magnetic field will incur in a more prominent signal. The experimental observation of the mode-branch at *f* ~ 4.4 GHz suggests the formation of bubble domains in the Fe/Gd films which could be attributed to different mechanisms, such as: (*i*) the in-plane field produced by the coplanar waveguide is sufficient to orient the Bloch-line of the magnetic domains as the field is reduced from magnetic saturation, (*ii*) alternatively a tilt of the sample with respect to the coplanar waveguide could similarly result in the application of an additional in-plane field to the magnetic specimen. All of these scenarios are possible given the Fe/Gd film has soft magnetic properties (Fig. 4.8). As a result, the *f*-*H* dispersions detailed in Figs. 5.3, 5.4 and 5.5 are predicted to detail the resonance behavior of a mixture of magnetic bubbles and dipole skyrmions.

5.4.5 Néel cap configuration for cylindrical domains with different helicity

The domain morphology across the thickness of the slab for cylindrical domains with different chirality is detailed (Fig. 5.11). Both dipole skyrmions (S = 1, $\gamma = \pm\,\pi/2$) and bubbles (S = 0) show similar perpendicular magnetization (m_z) distribution; however, the lateral magnetization (m_x, m_y) varies throughout the thickness of the slab for all the textures.

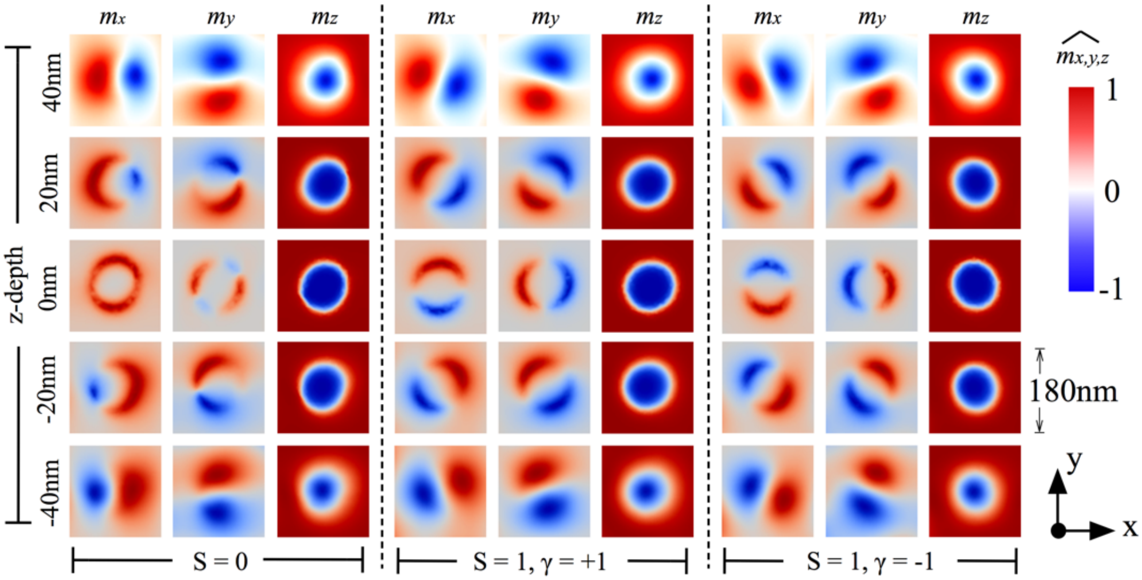

Figure 5.11 – Cylindrical domain in-plane magnetization. The domain morphology of cylindrical domains with different winding number (S = 0, 1) are explored at different depths of the slab and magnetization (m_x, m_y, m_z) orientations. Each equilibrium state depicts the top-side view of 180nm^2 area.

Differences are observed in the Bloch-line arrangement (center of the slab) and the Néel cap configuration (away from the center of the slab). In the case of bubbles, we see the Bloch-line aligns in the direction of the applied in-plane field. We recall, that the observation of bubbles in these films results from perturbing the equilibrium states with a constant in-plane field along the x-direction, with a magnitude H_x = 60 Oe, while a perpendicular field H_z is applied. Effects of the in-plane field on the domain morphology is detailed in Chapter 5.4.6. In contrast, skyrmions (S = 1, γ = ± π/2) have random chiral Bloch-line order which is set by the minimization of the energetics in the system.

The most distinct difference is observed in the Néel cap configuration surrounding the cylindrical domain. For bubbles (S = 0), the Néel caps orientation along both m_x and

m_y are mirror images around the center of the slab. This is the common configuration expected for film with a Bloch domain structure. For skyrmions ($S = 1, \gamma = \pm \pi/2$), the Néel cap arrangement depends on the chirality and the mirror images of both m_x and m_y are winded by ±90 degrees from the top to the bottom of the slab. This chiral Néel cap is what gives dipolar field driven skyrmions their topological protection.

5.4.6 Bloch-line configuration under an in-plane field

To understand the arrangement of the Bloch-line under an external in-plane field, we evaluated the domain morphology that results from different ratios of anisotropy K_U and magneto-static energy $2\pi M_S^2$, which is defined as the material Q-factor. It follows that thin films with Q-factor < 1 will prefer to have the magnetization lying on the plane of film; whereas, magnetic specimens with Q-factor > 1 will have the magnetization aligned perpendicular to film. However, in the case of relatively thick films with material Q-factor < 1, the minimization of anisotropy and magneto-static energy can favor a domain structure consisting of perpendicular magnetic domains and closure domains, e.g. Néel caps. As detailed in Chapter 4, our observation of perpendicular domains in these Fe\Gd films is a result of the latter circumstance.

Our sampling of magnetization states with varying Q-factor (~0.1 to 1) allows us to capture domains structures with different ratios of perpendicular domains and Néel caps (Fig. 5.12). At zero-field, we find that magnetization states with $K_U \leq 3\text{x}10^5$ erg/cm^3 favor a vortex domain state given the area restrictions of the slab, i.e. the magnetization would be in-plane for a continuous thin film; whereas equilibrium states with $K_U > 3\text{x}10^5$ erg/cm^3

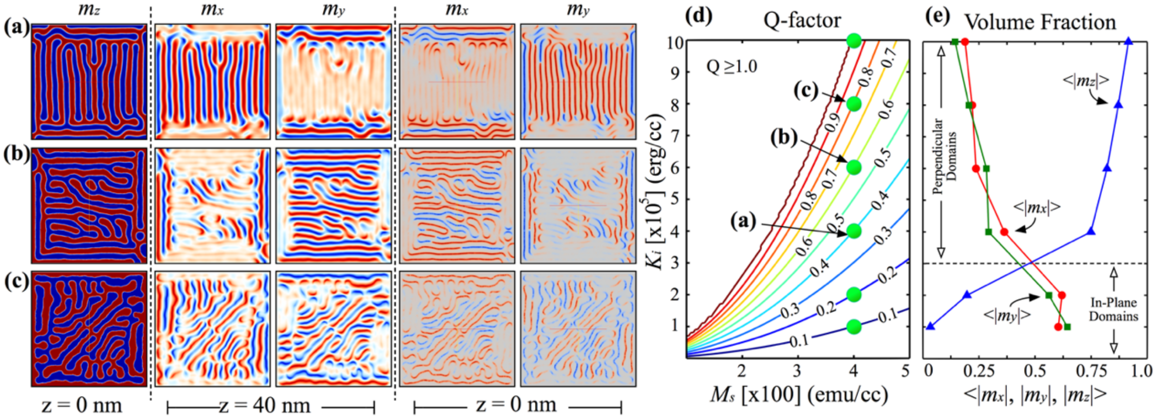

Figure 5.12 – Ordering of stripes domains under in-plane field. The rearrangement of equilibrium states with different Q-factor ratios under an external in-plane field, along the x-axis, are detailed. **(a-c)** The top side view ordering of m_x and m_y at the top (z = 40nm) and center (z = 0nm) of the slab reveals the rearrangement of the Néel caps and Bloch-line. **(e)** The magnetization volume fraction <|$m_{x,\,y,\,z}$|> for the equilibrium states in **(d)** show that perpendicular magnetic domains with Néel caps become favorable when <|m_z|> is greater than <|$m_{x,\,y}$|>. In this regime, as the Q-factor increases the volume fraction of the in-plane domains decreases, whereas, perpendicular domains become more prevalent in the domain morphology.

favor perpendicular disordered stripe magnetic domains. When these magnetization states are exposed to an in-plane field along the x-direction, with a magnitude of H_x = 60 Oe, the following broad observations can be made:

i. K_U = 4x10^5 erg/cm^3 – The majority of Néel caps align in the direction of the in-plane field H_x (m_x, z = 40 nm) and the Bloch-line of most stripe domains points orthogonal to the H_x field (m_y, z = 0 nm).

ii. K_U = 6x10^5 erg/cm^3 – The Bloch-line of most stripe domains align in the direction of the in-plane field (m_x, z = 0nm) and the Néel caps are orthogonal to the H_x field (m_x, z = 40nm).

iii. $K_U \geq$ 8x10^5 erg/cm^3 – The in-plane field H_x is insufficient to align a specific lateral magnetization component across the film. At the top of the slab, the Néel caps have magnetization randomly distributed along both m_x and m_y (z = 40nm); similar observations can be reached for the Bloch-line across the center of the slab (z = 0nm).

In all the cases above, we observe a transverse alignment of the Bloch-line and Néel caps because these structures have a helical arrangement across the thickness of the slab. Depending on the volume fraction of the in-plane magnetic domains, we observe distinct structures align differently with the in-plane field (Fig. 5.12e). As the volume fraction of the domain wall (Néel caps and Bloch-line) decreases, we find the in-plane field H_x is unable to reorder the domain state. Altogether, it appears that a specific ratio between $<|m_{x,y}|>$ and $<|m_z|>$ is required to favor the of the alignment of the Néel caps or the Bloch-line with an external field.

From these simulations, we can infer that the presence of an in-plane can result in helicity changes for domain states at the ground state. Effects on the chirality of the domains at zero-field will affect the perpendicular magnetic domains that form under an out-of-plane magnetic field. In our case, bubbles result from aligning the stripes at the ground state (Fig. 5.10).

5.4.7 Spin wave resonance above magnetic saturation

Using micromagnetic simulations, we explored the magnetization dynamics that result in the second mode branch appearing above magnetic saturation in the numerically computed susceptibility (Fig. 5.6c). We apply a sinusoidal field pulse along the x-direction to a magnetization state that is uniformly magnetized in the direction of the perpendicular

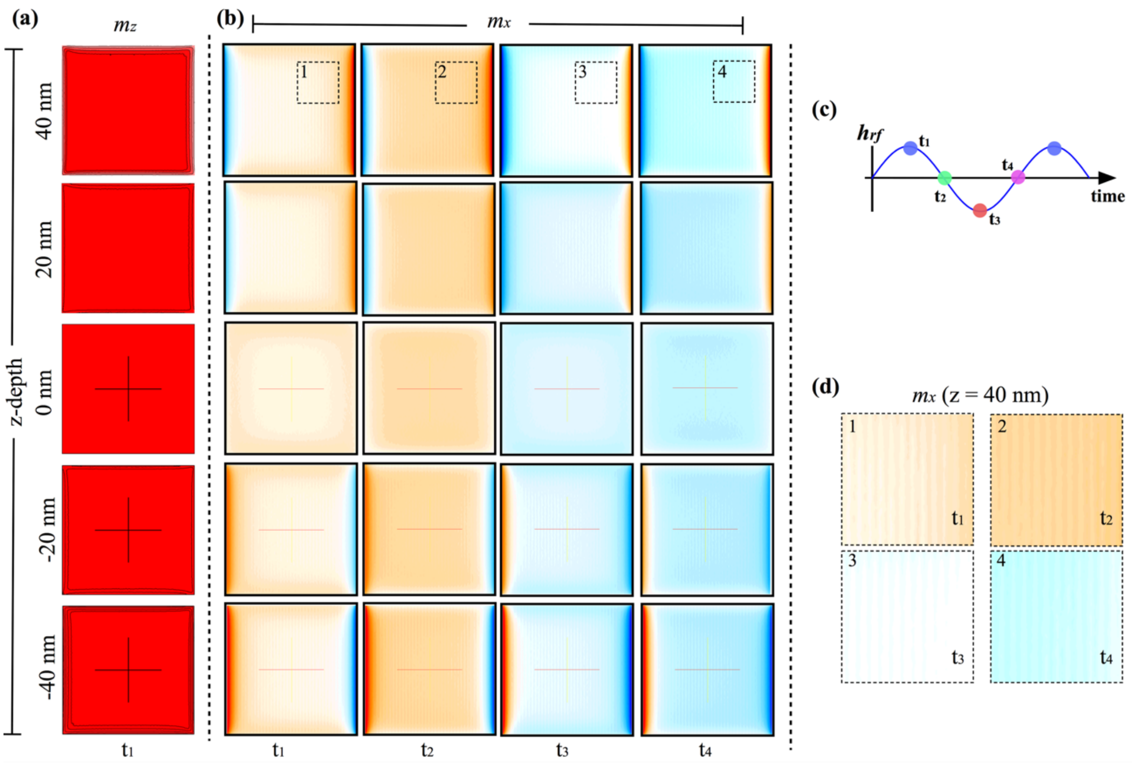

Figure 5.13 – Spin wave arising from slab edge. (a, b) The top-side magnetic distribution of M_x and M_z are detailed as a function of slab thickness and evolution in time when perturbed with a small oscillating h_{rf} in-plane field. **(c)** The h_{rf} field is applied along the x-direction, where several snapshots at different time intervals are collected. Here we detail four snapshots (t_1, t_2, t_3, t_4) that show a spin wave moving through the thickness of the slab. The cross at the center of the ES is an artifact from the visualization software. **(d)** Enlarged regions from time distributions along m_x show a moving spin wave.

field ($+H_z$) and exhibits a secondary resonant mode at $H_z = 3500$ Oe with resonance at $f \sim 2.89$ GHz (Fig. 5.6c). Inspecting the dynamics across the slab reveals a spin wave originates from the edge of the slab and moves across the thickness of the slab in the direction of the field perturbation (Fig. 5.13a). The magnetization state at time interval t_1 shows m_z at different depths of the slab (z = 40 nm, 20 nm, 0 nm, -20 nm, -40 nm). Here, contour lines depict the regions of the magnetization that are not completely aligned in the direction of the perpendicular magnetic field (Fig 5.13a). The highest deviations are observed along the top and bottom edges of the slab and appear negligible around the center of the slab. One can further observe the deviations from the top and bottom of the slab along m_z are at opposite sides. We further explore the spin-wave moving through the slab by plotting variations of m_x at the same depth positions as m_z for several time intervals (t_1, t_2, t_3, t_4) detailing the sinusoidal pulse (Fig. 5.13b). This representation allows us to further visualize the spin wave originating from the edge of the slab, which ultimately results in the additional weak mode above magnetic saturation.

5.5 Discussion

We have experimentally measured the resonance properties of dipole skyrmions and bubble domains that form in Fe/Gd films through temperature and thickness dependent studies. Our results suggest there is no contribution in the resonant spectra from skyrmions ordering in a close packing lattice. Furthermore, unlike DMI skyrmions, we do not observe a splitting of the resonant spectra at magnetic fields where a dipole skyrmion phase is present.

Through simulations, we predict that dipole skyrmions showcase localized spin-wave modes that are analogous to those formed by Dzyaloshinskii-Moriya interaction. We show dipole skyrmions possess elaborate dynamics given these textures possess a Bloch-line in the middle of the film and Néel caps that wraps around the cylindrical-like texture. At any resonant frequency, the dynamics of any helicity skyrmion throughout the thickness of the slab is inversed for the skyrmion with the opposite helicity. In future technologies, this difference in dynamics could be exploited as an additional degree of readability to distinguish between both helicity skyrmions, thus enabling each helicity skyrmion a binary bit.

In summary, we show that dipole skyrmions and bubbles are in fact distinct magnetic textures which possess very different dynamics under *r.f.* fields. The resonant properties of skyrmions appear to be different with the physical mechanism that results in their stabilization.

Acknowledgement: Chapter 5 is a reprint of the manuscript being prepared for publication: S. A. Montoya, S. Couture, J. J. Chess, J. C. T. Lee, N. Kent, M.-Y. Im, S. D. Kevan, P. Fischer, B. J. McMorran, S. Roy, V. Lomakin, and E. E. Fullerton. *Resonant properties of dipole stabilized skyrmions in amorphous Fe/Gd multilayers*. The dissertation author was the primary author of this manuscript.

5.6 References

[1] S. P. Parkin, M. Hayashi and L. Thomas, *Magnetic domain-wall racetrack memory*, Science **320**, 190-194 (2008).

[2] N. S. Kiselev, A. N. Bogdanov, R. Schafer and U. K. Robler, *Chiral skyrmions in thin magnetic films: new objects for magnetic storage technologies*. J. Phys. D: Appl. Phys. **44**, 392001 (2011).

[3] A. Fert, V. Cros and J. Sampaio, *Skyrmions on the track*. Nature Nanotech. **8**, 152–156 (2013).

[4] T. Schwarze, J. Waizner, M. Garst, A. Bauer, I. Stasinopoulos, H. Berger, C. Pfleiderer and D. Grundler, "*Universal helimagnon and skyrmion excitation in metallic, semiconducting, and insulating chiral magnets*" Nature Mat. **14**, 478-483 (2015).

[5] Y. Onose, Y. Okamura, S. Seki, S. Ishiwata, and Y. Tokura, "*Observation of magnetic excitations of skyrmion crystal in helimagnetic insulator Cu2OSeO3*" Phys. Rev. Lett. **109**, 037603 (2012).

[6] M. Mochizuki, "*Spin-wave modes and their intense excitation effects in skyrmion crystals*", Phys. Rev. Lett. **108**, 017601 (2012).

[7] C. Moutafis, S. Komineas and J. A. C. Bland. *"Dynamics and switching processes for magnetic bubbles in nanoelements"*, Phys. Rev. B. **79**, 223429 (2009).

[8] F. Büttner, C. Moutafis, M. Schneider, B. Krüger, C. M. Günther, J. Geilhufe, C. v. Korff, Schmising, J. Mohanty, B. Pfau, S. Schaffert, A. Bisig, M. Foerster, T. Schultz, C. A. F. Vaz, J. H. Franken, H. J. M. Swagten, M. Kläui and S. Eisebitt. *"Dynamics and inertia of skyrmionic spin structures"*, Nature Phys. **11**, 225-228 (2015).

[9] J. C. T Lee, J. J. Chess, S. A. Montoya, X. Shi, N. Tamura, S. K. Mishra, P. Fischer, B. J. McMorran, S. K. Sinha, E. E. Fullerton, S. D. Kevan and S. Roy. *Synthesizing skyrmion bound pairs in Fe-Gd films*. Appl. Phys. Lett. **109**, 022402 (2016).

[10] S.A. Montoya, S. Couture, J. C. Chess, J. C. T Lee, N. Kent, M.-Y. Im, S.D. Kevan, P. Fischer, B. J. McMorran, S. Roy, V. Lomakin and E.E. Fullerton, *Dipolar-stabilized skyrmions and skyrmion lattices in Fe/Gd multilayers*, arXiv:1608.01368 (2016).

[11] C. Kittel, "*Theory of the dispersion of magnetic permeability in ferromagnetic materials at microwave frequencies*", Phys. Rev. **71**, 281 (1946).

[12] C. Kittel, "*On the theory of ferromagnetic resonance absorption*", Phys. Rev. **73**, 155 (1947).

[13] G. Xiaobin, L. Xi, Y. Li, X. Han, D. Li, Z. Wang and Y. Zuo. "*Reduction of magnetic damping constant of FeCo films by rare-earth Gd doping*" App. Phys. Lett. **105**, 072411 (2014).

[14] Y. Fu, "*Magnetic properties of* $(Ni_{83}Fe_{17})_{1-x}$ Gd_x *thin films with diluted Gd doping*", IEEE Trans. Mag. **45**, No. 10 (2009).

[15] M.H. Seavey Jr., and P. E. Tannenwald, "*Direct observation of spin-wave resonance*", Phys. Rev. Lett. **1**, 168 (1958).

[16] C. Kittel, "*Excitation of spin waves in a ferromagnet by a uniform rf field*", Phys. Rev. **110**, 1295 (1958).

[17] R. Chang, S. Li, M. V. Lubarda, B. Livshitz and V. Lomakin, *FastMag: Fast micromagnetic simulator for complex magnetic structures.* J. Appl. Phys. **109**, 07D358 (2011).

[18] R. Streubel, F. Kronast, P. Fischer, D. Parkinson, O. G. Schmidt and D. Makarov. *Retrieving spin textures n curved magnetic thin films with full-field X-ray microscopies,* Nature Comm. **6**, 7612 (2015).

Chapter 6

Anisotropic Magnetoresistance Properties of Dipole Skyrmions

6.1 Introduction

Skyrmions exhibit novel transport properties given their topology carry quantized topological charge [1-2]. Numerous studies have shown that when conduction electrons interact with these non-trivial spin textures, the electrons couple to the magnetic texture of the skyrmion accumulating a Berry phase that gives rise to topological hall effect [3-9]. Furthermore, magnetoresistance (MR) measurements reveal that a lattice of skyrmions exhibit a unique signature in the MR-response that is correlated to field-driven magnetic phase transitions that drives the system from a helical to a skyrmion phase [10-11]. However, most of these properties have solely been identified in skyrmions stabilized by Dzyaloshinskii–Moriya interaction (DMI) in helimagnets with non-centrosymmetric structure and there is no evidence that suggests that other class of skyrmions exhibit these kind of phenomena.

Here we present an anisotropic magnetoresistance study in amorphous Fe/Gd multilayers that exhibits magnetic domains ranging from disordered perpendicular stripe domains to ordered dipole skyrmions [12,13]. The chiral textures are stabilized under the application of a perpendicular magnetic field and possess a population of two different helicity skyrmions. Our experimental findings and numerical modeling suggests a dipole skyrmion lattice results in an AMR response that is different DMI skyrmions. In this work, we provide a physical interpretation of the AMR resulting from disordered stripe domains and ordered dipole skyrmions. Using numerical simulations, we validate our experimental observations and show that the reorientation of the Bloch-line results in a distinctive field-dependent AMR response. Our results propose a simple methodology to identify potential ferromagnet and ferrimagnet materials that could host two helicity skyrmions.

6.2 Experimental details

We measure the AMR in three different magnetic field configurations: (i) in-plane and parallel to the length of the wire (longitudinal, $\rho_{||}$), (ii) in-plane and perpendicular to the length of the wire (transverse, $\rho_{\perp}$), and (iii) perpendicular to the film (polar, $\rho_{\odot}$) . In all AMR measurements performed, the magnetic field is swept from H = +10 kOe to H = -10 kOe and conversely. This magnetic field is higher than the field required to saturate the film at any temperature measured based on magnetometry and Hall measurements.

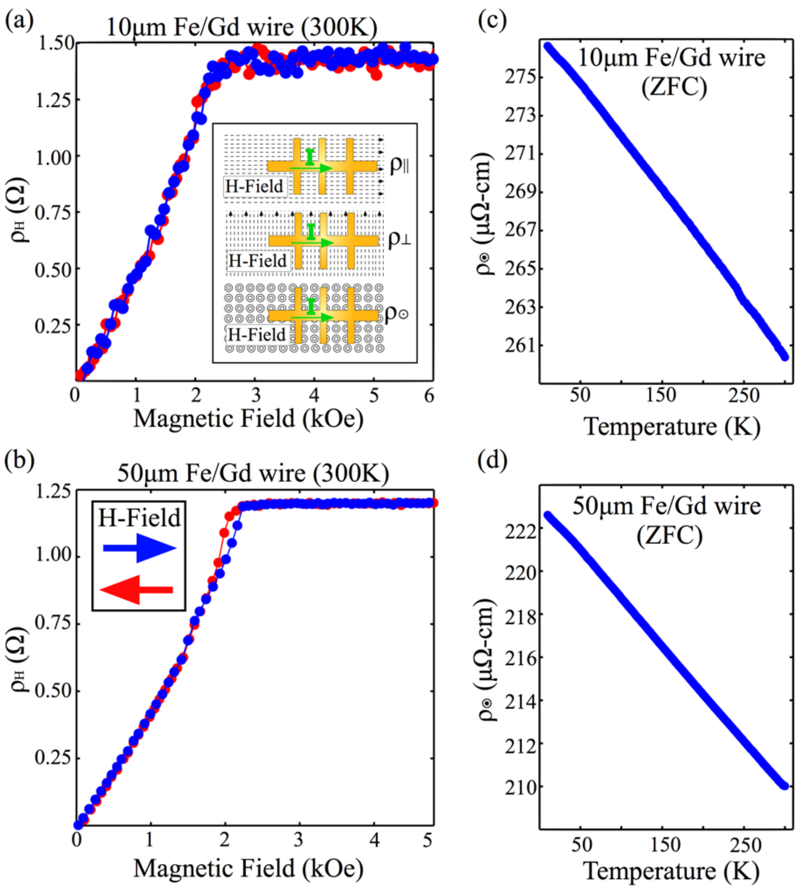

Figure 6.1 –Hall hysteresis and temperature dependence of polar resistivity. (a, b) The field-dependence of the polar Hall resistance obtained at room temperature is shown for two Fe/Gd wires with 10μm and 50μm wide wires. Insert in **(a)** shows the magnetic field and current configurations used to measure the response of the Fe/Gd wires. **(c, d)** The temperature dependence of the polar resistance for both Fe/Gd wires is detailed under a zero-field-cooling (ZFC) protocol.

6.3 Temperature dependence of patterned Fe/Gd wires

Figure 6.1a-b depicts the field-dependent polar Hall resistivity obtained from both Fe/Gd wires at room. Since the Hall response is analogous to the magnetic hysteresis, we are able to conclude that all films possess disordered perpendicular stripe domains at room temperature [13]. The 50μm width Fe/Gd wire exhibits a response closer to the continuous film and the 10μm width Fe/Gd wire exhibits some deviations. Since the wires on deposited onto photo-lithographed devices and the individual layers are ultrathin (<0.4nm), it appears there are some overshadowing effects result in Fe/Gd wires with some minute variations in composition.

Figure 6.1c-d illustrates the temperature dependence of the polar resistivity for both Fe/Gd wires under a zero-field-cooling protocol. At room temperature, the average resistivity is relatively high (> 200μΩ-cm) for either Fe/Gd wire in comparison to other amorphous ferromagnetic alloys [14]. As the temperature is reduced, we observe the resistivity increases in both Fe/Gd wires which suggests the specimens are semi-metallic. The residual resistivity ratio $\rho(80K)/\rho(300K)$ is nearly the same for both wires, i.e. the 10μm wire $\rho(80K)/\rho(300K) \sim 1.049$ and for the 50μm wire is $\rho(80K)/\rho(300K) \sim 1.044$.

Figure 6.2 shows the field dependent longitudinal, transverse and polar AMR at discrete temperatures from 300K to 80K for the 10um Fe/Gd wire. For a magnetic specimen, we know the AMR response depends on the scatter angle between the current and the magnetization. Lower scattering of electrons is expected from magnetic moments aligned perpendicular and orthogonal to the current flow, whereas, moments parallel and anti-parallel to the current flow will result in higher scattering. Because the current is fixed along the length of the wire, we know that different field orientations will allow us to probe the behavior of different textures in the film more favorably. Considering we know the Fe/Gd film possesses disordered perpendicular stripe domains with closure domains, e.g. Néel caps at zero-field [13], we can deduce that: (i) $\rho_{\odot}$ will be most sensitive to scattering from the Bloch wall and Néel caps and (ii) $\rho_{\parallel}$ and $\rho_{\perp}$ will be most susceptible to the scattering from perpendicular stripe domains.

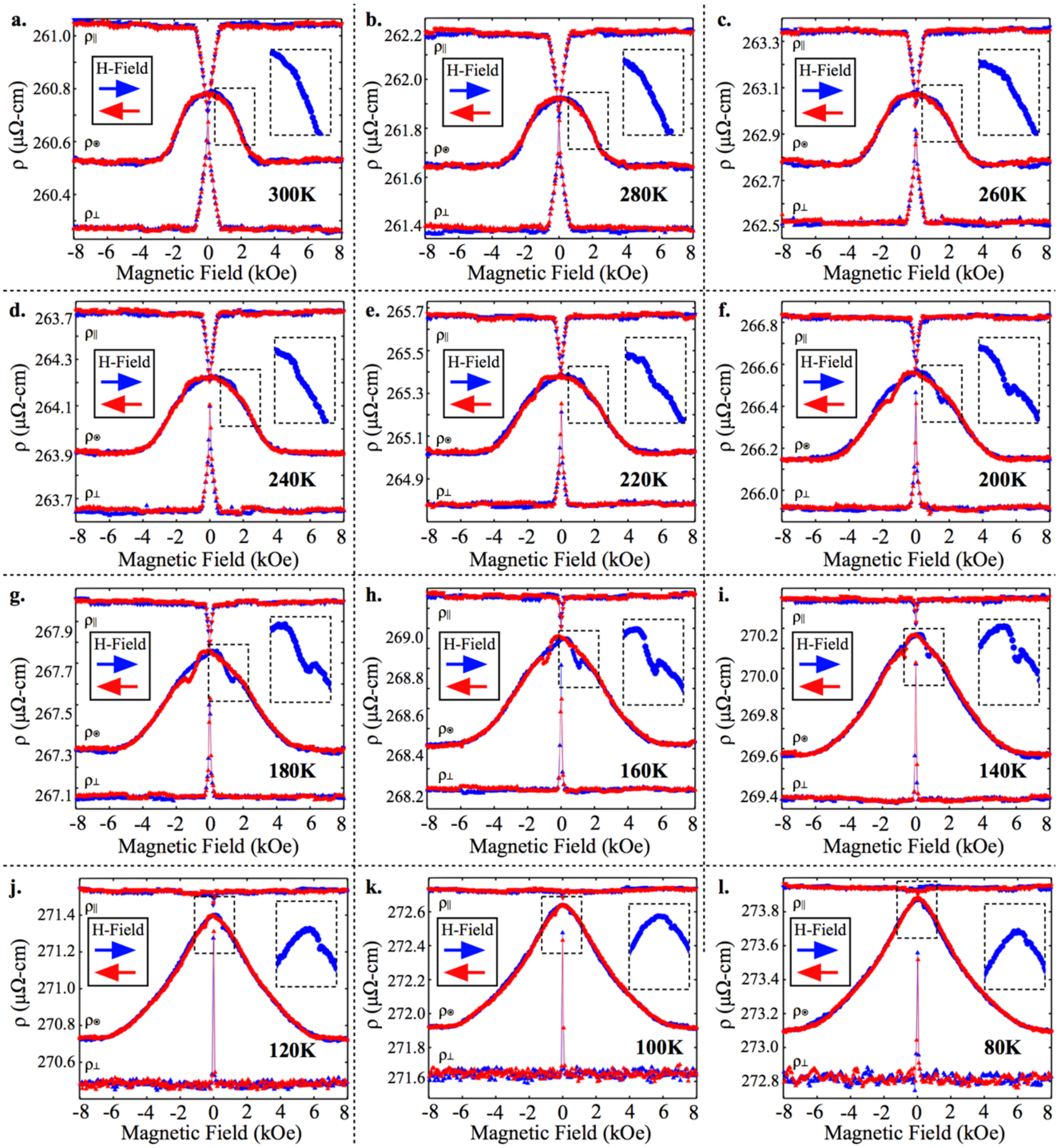

Figure 6.2 – The field-dependent AMR for the 10μm wide Fe/Gd wire. (a-l) Show the field varying longitudinal, polar and transverse resistivity from 300K to 80K in 20K intervals. At each temperature, a region of the field varying polar resistivity is enlarged to show specific features. The field sweeping direction is shown under different color.

It is important to understand that the AMR is a collective scattering response of the magnetic textures being probed.

We first focus on the temperature dependence of the ground state, i.e. domain morphology at zero-field, which provides information about the preferential magnetic order of the system. Under different field history, we find the magnetic domain arrangement is different from in-plane and perpendicular field geometries (Fig. 6.2). This can be deduced from the different values of ρ(H=0) observed along the longitudinal, transverse, and polar AMR response. At room temperature, both longitudinal and transverse AMR exhibit the same ground state, $\rho_{||}(H=0) = \rho_{\perp}(H=0)$, which is lower than the polar response $\rho_{\odot}$(H=0). Since we know the Fe/Gd film exhibits perpendicular stripe domains with Néel caps, we can infer that the stripe domains are disordered because the scattering at zero-field is the same along $\rho_{||}$ and $\rho_{\perp}$. Aligned stripes should result in different scattering along either in-plane field geometries. A higher polar response $\rho_{\odot}(H=0)$, suggests the Néel caps occupy a sizable portion of the volume fraction. We recall these in-plane textures can result in higher scattering [15-17] which contributes to the scattering off perpendicular stripe domains already probed along the longitudinal and transverse directions. As the temperature is reduced, the ground state along the in-plane fields both increase at different rates relative to each other, such that $\rho_{||}(H=0) > \rho_{\perp}(H=0)$ below 300K, which indicates a preferential ordering of the stripes along the length of wire occurs. This rearrangement is achievable when the field completely erases the domain walls in the Fe/Gd wire and the Bloch-line becomes reoriented along the direction of the current when the field is reduced from magnetic saturation.

Increasing the magnetic field, along either of the three orientations, results in a AMR curve that is dependent on the domain structure. Starting from zero-field, the longitudinal and transverse AMR curves linearly change with increasing field. The observation of a symmetric AMR response, around zero-field, indicates the field evolution is very similar in both field directions; in addition, a linear AMR response suggests the domains smoothly tilt in the direction of the applied field. From 300K to 100K, both in-plane field probing schemes exhibit a linear AMR response that narrows around zero-field with decreasing temperature. Above the saturation field H_{sat}, the AMR becomes constant because the magnetization is uniformly aligned in the direction of the applied field; hence, the scattering of conduction electrons should not change above magnetic saturation. The fact that we observe a reduction in the saturation field along $\rho_{||}$ and $\rho_{\perp}$ implies tilting the magnetization of the perpendicular domains in the direction of the applied field becomes easier as the temperature is lowered. This indirectly implies the anisotropy becomes softer with decreasing temperature. Below 100K, the longitudinal AMR becomes almost field independent and the transverse AMR swiftly changes under a weak in-plane field.

Next, we solely focus on the polar AMR evolution as a function of field which shows the Fe/Gd film undergoes a magnetic phase transition at temperatures where a skyrmion phase has been observed (Fig. 6.2). At room temperature, the polar AMR response exhibits a parabolic field dependence where $\rho_{\odot}$ smoothly decays around zero-field toward magnetic saturation. This behavior is consistent from 300K to 260K were only changes in the saturation field are observed (Fig. 6.2a-c). When the temperature is reduced, from 240K to 220K, the polar AMR begins to exhibit a non-uniform field reversal around zero-field (Fig. 6.2d, e). Here, as the field is reduced from positive to negative magnetic saturation, we find

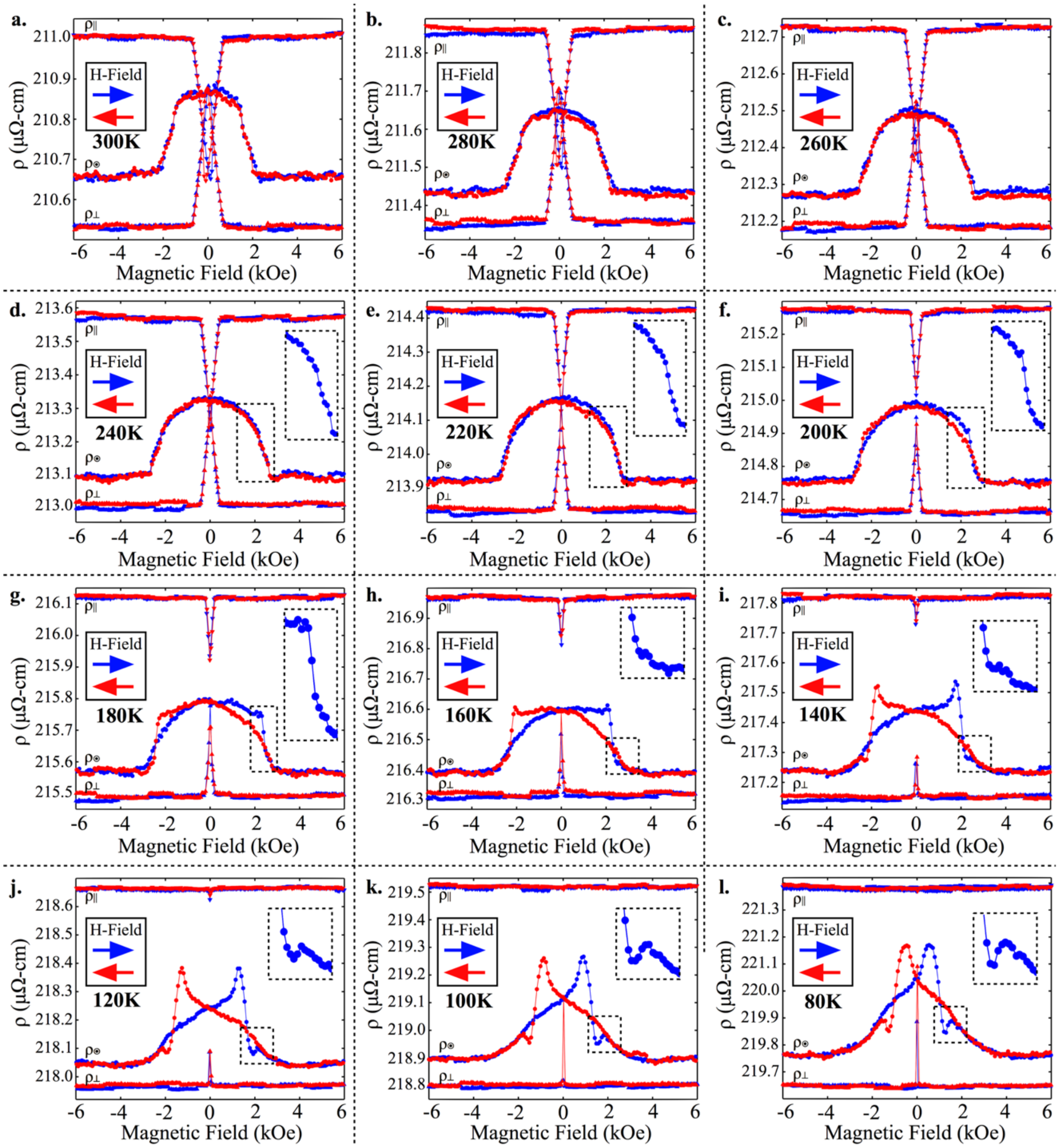

Figure 6.3 – The field-dependent AMR for the 50μm wide Fe/Gd wire. (a-l) Show the field varying longitudinal, polar and transverse resistivity from 300K to 80K in 20K intervals. At each temperature, a region of the field varying polar resistivity is enlarged to show specific features. The field sweeping direction is shown under different color.

the polar AMR sharply changes for a narrow field window, below zero-field, and then continues to decay in a parabolic fashion (Fig. 6.2). Similar AMR response is observed when the field is reversed from negative to positive magnetic saturation. An enlarged view of this AMR variation is detailed in the inserts at each temperature of Figure 6.2. By further reducing the temperature, from 200K to 100K, we find the swift decay in polar AMR becomes a well-defined artifact in the parabolic field dependence (Fig. 6.2f-k). The field window where the artifact appears exhibits an increase in polar resistivity which suggests a magnetic reconfiguration occurs that results in higher scattering. In this same temperature region, we find the polar AMR artifact slowly shifts to lower magnetic field windows as the temperature is reduced. Below 100K, the artifact nearly vanishes which indicates the domain state that gives rise to this AMR signature is no longer favorable at lower temperature (Fig. 6.2l).

Figure 6.3 shows the field dependent AMR response along the three different field configurations for the 50μm width Fe/Gd wire. The ground state obtained along the longitudinal, transverse and polar configurations follows a similar temperature dependence as the 10μm Fe/Gd wire (Fig. 6.2, 6.3). As before, the ground state along the polar AMR response is lower than the longitudinal AMR and higher than the transverse AMR response. Below 200K, the ground state always appears along the transverse AMR response and the highest scattering is observed along the longitudinal AMR response. The field dependence of the longitudinal and transverse response as a function of temperature is almost linear which suggests similar variability of volume fraction of Néel caps and perpendicular stripe domains is expected. Most notable changes are observed along the polar AMR response.

The polar AMR field variation of the 50μm wide Fe/Gd wire shows a more pronounced artifact appear at low temperatures that suggests multiple magnetic transitions exist in this specimen. At room temperature, there is a smooth parabolic decay in polar scattering as we move away from zero-field toward magnetic saturation. This behavior is consistent from 300K to 220K, were only changes in magnetic saturation are observed (Fig. 6.3a-e). At 200K, there begins to appear evidence of an abrupt change in resistivity $\rho_{\odot}$ that is dependent on the field history (Fig. 6.3f-g). Like before, the artifact in the polar AMR response appears below zero-field as the magnetic field is reduced from positive saturation to negative, and vice-versa. As the temperature is decreased, the scattering increases in the field region were the artifact is present such that the highest scattering is no longer observed at zero-field (Fig. 6.3h-l). The peak of the higher scattering does not correspond to a switching field, such as a critical field or nucleation field. Moreover, there is evidence that a second magnetic phase transition appears at higher magnetic fields in the same AMR artifact. The field region where the second phase transition appears is enlarged and detailed in the insert at each temperature (Fig. 6.3h-l). Unlike the 10μm width Fe/Gd wire, the artifact in the polar AMR persists below 80K which suggests the magnetic domain configuration that results in it also continues existing below 80K (Fig. 6.3h-l).

Figure 6.4 details the temperature dependence of the AMR ratio for both Fe/Gd wires previously detailed. The parallel and polar AMR ratio are defined as:

$$AMR_{||}(\%) = \frac{\rho_{||} - \rho_{\perp}}{\rho_{||}} \cdot (100\%) \quad \text{and} \quad AMR_{\odot}(\%) = \frac{\rho_{||} - \rho_{\odot}}{\rho_{||}} \cdot (100\%)$$

where the $\rho_{||}$, $\rho_{\perp}$ and $\rho_{\odot}$ resistivity values obtained above magnetic saturation. For consistency we chose the resistivity values at H_{dc} = 8000 Oe. We find both Fe/Gd wires exhibit an AMR ratio that is relatively low (~0.3%) which is typically expected for amor-

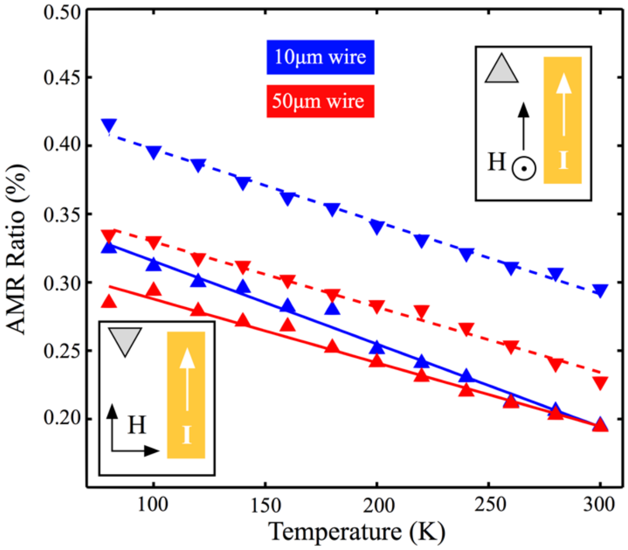

Figure 6.4 –Temperature dependence of AMR ratio for both Fe/Gd wires. The lateral (▽) and perpendicular (△) AMR ratios are calculated from results in Figure 2 and 3. The inserts detail the magnetic field and current geometry for both the lateral (▽) and perpendicular (△) configurations.

phous materials [14]. We find the AMR ratio for the 10μm wire is larger than the 50μm wire. As the temperature is reduced, the AMR ratio for both geometries increases linearly at different rates and there are modest changes as a function of temperature.

6.4 Micromagnetic simulations

To understand the mechanism that results in the artifact in the field dependent polar resistivity (Fig. 6.2f-l, 6.3f-l), we performed numerical simulations of the Landau-Lifshitz-Gilbert (LLG) equation utilizing the FASTMag solver [18]. We utilize material parameters and geometry of the slab as detailed in Chapter 4.10. The magnetic states are obtained as the magnetic field is swept from negative to positive magnetic saturation. The magnetic

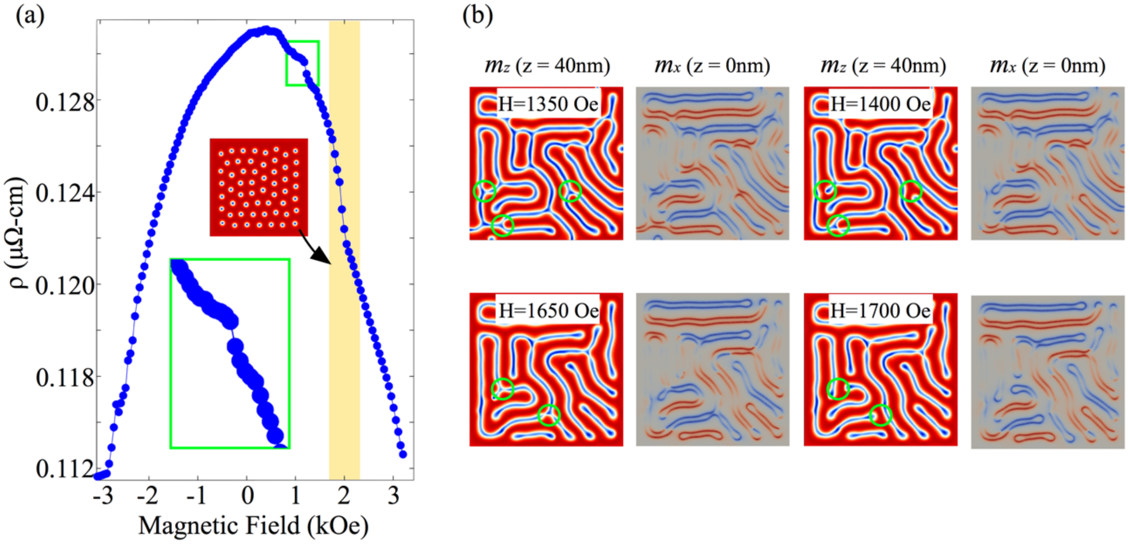

Figure 6.5 – Anisotropic magnetoresistance (AMR) from field dependent domain states. **(a)** Shows the anisotropic magnetoresistance resulting from domain states as the magnetic field is swept from H_z = -3200 Oe to H_z = 3200 Oe. The artifact appearing at positive fields is enlarged in the insert of **(a)**. The region showing a closed packed skyrmion phase is shaded over the AMR loop. **(b)** Shows the topside-view of the domain states at different positions of the slab: the magnetization along the z-axis is shown at z = 40nm and the magnetization along the x-axis is shown at the center of the slab. The field dependent domain states illustrate the collapse of stripe domains.

field is incremented in field steps of H_z = 50 Oe with 10-ns rise and 20-ns relaxation time. Since the AMR ratio is relatively low for these films (Fig. 6.4), we assume the scattering is uniform across the slab when computing the anisotropic magnetoresistance. The AMR is calculated based on $\rho(\phi) = 1 + \Delta\rho \cos^2 \phi$ where $\Delta\rho = \frac{\rho_{||} - \rho_{\perp}}{\rho_{\perp}}$ and ϕ is the angle between the magnetization and the current. For the simulations we set $\Delta\rho = 200\mu\Omega - cm$ based on results in Fig. 6.2 and 6.3, and we assume the current direction runs along the two sides of the slab. The overall resistivity resulting from each domain state is calculated as a network of resistors: elements lying in the direction of the current are added in series and

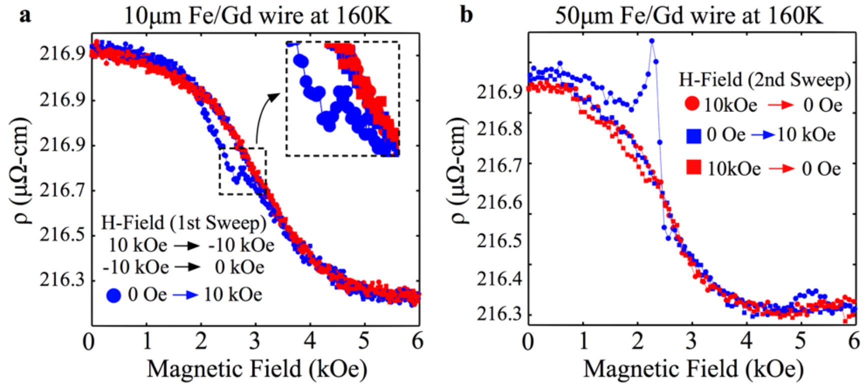

Figure 6.6 – Bloch-line reconfiguration. (a, b) Field-dependent polar AMR response of the 10μm and 50μm Fe/Gd wire at 160K under two different field protocols. The field history is detailed in the inserts of **(a, b)**.

elements transverse to the current direction are added in parallel.

Figure 6.5a shows the calculated anisotropic magnetoresistance that results from magnetic states obtained when sweeping the magnetic field from negative to positive magnetic saturation. For negative magnetic fields, the domain states result in a smooth parabolic resistivity response from negative saturation to zero-field. Then as the magnetic field is increased to positive saturation, a small artifact appears at fields where disordered stripe domains begin to collapse into dumbbell domains that eventually form a dipole skyrmion (Fig. 6.5b). The artifact occurs before the closed packed lattice forms which is color shaded in Fig 6.5b.

6.5 Domain structure rearrangement

To validate the Bloch-line rearrangement leads to the formation of an artifact in the polar anisotropic magnetoresistance response, we measured the AMR under two field histories: (i) First, the magnetic field is set to positive magnetic saturation and it is then reduced to negative magnetic saturation; afterwards, the field is scanned from negative saturation to positive saturation. The latter is the field history which has been detailed for measurements shown in Figure 2 and 3. (ii) The second field history consists of reducing the magnetic field from positive saturation to zero-field and then increasing the field once again to positive saturation and finally reducing it to zero-field.

Figure 6a, b shows the polar AMR response of both Fe/Gd wires at 160K under the latter magnetic field protocols. As the magnetic field is increased from zero-field to magnetic saturation, the AMR response exhibits an artifact as previously detailed (Fig. 6.2h, 6.3h). Then when the magnetic field is reduced from saturation to zero-field, the resistivity exhibits a parabolic field dependence with an AMR response that is lower than the latter, as observed in Fig 6.2h and 6.3h. Subsequently, when then magnetic field is increased again from zero-field to positive saturation, the AMR smoothly decays in a parabolic fashion and there is no presence of an artifact in the polar resistivity. Reducing the field from positive saturation to zero field, yields a higher resistivity than under the first field protocol.

6.6 Discussion

We have experimentally measured the field varying anisotropic magnetoresistance resulting from disordered stripe domains that arrange into isolated dipole skyrmions and a closed packed lattice of dipole skyrmions in amorphous Fe/Gd multilayers. The AMR was collected along three field-current probing schemes that allowed us to characterize the domain states encountered in the film from perpendicular domains, Bloch-line and Néel caps. Along the polar AMR response, it was found that an asymmetric artifact formed as the magnetic field is swept from positive to negative saturation and vice-versa. This artifact only appeared at temperatures where a closed packed skyrmion phase was previously image using resonant soft x-ray scattering and Lorentz transmission electron microscopy in continuous films as reported in Ref. 13. Furthermore, the AMR artifact appears to exhibit a geometrical size dependence given the 10µm wide Fe/Gd wire shows a smaller artifact compared to a 50µm wide Fe/Gd wire.

Utilizing numerical simulations, we reproduced our experimental observation of an artifact in the polar AMR loop from domain states exhibiting similar domain morphology. From inspecting the domain states, it was found that the artifact results primarily from disordered stripe domains that being to collapse into chiral domains that will form dipole skyrmions. The artifact occurred at magnetic fields prior to the formation of a closed packed lattice of dipole skyrmions. Given the slab lateral dimensions, we expected the artifact in the polar AMR to be small given experimental observations in larger geometries.

Our observations in the field varying AMR response could be utilized as a simple mechanism to probe ferromagnets and ferrimagnets for the existence of closed packed lattice of cylindrical features which is simpler than performing any imaging measurements.

Acknowledgement: Chapter 6 is a reprint of the manuscript being prepared for publication: S. A. Montoya, M. V. Lubarda, S. Couture, V. Lomakin and E. E. Fullerton. *Anisotropic magnetoresistance properties of dipole skyrmions in amorphous Fe\Gd multilayers*. Preprint (2016). The dissertation author was the primary author of this manuscript.

6.7 References

[1] T. H. R. Skyrme, *A unified field theory of mesons and baryons*. Nuclear Phys. 31, 556-569 (1962).

[2] N. Nagaosa and Y. Tokura, *Topological properties and dynamics of magnetic skyrmions*. Nat. Nanotechnol. **8**, 899-911 (2013).

[3] N. Kanazawa, et al. Large topological hall effect in a short-period helimagnet MnGe. Phys. Rev. Lett. 106, 156603 (2011).

[4] T. Schulz, R. Ritz, A. Bauer, M. Halder, M. Wagner, C. Franz, C. Pfleiderer, K. Everschor, M. Gasrt and A. Rosch. *Emergent electrodynamics of skyrmions in a chiral magnet.* Nat. Phys. **8**, 301-304 (2012).

[5] S. X. Huang and C. L. Chien, *Extended skyrmion phase in epitaxial FeGe(111) thin films*. Phys. Rev. Lett. 108, 267201 (2012).

[6] Y. Li, N. Kanazawa, X. Z. Yu, A. Tsukazaki, M. Kawasaki, M. Ichikawa, X. F. Jin, F. Kagawa and Y. Tokura. *Robust formation of skyrmions and topological hall effect anomaly in epitaxial MnSi*. Phys. Rev. Lett. **110**, 117202 (2013).

[7] D. Liang, J. P. DeGrave, M. J. Stolt, Y. Tokura and S. Jin. *Current-driven dynamics of skyrmions stabilized in MnSi nanowires revealed by topological Hall effect*. Nat. Comm. 6, 8217 (2015).

[8] A. Neubauer, C. Pfleiderer, B. Binz, A. Rosch, R. Ritz, P.G. Niklowitz and P. Böni. *Topological hall effect in the A Phase of MnSi.* Phys. Rev. Lett. **102**, 186602 (2009).

[9] J. Matsuno, N. Ogawa, K. Yasuda, F. Kagawa, W. Koshibae, N. Nagaosa, Y. Tokura and M. Kawasaki. *Interface-driven topological hall effect in* $SrRuO_3$-$SrIrO_3$ *bilayer*. Sci. Adv. **2**, E1600304 (2016).

[10] H. Du, J. P. DeGrave, F. Xue, D. Liang, W. Ning, J. Yang, M. Tian, Y. Zhang and S. Jin. *Highly stable skyrmion state in helimagnet MnSi nanowires*. Nano Lett. 14, 2026-2032 (2014).

[11] H. Du, D. Liang, C. Jin, L. Kong, M. J. Stolt, W. Ning, J. Yang, Y. Xing, J. Wang, R. Che, J. Zang, S. Jin, Y. Zhang and M. Tian. *Electric field probing of field-driven cascading quantized transitions of skyrmion cluster states in MnSi nanowires*. Nat. Comm. 6, 7637 (2015).

[12] J. C. T Lee, J. J. Chess, S. A. Montoya, X. Shi, N. Tamura, S. K. Mishra, P. Fischer, B. J. McMorran, S. K. Sinha, E. E. Fullerton, S. D. Kevan and S. Roy. *Synthesizing skyrmion bound pairs in Fe-Gd films*. Appl. Phys. Lett. **109**, 022402 (2016).

[13] S.A. Montoya, S. Couture, J. C. Chess, J. C. T Lee, N. Kent, M.-Y. Im, S.D. Kevan, P. Fischer, B. J. McMorran, S. Roy, V. Lomakin and E.E. Fullerton, *Dipolar-stabilized skyrmions and skyrmion lattices in Fe/Gd multilayers*, arXiv:1608.01368 (2016).

[14] T. R. Mcguire and R. I. Potter. *Anisotropic magnetoresistance in ferromagnetic 3d alloys.* IEEE Trans. Magn. 11, 1018-1038 (1975).

[15] U. Rudiger, J. Yu, L. Thomas, S. S. P. Parkin and A. D. Kent. *Magnetoresistance, micromagnetism, and domain-wall scattering in epitaxial hcp Co films.* Phys. Rev. B. 59, 11914 (1999).

[16] A. D. Kent, J. Yu, U. Rudiger and S. S. P. Parkin. *Domain wall resistivity in epitaxial thin film microstructures*. J. Phys. Condens. Matter. 13, R461 (2001).

[17] D. Ravelosona, A. Cebollada, F. Briones, C. Diaz-Paniagua, M. A. Hidalgo and F. Batallan. *Domain-wall scattering in epitaxial FePd ordered alloy films with perpendicular magnetic anisotropy*. Phys. Rev. B 59, 4322 (1999).

[18] R. Chang, S. Li, M. V. Lubarda, B. Livshitz and V. Lomakin, *FastMag: Fast micromagnetic simulator for complex magnetic structures.* J. Appl. Phys. **109**, 07D358 (2011).

Chapter 7

Conclusions

7.1 Thesis results

In this thesis, we have detailed the observation and study of nanomagnetic cylindrical-like features with chiral topology termed dipole skyrmions in amorphous Fe/Gd multilayers. In Chapter 4, we have shown through the study of numerous Fe/Gd films of varied alloy composition and overall film thickness that these class domains are achievable in a material parameter space with $Q < 1$. The overall required properties that favor the formation of these domain consists of thick films with low uniaxial anisotropy K_U, low magnetization M_S and low exchange A_{ex}. We have demonstrated tunability of the broad dipole skyrmion phase in temperatures and applied magnetic fields is achievable by modifying the layer structure and film thickness. Unlike DM skyrmions, the dipole skyrmions investigated possess a chiral Bloch-line at the center of the film and Néel caps that extend from the center to the surface of the film. Furthermore, we have experimentally demonstrated that dipole skyrmions with sub-100nm features are achievable by means of competing dipole and domain wall energy, which contradicts a common conception of dipole skyrmions.

These rich textures result in novel electromagnetic properties, as we have detailed in Chapter 5 and 6, which suggests many of the interesting properties observed in skyrmions result from topology of the magnetic domain and not the physical mechanism that stabilizes these chiral textures. Under the microwave field perturbations, we have verified that dipole skyrmions exhibit localized spin wave modes that are independent on whether these arrange in closed packed lattice or they are uncorrelated. We observe no splitting of the resonant mode branches where the dipole skyrmion phase forms, which suggests this splitting in the resonant mode branches in DMI skyrmions could potentially be related to a magnetic phase change from a helical to a skyrmion phase in non-centrosymmetric magnets. We also observe a clear distinction in the resonant modes resulting at temperatures where either disordered stripe domain phase or a skyrmion phase is preferable. The localized spin wave modes numerically predicted for the dipole skyrmions are far more complex than those expected in DMI skyrmions, given the domain structure of the dipole skyrmion. We predict the existence of four localized spin wave modes in dipole skyrmions. Also opposite helicity dipole skyrmions show the inverse spin wave dynamics as a function of thickness. We also show the excitation of magnetic bubbles and dipole skyrmions are distinct. This further shows that although bubbles and dipole skyrmions form due to the same physical mechanism, the topology of the magnetic features results in very different properties.

Transport studies on patterned Fe/Gd wires show that a closed packed lattice of dipole skyrmions exhibits an artifact in the anisotropic magnetoresistance response at comparable magnetic fields where the skyrmion phase forms. Using numerical simulations, we showed that the artifact in the polar resistivity results from a domain reconfiguration that occurs as the domain morphology transitions from disordered stripes to an ordered skyrmion phase under a magnetic field. We also demonstrated that the artifact in the AMR response exhibits a geometrical size dependence: wide wires show a more pronounced artifact compared to narrow wires. The artifact in the polar resistivity is sensitive to field history and does not arise if the magnetic domain states transition from stripes to isolated dipole skyrmions under a magnetic field.

In overall, many of the conclusion reached in our studies can be extended to other ferromagnets and ferrimagnets exhibiting dipole skyrmions that form in films with $Q < 1$ where the moment and exchange can be tuned. Our results are indicative that dipole skyrmions are very interesting magnetic textures and possess rich physics.

7.2 Future outlook

There are still many interesting open questions that need to be explored on the subject of dipole skyrmions. Here, we specifically studied the formation of topologically chiral magnetic features in amorphous Fe/Gd multilayers that form in relatively thick films (~50 to 80-nm). The next venue would be to stabilize comparable dipole skyrmions in different magnetic systems as well as determine the feasibility of reducing the size of the magnetic features even further.

Since most studies have solely focused on investigating properties and dynamics in DMI skyrmions, it is of interest to investigate whether how dipole skyrmions behave when perturbed with d.c. current and a.c current pulses, and similarly how these textures behave under thermal gradients. The observation and quantification of current induced displacement of dipole skyrmions has fundamental and technological implications. Future studies should address whether these texture can be moved with comparable current densities as DMI skyrmions as well as determining the mechanism by which these textures move. Experimental evidence of current displacement should further promote these class of skyrmions as memory bits for potential memory technologies.